Regulation of Star Formation Rates in Multiphase Galactic Disks: Numerical Tests of the Thermal/Dynamical Equilibrium Model

Chang-Goo Kim[1,2], Woong-Tae Kim[1,2,3], and Eve C. Ostriker[4]

[1]*Center for the Exploration of the Origin of the Universe (CEOU), Astronomy Program, Department of Physics & Astronomy, Seoul National University, Seoul 151-742, Republic of Korea*

[2]*Department of Physics & Astronomy, FPRD, Seoul National University, Seoul 151-742, Republic of Korea*

[3]*Institute for Advanced Study, Einstein Drive, Princeton, NJ 08540, USA*

[4]*Department of Astronomy, University of Maryland, College Park, MD 20742, USA*

kimcg@astro.snu.ac.kr, wkim@astro.snu.ac.kr, ostriker@astro.umd.edu

ABSTRACT

We use vertically-resolved numerical hydrodynamic simulations to study star formation and the interstellar medium (ISM) in galactic disks. We focus on outer disk regions where diffuse H I dominates, with gas surface densities $\Sigma = 3 - 20 \, \mathrm{M}_\odot \, \mathrm{pc}^{-2}$ and star-plus-dark matter volume densities $\rho_{\mathrm{sd}} = 0.003 - 0.5 \, \mathrm{M}_\odot \, \mathrm{pc}^{-3}$. Star formation occurs in very dense, self-gravitating clouds that form by mergers of smaller cold cloudlets. Turbulence, driven by momentum feedback from supernova events, destroys bound clouds and puffs up the disk vertically. Time-dependent radiative heating (FUV from recent star formation) offsets gas cooling. We use our simulations to test a new theory for self-regulated star formation. Consistent with this theory, the disks evolve to a state of vertical dynamical equilibrium and thermal equilibrium with both warm and cold phases. The range of star formation surface densities and midplane thermal pressures is $\Sigma_{\mathrm{SFR}} \sim 10^{-4} - 10^{-2} \, \mathrm{M}_\odot \, \mathrm{kpc}^{-2} \, \mathrm{yr}^{-1}$ and $P_{\mathrm{th}}/k_{\mathrm{B}} \sim 10^2 - 10^4 \, \mathrm{cm}^{-3} \, \mathrm{K}$. In agreement with observations, turbulent velocity dispersions are $\sim 7 \, \mathrm{km \, s}^{-1}$ and the ratio of the total (effective) to thermal pressure is $P_{\mathrm{tot}}/P_{\mathrm{th}} \sim 4-5$, across this whole range (provided shielding is similar to the Solar neighborhood). We show that Σ_{SFR} is not well correlated with Σ alone, but rather with $\Sigma \sqrt{\rho_{\mathrm{sd}}}$, because the vertical gravity from stars and dark matter dominates in outer disks. We also find that Σ_{SFR} has a strong, nearly linear correlation with P_{tot}, which itself is within $\sim 13\%$ of the dynamical-equilibrium estimate $P_{\mathrm{tot,DE}}$. The quantitative relationships we find between Σ_{SFR} and the turbulent and thermal pressures show that star formation is highly efficient for energy and momentum production, in contrast to the low efficiency of mass consumption. Star formation rates adjust until the ISM's energy and momentum losses are replenished by feedback within a dynamical time.

Subject headings: galaxies: ISM — galaxies: kinematics and dynamics — galaxies: star formation — method: numerical — turbulence

1. Introduction

Large-scale star formation rates in galaxies are observed to correlate with both the gaseous and stellar content, and with the galaxy's gravitational potential well (e.g. Ryder & Dopita 1994; Kennicutt 1998; Wong & Blitz 2002; Boissier et al. 2003; Salim et al. 2007; Leroy et al. 2008; Bigiel et al. 2008, 2010, 2011; Genzel et al. 2010; Daddi et al. 2010; Shi et al. 2011). Empirical fits in disks often adopt power-law ("Kennicutt-Schmidt") forms for the relationship among the surface density of star formation Σ_{SFR}, the surface density of gas Σ, the surface density of the old stellar disk Σ_s, and the orbital angular velocity Ω.

From the "supply side" point of view, gas represents the fuel for star formation, and the stellar disk and dark matter halo help to define dynamical timescales within the interstellar medium (ISM) that could affect how rapidly gas collects and collapses: the galactic orbital time, the vertical oscillation period and flow crossing time, and the gravitational free-fall time. Power laws naturally arise if the star formation rate is proportional to the ratio of the gas content and one of these dynamical times. The observed timescale for gas to be converted to stars, $t_{SF,gas} \equiv \Sigma/\Sigma_{SFR}$ is, however, generally quite long compared to these dynamical times. Together, the empirical results present a picture of star formation that is sensitive to both fuel supply and ambient environmental conditions, and that has low apparent efficiency.

In recent work, Ostriker et al. (2010) (hereafter OML10) and Ostriker & Shetty (2011) (hereafter OS11) have argued that star formation rates respond to demand, as well as supply. Maintaining an equilibrium state in the ISM requires constant inputs of energy and momentum, and contributions from star formation are critical. Star formation can be self-regulated via feedback, in such a way that supply and demand match within the ISM: heating balances cooling, pressure balances gravity, and turbulent driving balances dissipation. The theory of OML10 and OS11 proposes that observed star formation rates can be understood as a response to the needs of the ISM. Because each massive star injects so much energy, only a relatively modest star formation rate (implying a long $t_{SF,gas}$) is necessary. From the point of view of energy and momentum sources and sinks, star formation is in fact quite efficient.

To see why feedback is vital, it is key to consider the internal thermal and dynamical state of the ISM, rather than just integrated properties. The internal vertical dynamical time $t_{dyn} \propto (G\rho_{tot})^{-1/2}$, for ρ_{tot} the total (gas + stellar) density, depends on the thicknesses of the gaseous and stellar disks. In particular, the contribution from gas gravity alone gives $\Sigma/t_{dyn} \propto \Sigma^{3/2}/H^{1/2}$. The gas disk thickness H depends (linearly or quadratically) on the vertical velocity dispersion of the gas, which includes both thermal and turbulent terms.[1] Because thermal energy is radiated away, and turbulent energy is dissipated (in shocks and shear layers) on timescales $\lesssim t_{dyn} \ll t_{SF,gas}$, the internal energy must be continuously replenished. Young, high-mass stars restore this energy and preserve the life of the ISM. If star formation feedback were entirely absent and the only heating source were the cosmic background radiation, t_{dyn} would drop by nearly two orders of magnitude, with a corresponding (or greater) increase in Σ_{SFR}.

OML10 and OS11, considering respectively mid-to-outer disks and central starburst regions, showed

---

[1]In this work we neglect the magnetic term, which is likely to be small (see below) but would provide a minimum vertical support in the limit of vanishing turbulent terms.

that observed star formation rates are quantitatively consistent with analytic predictions that follow from imposing thermal and dynamical equilibrium in the diffuse ISM. OS11 also presented initial results of numerical simulations that include turbulent driving associated with star formation, confirming the analytic theory for molecule-dominated regions. Additional results from simulations in the starburst regime will be presented in Shetty & Ostriker (2011, in preparation).

In this paper, we use time-dependent numerical simulations to test the OML10 theory (and extensions based on OS11), for the outer-disk regime where the ISM is dominated by diffuse atomic gas. A crucial aspect of our simulations is that we vertically resolve the disk (our grid scale is 1 pc). We shall show that, as assumed by OML10, thermal and vertical dynamical equilibrium are both satisfied in our numerical models. We shall also show that feedback from star formation is largely responsible for sustaining both the thermal and turbulent pressure (and energy) in the atomic ISM. We numerically calibrate the yield relation between Σ_{SFR} and the thermal and turbulent pressures in the diffuse ISM, demonstrating that near-linear relations hold for both P_{th} and P_{turb}. By combining these feedback relations with dynamical equilibrium, we show that Σ_{SFR} depends nearly linearly on the weight of the diffuse ISM (i.e. the dynamical-equilibrium pressure $P_{tot,DE} \approx P_{th} + P_{turb}$). The correlation between Σ_{SFR} and P_{tot} (or $P_{tot,DE}$) is stronger and more general than other star formation relations that are commonly cited.

In addition to testing the thermal/dynamical equilibrium theory of star formation, our numerical models allow us to address a number of interesting issues related to observations of diffuse atomic gas in the Milky Way and external galaxies (Dickey et al. 1990; Braun 1997; van Zee & Bryant 1999; Heiles & Troland 2003; Young et al. 2003; Petric & Rupen 2007; Dickey et al. 2009; Kalberla & Kerp 2009). These observations show that (1) turbulent velocity dispersions are typically ~ 10 km s^{-1}, relatively independent of location or star formation rate; (2) both cold and warm atomic gas are pervasive, in proportions that appear relatively independent of location; (3) the thermal pressure is a small fraction of the total pressure. Our numerical results are consistent with these observations, and can be understood based on the thermal/dynamical equilibrium model with energy and momentum feedback from star formation.

Our numerical models are idealized in that they represent a local patch of unmagnetized gas in a featureless disk where star formation is primarily responsible for the injection of thermal and kinetic energies. Thus, in this paper we do not capture the potential consequences of galactic structural features and certain instabilities that may affect ISM dynamics and star formation. The ISM surface density averaged over $\sim$ kpc scales can be significantly affected by large-scale gravitational instability (e.g., Wada & Norman 1999, 2007; Kim & Ostriker 2001, 2002, 2007; Li et al. 2005; Tasker & Bryan 2006; Tasker & Tan 2009; Tasker 2011; Bournaud et al. 2007; Bournaud & Elmegreen 2009; Hopkins et al. 2011), spiral arm compression (e.g. Kim & Ostriker 2002, 2006; Shetty & Ostriker 2006; Kim et al. 2008, 2010; Dobbs & Bonnell 2006, 2008; Dobbs et al. 2008, 2011; Wada & Koda 2004; Wada 2008; Wada et al. 2011), and Parker instability (e.g. Basu et al. 1997; Kim et al. 1998, 2001, 2002; Mouschovias et al. 2009). Since the timescales to collect gas over $\gtrsim$ kpc scales from gravitational instabilities and spiral arms are longer than local dynamical times, our models may nevertheless provide a good first approximation to the effects of star formation feedback on local regions within larger gas accumulations. In addition, initial tests we have conducted which include magnetic fields (permitting Parker instability) show similar behavior to our unmagnetized models.

As well as producing $\sim$ kpc-scale overdensities, both gravitational instabilities (e.g. Wada et al. 2002; Kim et al. 2003; Kim & Ostriker 2007; Agertz et al. 2009; Aumer et al. 2010; Bournaud et al. 2010) and spiral shocks (e.g. Kim & Ostriker 2006; Kim et al. 2006, 2010; Dobbs et al. 2006), together with magnetorotational instabilities (e.g., Kim et al. 2003; Piontek & Ostriker 2004, 2005, 2007), drive turbulence in the ISM. In particular, turbulence levels $\gtrsim 10$ km s^{-1} can be produced by large-scale gravitational instability, and may be important during the highly-transient early evolution of disk galaxies. Several of the above numerical models have shown, however, that unless energy (representing feedback) is locally injected into massive, high-density clumps that form, the result is irreversible gravitational collapse and star formation far exceeding observed rates. Stellar feedback therefore appears to be crucial for disrupting bound clouds (thus limiting star formation) and maintaining – over many galactic orbits – turbulent ISM levels similar to those observed in nearby galaxies.

The plan of this paper is as follows. In Section 2, we begin by summarizing the theory developed in OML10 and OS11. Section 3 describes the numerical methods and parameters used for our time-dependent simulations, and Section 4 presents our model results. These include time averages of star formation rates, thermal and turbulent pressures, gas layer scale-heights, thermal and turbulent velocity dispersions, and mass fractions of gas components. In Section 5, we use our numerical results to test the validity of the physical assumptions and adopted parameters in the OML10 theory. Here, we also demonstrate the balance between turbulent driving and dissipation (as in OS11), and quantify the feedback yield relations between $P_{\rm th}$ and $P_{\rm turb}$, and $\Sigma_{\rm SFR}$. We compare our numerical results to several simple prescriptions for star formation in Section 6. Section 7 summarizes and discusses our main results.

2.   Summary of Thermal/Dynamical Equilibrium Model

In this section, we briefly summarize the OML10 thermal/dynamical equilibrium model, highlighting the fundamental assumptions and predictions that we shall test in this work. We then draw on OS11 to outline additional predictions related to the dynamical state and star formation rate in disks dominated by turbulent, diffuse gas, and describe how these hypotheses will be tested.

OML10 considered a multiphase, turbulent galactic ISM disk with thermal properties mediated by stellar heating. The gaseous disk, with total surface density of neutral gas Σ, is immersed within the stellar disk and dark matter halo, whose combined midplane density is given by $\rho_s + \rho_{\rm dm} \equiv \rho_{\rm sd}$. The neutral gas disk is composed of two components: diffuse gas, with surface density averaged over large scales $\Sigma_{\rm diff}$; and gravitationally bound clouds (GBCs) with surface density averaged over large scales (i.e. many individual bound clouds) $\Sigma_{\rm GBC} = \Sigma - \Sigma_{\rm diff}$. The diffuse component includes both warm, rarefied gas and cold, dense gas in cloudlets that are not massive enough to be gravitationally bound. Star formation takes place within the gravitationally-bound component.

The first key assumption of OML10 is that the volume-filling diffuse ISM disk is in force balance in the vertical direction. The combined inward gravitational force of the stars, dark matter, and gas (both diffuse and GBC components) must be matched by the outward pressure forces within the diffuse gas. Averaging

the vertical component of the momentum equation over time and in the horizontal direction, OML10 showed that in a state of dynamical equilibrium, $P_{\text{tot}} = P_{\text{tot,DE}}$ for

$$P_{\text{tot,DE}} \equiv \frac{\pi G \Sigma_{\text{diff}}^2}{4} \left\{ 1 + 2\frac{\Sigma_{\text{GBC}}}{\Sigma_{\text{diff}}} + \left[\left(1 + 2\frac{\Sigma_{\text{GBC}}}{\Sigma_{\text{diff}}} \right)^2 + \frac{32\zeta_d c_w^2 \tilde{f}_w \alpha}{\pi G} \frac{\rho_{\text{sd}}}{\Sigma_{\text{diff}}^2} \right]^{1/2} \right\}; \tag{1}$$

that is, the total effective midplane pressure[2] P_{tot} must support the weight of the overlying diffuse gas in the total gravitational field. Although we use the symbol $P_{\text{tot,DE}}$ to denote the vertical weight, it is important to note that the weight and effective pressure balance only if equilibrium holds, and only in an averaged sense.

In equation (1), α is the ratio of total (effective) pressure to thermal pressure in the diffuse medium, ζ_d is a dimensionless parameter characterizing the gas density profile ($\zeta_d = 1/\pi$ for a Gaussian profile), $c_w = (kT_w/\mu)^{1/2}$ is the thermal speed of the warm gas, and $\tilde{f}_w = v_{\text{th,diff}}^2/c_w^2$ for $v_{\text{th,diff}}$ the mass-weighted thermal velocity dispersion in the diffuse gas. The quantity $\tilde{f}_w$ is also equal to ρ_w/ρ_0 for ρ_w the warm medium density and ρ_0 the volume-averaged density of the diffuse medium (including cold cloudlets, assumed to be in pressure equilibrium with the warm medium) at the disk midplane. The mass fraction of the warm medium in the diffuse gas is comparable to $\tilde{f}_w$ (see OML10). In a state of dynamical equilibrium, the midplane diffuse-gas thermal pressure $P_{\text{th}} = \rho_0 v_{\text{th,diff}}^2$ is equal to

$$P_{\text{th,DE}} = \frac{P_{\text{tot,DE}}}{\alpha} \tag{2}$$

(see equation 11 of OML10). If the dominant contributions to the total effective pressure are thermal and turbulent terms with $P_{\text{turb}} = \rho_0 v_{\text{z,diff}}^2$, then $\alpha = (v_{\text{th,diff}}^2 + v_{\text{z,diff}}^2)/v_{\text{th,diff}}^2 = \sigma_{\text{z,diff}}^2/v_{\text{th,diff}}^2$ for $v_{\text{z,diff}}$ the turbulent vertical velocity dispersion and $\sigma_{\text{z,diff}}$ the total vertical velocity dispersion in the diffuse gas ($\sigma_{\text{z,diff}}$ is a direct observable for a face-on disk). Note that in equation (1), the product $c_w^2 \tilde{f}_w \alpha = P_{\text{tot}}/\rho_0$, which is equal to $\sigma_{\text{z,diff}}^2$ if turbulent and thermal terms dominate the effective pressure, i.e. $P_{\text{tot}} \approx P_{\text{th}} + P_{\text{turb}}$.

Next, OML10 assumed that the diffuse ISM is in a state of thermal equilibrium, in which cold and warm atomic phases coexist at a midplane thermal pressure $P_{\text{th,TE}}$. In order for the diffuse gas to be in the two-phase regime, $P_{\text{th,TE}}$ must fall between the minimum pressure P_{min} for the cold phase and the maximum pressure P_{max} for the warm phase (cf. Field et al. 1969). Both P_{max} and P_{min} depend linearly on the local radiative heating rate per particle, Γ, which itself depends approximately linearly on the locally-averaged star formation rate surface density, Σ_{SFR}, if young massive stars are responsible for most of the heating. Motivated by detailed modeling of heating and cooling in the Solar neighborhood (Wolfire et al. 2003) and numerical simulations of turbulent multiphase gas (Piontek & Ostriker 2005, 2007), OML10 assumed that $P_{\text{th,TE}}$ is comparable to the geometric-mean pressure $P_{\text{two}} \equiv (P_{\text{min}} P_{\text{max}})^{1/2}$. Based on the results of Wolfire

---

[2] As discussed in OML10, P_{tot} is actually a pressure *difference* between the midplane and the top of the neutral layer. Thus, if the cosmic-ray and magnetic scale heights far exceed that of the neutral gas, there is not a significant contribution to P_{tot} from magnetic or cosmic-ray terms (even if their midplane pressures are large), and the weight of the diffuse neutral layer must be supported primarily by turbulent and thermal pressure.

et al. (2003), OML10 adopted a geometric mean "two-phase" pressure given by

$$P_{\text{two}}/k_{\text{B}} = 3 \times 10^3 \text{ cm}^{-3}\text{K}\frac{4G'_0}{1+3Z'_d(\Sigma/\Sigma_0)^{0.4}}, \tag{3}$$

where k_{B} is the Boltzmann constant, $G'_0 = J_{\text{FUV}}/J_{\text{FUV},0}$ is the mean FUV intensity relative to the Solar neighborhood value $J_{\text{FUV},0} = 2.2 \times 10^{-4} \text{ erg s}^{-1} \text{ cm}^{-2}\text{sr}^{-1}$, $\Sigma_0 = 10 \text{ M}_\odot \text{ pc}^{-2}$ is the surface density of neutral gas at the Solar circle (Dickey & Lockman 1990; Kalberla & Kerp 2009), and Z'_d is the dust abundance relative to Solar neighborhood value. In the Solar neighborhood, $P_{\text{two}}/k_{\text{B}} = 3000 \text{ cm}^{-3}\text{K}$ for the OML10 prescription.

In a state of simultaneous thermal and dynamical equilibrium, heating and cooling are in balance so that $P_{\text{th}} = P_{\text{th,TE}} \sim P_{\text{two}}$, and vertical forces are in balance so that $P_{\text{th}} = P_{\text{th,DE}}$. With $P_{\text{two}} \propto G'_0 \propto J_{\text{FUV}} \propto \Sigma_{\text{SFR}}$, the surface density of star formation should be proportional to P_{th}. Thus, equating (2) and (3) yields an expression for the star formation rate, with Σ_{SFR} proportional to the right-hand side of equation (1) – i.e. to the weight of the diffuse gas layer in the total gravitational field. In low-density outer-disk regions where the diffuse gas dominates GBCs ($\Sigma_{\text{diff}} \rightarrow \Sigma$ and $\Sigma_{\text{GBC}} \rightarrow 0$), an approximate form for Σ_{SFR} is then given by

$$\Sigma_{\text{SFR,low}} \approx 3 \times 10^{-4} \text{ M}_\odot \text{ kpc}^{-2} \text{ yr}^{-1} \left(\frac{\Sigma}{10 \text{ M}_\odot \text{ pc}^{-2}}\right) \left[1 + 3 \left(\frac{Z'_d\Sigma}{10 \text{ M}_\odot \text{ pc}^{-2}}\right)^{0.4}\right] \times$$
$$\left[\frac{2}{\alpha}\left(\frac{\Sigma}{10 \text{ M}_\odot \text{ pc}^{-2}}\right) + \left(\frac{50\tilde{f}_w}{\alpha}\right)^{1/2}\left(\frac{\rho_{\text{sd}}}{0.1 \text{ M}_\odot \text{ pc}^{-3}}\right)^{1/2}\right] \tag{4}$$

(see eqs. 22 and A13 in OML10). The numerical coefficient in equation (4) is calibrated based on the local Milky Way value $\Sigma_{\text{SFR},0} = 2.5 \times 10^{-3} \text{ M}_\odot \text{ kpc}^{-2} \text{ yr}^{-1}$ (Fuchs et al. 2009).

In the case when $\Sigma_{\text{GBC}}/\Sigma$ is non-negligible, in order to obtain a closed set of equations, OML10 made the additional assumption that star formation within GBCs has a gas consumption timescale $t_{\text{SF,GBC}}$ so that

$$\Sigma_{\text{SFR}} = \frac{\Sigma_{\text{GBC}}}{t_{\text{SF,GBC}}} = \frac{\Sigma - \Sigma_{\text{diff}}}{t_{\text{SF,GBC}}}. \tag{5}$$

If GBCs have relatively uniform properties, then $t_{\text{SF,GBC}}$ will be relatively constant. By equating (2) and (3), and combining with equation (5), OML10 obtained a cubic equation that can be solved for Σ_{SFR} as a function of Σ and ρ_{sd} in the general case; an approximate form is given by

$$\Sigma_{\text{SFR}} \approx \left[\frac{t_{\text{SF,GBC}}}{\Sigma} + \frac{1}{\Sigma_{\text{SFR,low}}}\right]^{-1} \tag{6}$$

(see eqs. 23 and A14 in OML10). Note that for low surface density outer disks, equation (4) is recovered and Σ_{SFR} is independent of $t_{\text{SF,GBC}}$ – i.e. the star formation rate becomes independent of the rate at which gas in GBCs collapses to make stars.

OML10 took $t_{\text{SF,GBC}} = 2 \text{ Gyr}$ based on the empirical linear correlation (Bigiel et al. 2008) between the molecular mass in CO and the SFR at 750 pc scale for a set of disk galaxies (at moderate $\Sigma \lesssim 100 \text{ M}_\odot \text{ pc}^{-2}$),

and adopted $\alpha \approx 5$ and $\tilde{f}_w \approx 0.5$ as typical values based on observations of the Milky Way and other well-studied disk galaxies. If the same set of parameters is adopted for all galaxies (note that the dependence on $\tilde{f}_w/\alpha$ in equation 4 is weak: $\Sigma_{SFR} \propto (\tilde{f}_w/\alpha)^{0.5}$), Σ_{SFR} is a function of just Σ and ρ_{sd}. OML10 applied this formulation to azimuthally-averaged data for a sample of spiral galaxies to predict Σ_{SFR} as a function of galactocentric radius R. The resulting predicted profiles of Σ_{SFR} are overall in remarkably good agreement with the observations. For a few galaxies, however, observed values of Σ_{SFR} are offset from the prediction. The difference may owe to different values of α, $\tilde{f}_w$, and/or $t_{SF,GBC}$ from the adopted values, or to effects associated with azimuthal averaging when there is strong spiral structure. It should also be noted that there are still significant uncertainties in the observations, which might lead to offsets with respect to the theory. Empirical determinations of Σ and $t_{SF,GBC}$ are uncertain since some gas may be undetected in both 21 cm and CO lines, and since the conversion factor X_{CO} from CO to H_2 can vary by a factor ~ 2 (X_{CO} varies even more at low metallicity, and where $\Sigma \gtrsim 100 \, M_\odot \, pc^{-2}$). The age of the young-star population, as well as the treatment of extended vs. concentrated tracers of star formation, can also affect the empirical estimates of Σ_{SFR}. In addition, as discussed by OML10, values of ρ_{sd} are uncertain as stellar disk thickness estimates for face-on galaxies are obtained via scaling relations rather than being directly measured.

In this paper, we focus on the low-Σ case, corresponding to outer disks where the gas is primarily diffuse and atomic. In this regime, Σ_{SFR} is predicted to depend on α and $\tilde{f}_w$ but not on $t_{SF,GBC}$, according to equation (4). Using our numerical simulations, in which Σ and ρ_{sd} are independent variables, we can directly test the primary assumptions of the OML10 theory. Since we can measure α, $\tilde{f}_w$, Σ_{diff} (and $\Sigma_{GBC} = \Sigma - \Sigma_{diff}$) together with P_{th} from the simulation outputs for any model, we can test whether the measured midplane thermal pressure in fact agrees with the dynamical equilibrium value $P_{th,DE}$ predicted by equation (2). We can also investigate whether the measured midplane P_{th} is close to P_{two}, following the hypothesis of OML10 that the system evolves to a state of thermal equilibrium having both a warm and cold atomic phase. Similarly, we can test whether the sum of the measured thermal and turbulent pressures $P_{th} + \rho_0 v_{z,diff}^2 = P_{tot}$ is consistent with the dynamical equilibrium prediction of equation (1) (since the present simulations do not include magnetic fields, cosmic rays, or radiation pressure, these terms do not enter P_{tot}). Further, we can check whether our numerical results for α and $\tilde{f}_w$ agree with empirically-estimated values, and explore how much variation in α and $\tilde{f}_w$ there is among models with different Σ and ρ_{sd}. Finally, we can compare the value of Σ_{SFR} from the simulations with the theoretical prediction based on simultaneous thermal and dynamical equilibrium (cf. equation 4).

In addition to testing the theory of OML10, we can use our numerical simulations to test more general ideas related to the self-regulation of star formation, as introduced by OS11. We consider the situation in which the ISM is dominated by diffuse gas, so that $\Sigma_{GBC}/\Sigma_{diff} \to 0$ and $\Sigma_{diff} \to \Sigma$. We also assume the effective pressure is dominated by thermal and turbulent terms[3], and take $\zeta_d \approx 1/\pi$ and $c_w^2 \tilde{f}_w \alpha = \sigma_{z,diff}^2 \to \sigma_z^2$

---

[3]That is, we assume cosmic ray, magnetic field, and radiation effects are unimportant – see OML10 and OS11 for an evaluation and discussion of these.

so that equation (1) for the weight becomes

$$P_{\text{tot,DE}} = \frac{\pi G \Sigma^2}{4} \left\{ 1 + \left[1 + \frac{32 \sigma_z^2}{\pi^2 G} \frac{\rho_{\text{sd}}}{\Sigma^2} \right]^{1/2} \right\}. \tag{7}$$

A simplified expression for $P_{\text{tot,DE}}$, within 20% of equation (7), is

$$
\begin{aligned}
P_{\text{tot,DE}} \quad &\approx \quad \frac{\pi G \Sigma^2}{2} + \Sigma (2 G \rho_{\text{sd}})^{1/2} \sigma_z \\
&= \quad 10^4 k_B \, \text{cm}^{-3} \, \text{K} \left(\frac{\Sigma}{10 \, \text{M}_\odot \, \text{pc}^{-2}} \right) \times \\
&\quad \left[0.33 \left(\frac{\Sigma}{10 \, \text{M}_\odot \, \text{pc}^{-2}} \right) + 1.4 \left(\frac{\rho_{\text{sd}}}{0.1 \, \text{M}_\odot \, \text{pc}^{-3}} \right)^{1/2} \left(\frac{\sigma_z}{10 \, \text{km s}^{-1}} \right) \right].
\end{aligned}
\tag{8}
$$

The vertical dynamical equilibrium equation is

$$P_{\text{th}} + P_{\text{turb}} = \rho_0 v_{\text{th,diff}}^2 + \rho_0 v_{\text{z,diff}}^2 = \rho_0 \sigma_z^2 = P_{\text{tot,DE}}. \tag{9}$$

As noted above, it is expected that $P_{\text{th}} = \rho_0 v_{\text{th,diff}}^2 \propto \Sigma_{\text{SFR}}$ in a state of thermal equilibrium. In addition, OS11 argued that if mechanical feedback from star formation provides the dominant contribution to the vertical turbulent motions, then the turbulent pressure P_{turb} should also scale roughly linearly with Σ_{SFR}, as

$$P_{\text{turb}} = f_p \frac{p_*}{4 m_*} \Sigma_{\text{SFR}}. \tag{10}$$

Here, p_* is the mean radial momentum injected by each massive star, m_* is the total mass in stars formed per massive star, and the order-unity coefficient f_p parameterizes the details of turbulent momentum injection and dissipation. When turbulence dominates the pressure and self-gravity dominates the vertical weight, equations (7), (9) and (10) with $f_p \approx 1$ combine to yield a prediction that $\Sigma_{\text{SFR}} \approx 2 \pi G \Sigma^2 m_* / p_*$. OS11 found that this prediction is in good agreement with both numerical simulations (for a cold-gas dominated ISM) and with observations of molecule-dominated starburst regions with $\Sigma \gtrsim 100 \, \text{M}_\odot \, \text{pc}^{-2}$.

More generally, if star formation is responsible for both heating and driving vertical motions in the diffuse ISM, we expect the thermal and turbulent pressure contributions to scale roughly linearly with Σ_{SFR}. Normalizing relative to convenient dimensional units for observational comparison, we can define

$$\frac{P_{\text{th}}/k_B}{10^3 \, \text{cm}^{-3} \, \text{K}} \quad \equiv \quad \eta_{\text{th}} \frac{\Sigma_{\text{SFR}}}{10^{-3} \, \text{M}_\odot \, \text{kpc}^{-2} \, \text{yr}^{-1}} \tag{11}$$

$$\frac{P_{\text{turb}}/k_B}{10^3 \, \text{cm}^{-3} \, \text{K}} \quad \equiv \quad \eta_{\text{turb}} \frac{\Sigma_{\text{SFR}}}{10^{-3} \, \text{M}_\odot \, \text{kpc}^{-2} \, \text{yr}^{-1}}. \tag{12}$$

The parameters η_{th} and η_{turb} are yield coefficients that measure the efficacy of feedback. For the fiducial parameters adopted in OML10, $\eta_{\text{th}} = 1.2[0.25 + 0.75 Z'_d (\Sigma/10 \, \text{M}_\odot \, \text{pc}^{-2})^{0.4}]^{-1}$, where the factor in square brackets is unity in the Solar neighborhood. For the fiducial value $p_*/m_* = 3000 \, \text{km s}^{-1}$ adopted in OS11 (assuming supernovae are the most important sources of momentum), $\eta_{\text{turb}} = 3.6 f_p$. Note that with the

heating and turbulent driving yield coefficients as defined in equations (11) and (12), $\alpha = (P_{th} + P_{turb})/P_{th} = 1 + \eta_{turb}/\eta_{th}$ if only thermal and turbulent stresses contribute to the effective midplane pressure. We thus expect $\eta_{th} + \eta_{turb} \sim 1.2 + 3.6 \sim 5$ and $\alpha \sim 1 + (3.6/1.2) = 4$ under conditions similar to the Solar neighborhood. The latter is comparable to the value $\alpha = 5$ adopted in OML10 for comparisons of equation (6) with observations of Σ_{SFR}. By exploring the relations between the measured values of P_{th}, P_{turb}, and Σ_{SFR} in our simulations, we can numerically evaluate η_{th} and η_{turb}, testing whether these quantities (and therefore α) are indeed near-constant.

Combining equations (9), (11) and (12), the self-regulated star formation rate in a diffuse-gas-dominated region where the pressure is controlled by energy and momentum feedback from massive stars has the form

$$\Sigma_{SFR} = 2 \times 10^{-3} \; M_\odot \; kpc^{-2} \; yr^{-1} \left(\frac{\eta_{th} + \eta_{turb}}{5} \right)^{-1} \frac{P_{tot,DE}/k_B}{10^4 \; cm^{-3} \, K}. \tag{13}$$

For outer-disk regions, equation (7) or (8) may be used for the ISM weight $P_{tot,DE}$. In galactic-center regions where the bulge potential exceeds that of the disk, $\rho_{sd} \rightarrow \rho_b/3$ for ρ_b the bulge stellar density (see OS11).

For very dust-poor systems, FUV radiation escapes more easily from star-forming regions and penetrates further in the diffuse ISM, which may make the heating yield η_{th} comparable to or even larger than η_{turb} (see OML10 and Bolatto et al. 2011). Alternatively, in regions where Σ is extremely high and reprocessed IR radiation is trapped, radiation pressure becomes important and a term $\eta_{rad} \propto \Sigma \kappa_{IR}$ would be included in equation (13). Since the cosmic ray and magnetic pressures presumably increase with higher Σ_{SFR} in analogy with equations (11) and (12), corresponding feedback terms could be included in equation (13), with the values of η_{CR} and η_{mag} appropriately taking account of differing vertical scale heights compared to the neutral, star-forming gas (see OS11).

Using our present simulations, we can test whether the generalized feedback-regulated star formation prediction $\Sigma_{SFR} \propto P_{tot,DE}$ is satisfied. We will also compare our results to the power-law form $\Sigma_{SFR} \propto \Sigma^{1+p}$ traditionally used in fitting observations, and to the form $\Sigma_{SFR} \propto \Sigma \rho_0^{1/2}$ that is frequently adopted in numerical simulations of galaxy formation/evolution in the cosmological context.

3. Numerical Methods and Models

3.1. Basic Equations

The numerical models of this paper investigate thermal and dynamical evolution of gas in a vertically stratified, differentially rotating, self-gravitating galactic disk under the influence of interstellar cooling, heating, and radiative and mechanical feedback from star formation. We set up a local Cartesian frame whose center is located at a galactocentric radius R_0 and rotates with an angular velocity $\Omega = \Omega(R_0)$. In this local frame, $x \equiv R - R_0$, $y \equiv R_0(\phi - \Omega t)$, and z represent the radial, azimuthal, and vertical coordinates, respectively. Our simulation domain is a two-dimensional rectangular region with size $L_x \times L_z$ in the $\hat{\mathbf{x}} - \hat{\mathbf{z}}$ plane with $y = 0$ (hereafter XZ plane), representing a radial-vertical slice of the disk, although we implicitly consider the thickness $L_y (\ll L_x, L_z)$ in the y-direction for the purposes of computing star formation rates and

momentum feedback (see Section 3.2.1). We include nonzero velocity in the y-direction in order to treat epicyclic motions self-consistently. The equilibrium background velocity relative to the center ($x = z = 0$) of the simulation domain is given by $\mathbf{v}_0 = -q\Omega x\hat{\mathbf{y}}$, where $q \equiv -(d\ln\Omega/d\ln R)|_{R_0}$ is the local dimensionless shear rate. In terms of q, the epicycle frequency κ is given by $\kappa^2 = (4-2q)\Omega^2$. We assume a flat rotation curve so that $q = 1$ and $\kappa = \sqrt{2}\Omega$.

We expand the basic equations of hydrodynamics in the local frame, neglecting terms arising from the curvilinear geometry. The resulting shearing-sheet equations (e.g. Kim et al. 2002; Piontek & Ostriker 2007) are

$$\frac{\partial \rho}{\partial t} + \nabla \cdot (\rho\mathbf{v}) = 0, \tag{14}$$

$$\frac{\partial \mathbf{v}}{\partial t} + \mathbf{v} \cdot \nabla\mathbf{v} = -\frac{1}{\rho}\nabla P - 2\Omega \times \mathbf{v} + 2q\Omega^2 x\hat{\mathbf{x}} - \nabla\Phi + \mathbf{g}_{sd}, \tag{15}$$

$$\frac{\partial e}{\partial t} + \nabla \cdot (e\mathbf{v}) = -P\nabla \cdot \mathbf{v} - \rho\mathcal{L} + \mathcal{K}\nabla^2 T, \tag{16}$$

$$\nabla^2\Phi = 4\pi G\rho, \tag{17}$$

where Φ is the self-gravitational potential of the gas, $\mathbf{g}_{sd}$ is the external gravity from the stellar disk and the dark matter halo, $\rho\mathcal{L}$ is the net cooling function, and $\mathcal{K}$ is the thermal conductivity. Assuming that the gas is predominantly atomic and has cosmic abundances, $P = 1.1nk_BT$ is the gas pressure where $n = \rho/(1.4m_p)$ is the number density of hydrogen nuclei. We adopt an ideal gas law so that the internal energy density is given by $e = P/(\gamma-1)$ with index $\gamma = 5/3$. For the external gravity, we take the simple form

$$\mathbf{g}_{sd} = -4\pi G\rho_{sd}z\hat{\mathbf{z}}, \tag{18}$$

where ρ_{sd} is the midplane density of the stellar disk plus that of the dark matter halo. Since the scale height of the gas is much smaller than those of the stellar disk and the dark matter halo, $\mathbf{g}_{sd}$ given in equation (18), corresponding to vertically-uniform ρ_{sd}, is a reasonable approximation in studying dynamics of the gas.

The net cooling function per volume is given by $\rho\mathcal{L} \equiv n[n\Lambda(T)-\Gamma]$. For the cooling rate of the diffuse ISM, we adopt the fitting formula obtained by Koyama & Inutsuka (2002):

$$\Lambda(T) = 2 \times 10^{-19}\exp\left(\frac{-1.184 \times 10^5}{T+1000}\right) + 2.8 \times 10^{-28}\sqrt{T}\exp\left(\frac{-92}{T}\right) \text{ erg cm}^3 \text{ s}^{-1}, \tag{19}$$

with temperature T in degrees Kelvin. Cooling at low T is dominated by the 158μm fine-structure line of C II, whereas cooling at high T is dominated by Lyα line emission; both lines are collisionally excited. The heating rate Γ is dominated by the photoelectric effect on small dust grains and polycyclic aromatic hydrocarbons (PAHs) by FUV photons with energy $6\text{ eV} < h\nu < 13.6\text{ eV}$ (Bakes & Tielens 1994). The diffuse FUV radiation field, with intensity J_{FUV}, is produced by young O and B stars and therefore should depend on recent star formation. We thus allow Γ to vary with time, while keeping Γ uniform throughout the simulation box (i.e. J_{FUV} is treated as spatially constant). We follow Koyama & Inutsuka (2002) in adopting a fiducial heating rate in the Solar neighborhood $\Gamma_0 = 2 \times 10^{-26}$ erg s^{-1}. In thermal equilibrium ($\rho\mathcal{L} = 0$) for this cooling function, two stable phases co-exist for a range of densities and pressures: the maximum

pressure for the warm phase is $P_{max}/k_B = 5.5 \times 10^3(\Gamma/\Gamma_0)$ cm^{-3} K occurring at $T_{max} = 5000$ K and $n_1 = 1.0(\Gamma/\Gamma_0)$ cm^{-3}, and the minimum pressure for the cold phase is $P_{min}/k_B = 1.8 \times 10^3(\Gamma/\Gamma_0)$ cm^{-3} K at $T_{min} = 188$ K and $n_2 = 8.7(\Gamma/\Gamma_0)$ cm^{-3}. The two-phase pressure is thus given by $P_{two}/k_B \equiv (P_{min}P_{max})^{1/2}/k_B = 3.1 \times 10^3(\Gamma/\Gamma_0)$ cm^{-3} K. For Solar-neighborhood conditions, P_{two} is essentially the same as adopted in OML10, $P_{two}/k_B = 3000$ cm^{-3} K (see equation 3). We describe our prescription for connecting Γ with the (time-dependent) star formation rate, including metagalactic FUV radiation, in § 3.2.2.

Thermal conduction plays an important role in the development of thermal instability (TI). Conduction not only sets the critical wavelength (the "Field length") of TI (Field 1965), but also determines the thickness of interface layers between cold and warm phases (Begelman & McKee 1990). Inclusion of thermal conductivity is therefore essential to resolve TI in numerical simulations (Koyama & Inutsuka 2004; Piontek & Ostriker 2004; Kim et al. 2008). A realistic value of thermal conductivity in the diffuse ISM at $T < 10^4$ K is $\mathcal{K} \sim 2.5 \times 10^3 T^{1/2}$ erg s^{-1} cm^{-1} K^{-1} (Parker 1953). The corresponding Field length is then $\lambda_F \sim 0.2$ pc for the typical density $n = 1$ cm^{-3} and temperature $T = 10^3$ K of the thermally unstable gas, which would require an extremely fine numerical grid $\Delta x \lesssim \lambda_F/3$ in order for TI to be resolved. In addition, hydrodynamic simulations involving supersonic turbulence inherently suffer from a significant level of numerical diffusion (e.g., Gazol et al. 2005; Kim et al. 2008), which is larger than the physical conductivity unless Δx is extremely small. Adopting a realistic value of $\mathcal{K}$ is therefore prohibitively expensive for multi-dimensional simulations in kpc-scale numerical boxes. Fortunately, however, dynamics on larger scales are not sensitive to the exact conduction scale, similar to large-scale dynamics in supersonic flows being insensitive to the exact thickness of shocks. In this paper, we therefore adopt a numerical conductivity of $\mathcal{K} = 4 \times 10^7$ erg s^{-1} cm^{-1} K$^{-1}/[1+(0.05$ cm$^{-3}/n)]$ as in Koyama & Ostriker (2009a), which enables us to resolve the Field length numerically, and limits thermal conduction in low-density regions.

We solve the time-dependent partial differential equations (14)-(17) using a modified version of the *Athena* code (Stone et al. 2008; Stone & Gardiner 2009). *Athena* employs a single-step, directionally unsplit Godunov method for (magneto)hydrodynamics in multispatial dimensions, providing several schemes for integration in time, spatial reconstruction, and solution of the Riemann problem. We use the van Leer algorithm (Stone & Gardiner 2009) for integration, with piecewise linear reconstruction and the HLLC Riemann solver. We solve the net cooling function based on implicit time integration using Simpson's rule (e.g., Koyama & Ostriker 2009a) with a limit for the maximum temperature change of 50%. We also use an explicit conduction solver for isotropic thermal conduction, and revert to first order flux updates if a negative density appears during the higher-order update (Lemaster & Stone 2009). The gravitational potential is calculated using fast Fourier transforms in disk geometry with vacuum boundary conditions in the *z*-direction (Koyama & Ostriker 2009a). At the *x*-boundaries, we apply shearing-periodic boundary conditions (Hawley et al. 1995). In the *z*-direction, we adopt periodic boundary conditions for the hydrodynamic variables so as to maintain a constant mass within the domain. By running comparison models using outflow boundary conditions in *z*, we have checked that the boundary conditions do not affect the simulation outcomes significantly.

3.2. Prescription for Star Formation Feedback

In our simulations, self-gravitational collapse and ensuing feedback from star formation control both thermal and dynamical evolution of the model ISM. We consider both mechanical (momentum input) and radiative (thermal energy input) feedback effects. Mechanical feedback drives turbulence that supports the disk in the vertical direction, while radiative feedback affects the thermal pressure by changing the heating rate. In this section, we detail our prescription for star formation feedback.[4]

3.2.1. Mechanical Feedback

Star formation in our models occurs only inside clouds where the gas density is larger than a critical value. The threshold density $\rho_{\rm cr}$ should be large enough for star formation to occur only in self-gravitating regions. In addition, these self-gravitating regions should be resolved on the grid, i.e. the Jeans wavelength $\lambda_J(\rho_{\rm cr}) = [\pi c_{\rm cr}^2/(G\rho_{\rm cr})]^{1/2}$ should exceed the grid spacing Δx (taken to be 1 pc in our models), where $c_{\rm cr}$ denotes the thermal speed at the threshold temperature $T_{\rm cr}$. Since the cooling time is very short, dense clouds are generally in thermal equilibrium, and $n_{\rm cr} = \Gamma/\Lambda(T_{\rm cr})$. Equation (19) then yields

$$\lambda_J \approx 1.4 T_{\rm cr}^{3/4} e^{-46/T_{\rm cr}} (\Gamma/\Gamma_0)^{-1/2} \text{ pc}, \tag{20}$$

for $T \lesssim 100$ K. For a fixed λ_J, we obtain $T_{\rm cr}$ (and hence $n_{\rm cr}$) as a function of Γ/Γ_0. A simple power-law fit for $\lambda_J = 2.7$ pc gives $n_{\rm cr} \approx 500(\Gamma/\Gamma_0)^{0.2}$ cm^{-3}, which we take as the threshold density for star formation in our simulations. Although slightly lower threshold density would be needed to meet the Truelove criterion $\lambda_J/\Delta x > 4$ (Truelove et al. 1997, 1998) and limit artificial fragmentation in collapsing clouds, our choice is acceptable in the current context since our aim is not to follow cloud collapse and fragmentation but instead to disperse self-gravitating clouds by turning on star formation feedback, as explained below.

Not all clouds with $\rho \geq \rho_{\rm cr}$ immediately undergo gravitational collapse and star formation, since the star formation efficiency and the computational time step should be considered as well. Let us consider a star-forming region with density $\rho \geq \rho_{\rm cr}$. Assuming that our simulation domain represents a two-dimensional slab with thickness L_y in the y-direction, the mass in the cloud above the threshold is $M_{\rm cl} = L_y \int_{\rho \geq \rho_{\rm cr}} \rho dx dz$. For the thickness of the slab, we take $L_y = 2r_{\rm sh}$, where $r_{\rm sh}$ is the initial radius of an SN shell explained below. This choice of L_y is due to the fact that the most significant feedback in the simulation domain comes from SN events occurring within $2r_{\rm sh}$ in the y-direction. The SFR expected from the cloud is

$$\dot{M}_* = \epsilon_{\rm ff} \frac{M_{\rm cl}}{t_{\rm ff}(\rho)} \tag{21}$$

---

[4]Other recent numerical studies of the ISM have used somewhat different prescriptions for radiative and mechanical feedback from those we adopt. For example, Joung et al. (2009) adopted $\Gamma \propto \Sigma_{\rm gas}^{0.4}$ together with type-II SN rates scaling as $\Sigma_{\rm SN} \propto \Sigma_{\rm gas}^{1.4}$; Agertz et al. (2009) included feedback from supernovae based on a volumetric star formation rate $\rho_{\rm SFR} \propto \rho_{\rm gas}^{1.5}$ but did not include diffuse UV heating; and Tasker (2011) adopted a photoelectric heating rate that declines exponentially outward, but did not include mechanical feedback from supernovae.

where ϵ_{ff} is the star formation efficiency per free-fall time, $t_{\text{ff}}(\rho) \equiv (3\pi/(32G\rho))^{1/2}$. We take $\epsilon_{\text{ff}} = 0.01$ as a fiducial value consistent with theory and observations (Krumholz & McKee 2005; Krumholz & Tan 2007). The probable number of massive stars to form within the cloud in a time interval Δt is then given by

$$\mathcal{N}_* = \frac{\dot{M}_*}{m_*}\Delta t, \tag{22}$$

where m_* is the total mass of stars in all masses formed per massive star. We define massive stars as those that undergo supernovae, and adopt $m_* = 100\,\text{M}_\odot$ for all simulations consistent with the initial mass function of Kroupa (2001). For a given computational time step Δt, $\mathcal{N}_*$ calculated from equation (22) is typically $\sim 10^{-4} - 10^{-3}$ (as small as $\sim 10^{-6}$ immediately after SN explosions due to small time step), much smaller than unity. Therefore, in zones where $\rho \geq \rho_{\text{cr}}$ we generate a uniform random number $\tilde{\mathcal{N}} \in [0, 1)$ at each time step, and turn on feedback only provided $\mathcal{N}_* > \tilde{\mathcal{N}}$.

We implement mechanical feedback from star formation in a very simple way, by injecting momentum in the form of an expanding spherical velocity distribution to represent the radiative stage of a SN (cf., Shetty & Ostriker 2008). As the initial radius of the shell in three dimensions, we take $r_{\text{sh}} = 10$ pc, corresponding to the SN shock radius at the shell formation time (Cioffi et al. 1988; Koo & Kang 2004). We assume the center of the sphere is at a location y_{off} distributed randomly in the range $|y_{\text{off}}| \leq r_{\text{sh}}$, so that the initial shell radius in the XZ plane (at $y = 0$) is $R_{\text{max}} \equiv (r_{\text{sh}}^2 - y_{\text{off}}^2)^{1/2}$, varying between 0 and r_{sh}. We use a random number to choose the value of y_{off} for each feedback event. When a feedback event occurs, we first redistribute mass, momentum, and thermal energy within a circular region of radius R_{max} by taking spatial averages. We then add to the momentum density in the x- and z-directions according to

$$\rho\mathbf{v}_{\text{sh,2D}} = \begin{cases} p_{\text{max}} \left(\frac{R}{r_{\text{sh}}^2}\right)\mathbf{R}, & R \leq R_{\text{max}}, \\ 0, & R > R_{\text{max}}, \end{cases} \tag{23}$$

where $\mathbf{R}$ is the position vector with respect to the center of the SN sphere in the XZ plane, and p_{max} is the momentum density at $R = R_{\text{max}}$. By requiring the mean momentum input from equation (23) (averaged over y_{off}) is equal to the outward momentum that a three-dimensional shell would have, one obtains $p_{\text{max}} = 15p_*/(32r_{\text{sh}}^3)$, where p_* is the total radial momentum in three dimensions. In all simulations, we take $p_* = 3 \times 10^5\,\text{M}_\odot\,\text{km s}^{-1}$ corresponding to the late stages of a single SN with energy $E_{\text{SN}} = 10^{51}$ erg (Cioffi et al. 1988). The velocity profile $v(R) \propto R^2$ is chosen to guarantee an initially divergence-free velocity field at $R = 0$.

We note a few caveats that should be kept in mind regarding our simplified prescription for star formation feedback. First, as our main focus is on the diffuse gas component (which dominates by mass), our treatment does not attempt to follow the evolution and destruction of star-forming clouds in detail. Thus, we do not introduce a time delay prior to the momentum injection, or separately model effects of expanding H II regions or winds (the former was previously considered in Koyama & Ostriker 2009a, which found that only relatively low levels of turbulence were induced in the diffuse ISM). In this first study, our goal is primarily to incorporate turbulent driving in the diffuse ISM at a realistic level for a given star formation rate, which is accomplished by simply injecting momentum impulsively. Future work should improve this

treatment, but experience with numerical models of turbulent giant molecular clouds has shown that much astronomical insight can be gained even when idealized treatments of turbulent driving are adopted (Mac Low & Klessen 2004; McKee & Ostriker 2007).

Second, although our feedback treatment aims to model turbulent driving in the neutral warm/cold ISM that is induced by SNe, our approach does not attempt to model the high-temperature interiors of SN remnants themselves. Previous work has shown that it is difficult to model SN explosions by injecting thermal energy in large scale simulations because of *overcooling*: radiative energy losses are too rapid due to lack of spatial resolution (Katz 1992). At resolution levels that are affordable, far too little thermal energy ends up being converted to kinetic energy; instead it is radiated away. In order to avoid overcooling, in some simulations radiative cooling is artificially turned off until blast waves have developed (e.g., Thacker & Couchman 2001; Agertz et al. 2011), or the initial sizes of regions where SN energy is injected are set such that the gas temperature $T \sim 10^7$ K, where a dip is present in the cooling function (Joung & Mac Low 2006). For simulations such as ours which include self-gravity, SN events occur within very dense regions. Since the cooling rate is proportional to the square of the gas density, experiments we conducted with thermal energy injection and a coronal-gas cooling function showed that the cooling time was still unrealistically short at the resolution of our simulations, even if we adjusted the gas temperature to the dip of cooling function. Thus, although hot gas created in SNe may be quite important in many ways (including driving galactic winds), the present models focus just on the warm/cold ISM and star formation, and leave the interesting issues of the hot ISM for future work.

3.2.2. Radiative Feedback

Since the photoelectric heating rate is proportional to the intensity of the FUV radiation field, we simply take $\Gamma \propto J_{\mathrm{FUV}}$, with a proportionality constant depending on the heating efficiency of small grains and PAHs (see e.g., Bakes & Tielens 1994). There are two sources of the FUV radiation field in outer disk: $J_{\mathrm{FUV,local}}$, the FUV radiation emitted by recently-formed OB stars locally in the disk, and $J_{\mathrm{FUV,meta}}$, the metagalactic FUV radiation field. Radiation originating in the inner regions of the galaxy could also reach the outer galaxy, but this contribution is smaller than the local radiation unless the optical depth is very low.

If FUV escapes into the diffuse ISM from star-forming regions at the midplane at rate per unit area Σ_{FUV}, then $J_{\mathrm{FUV}} = \Sigma_{\mathrm{FUV}}[1 - E_2(\tau_\perp/2)]/(4\pi\tau_\perp)$ for $\tau_\perp = \Sigma\kappa_{\mathrm{FUV}}$ the optical depth through the diffuse neutral ISM, and E_2 the second exponential integral. As the radiative transfer factor depends only logarithmically on $1/\tau_\perp$ at low optical depth, for simplicity OML10 adopted $J_{\mathrm{FUV}} \propto \Sigma_{\mathrm{FUV}} \propto \Sigma_{\mathrm{SFR}}$ for application to galaxies with dust abundance not far from Solar and a moderate range of diffuse-H I surface densities. In galaxies with very low dust abundance, UV may escape much more easily from star forming regions, and also travel further through the diffuse ISM. This would lead to an increase in both $\Sigma_{\mathrm{FUV}}/\Sigma_{\mathrm{SFR}}$ and $J_{\mathrm{FUV}}/\Sigma_{\mathrm{FUV}}$ relative to the Milky Way, so that the ratio $J_{\mathrm{FUV}}/\Sigma_{\mathrm{SFR}}$ could be much higher than in the Solar neighborhood. Bolatto et al. (2011) found that the warm H I and star formation content of the SMC indeed appears to require a higher ratio of $J_{\mathrm{FUV}}/\Sigma_{\mathrm{SFR}}$ than in normal disks like the Milky Way.

In this work, we assume the heating rate due to local FUV scales with the local star formation rate as $\Gamma/\Gamma_0 = f_{\rm rad}\Sigma_{\rm SFR}/\Sigma_{\rm SFR,0}$, where $\Sigma_{\rm SFR,0} = 2.5 \times 10^{-3}$ M$_\odot$ kpc^{-2} yr^{-1} is the SFR surface density in the Solar neighborhood (Fuchs et al. 2009) and $\Gamma_0 = 2 \times 10^{-26}$ erg s^{-1} (Koyama & Inutsuka 2002). The parameter $f_{\rm rad}$ thus implicitly includes the normalized heating efficiency of the FUV radiation, allows for additional forms of heating such as X-rays (see Wolfire et al. 1995, 2003), and would vary depending on details of radiative transfer. Note that $f_{\rm rad} = 4/[1 + 3(Z'_d\Sigma/10$ M$_\odot$ pc$^{-2})^{0.4}]$ is adopted in OML10 based on the fit in Wolfire et al. (2003); this has $f_{\rm rad} = 1$ in the Solar neighborhood.

The total volumetric heating rate is then written as

$$\Gamma = \Gamma_0 \left[f_{\rm rad} \left(\frac{\Sigma_{\rm SFR}}{\Sigma_{\rm SFR,0}} \right) + \left(\frac{J_{\rm FUV,meta}}{J_{\rm FUV,0}} \right) \right]. \tag{24}$$

Note that the heating by the metagalactic FUV given by the second term in equation (24) provides a minimum heating rate when $\Sigma_{\rm SFR}$ is extremely small. We adopt $J_{\rm FUV,meta} = 0.0024 J_{\rm FUV,0}$ (Sternberg et al. 2002), so that in practice $J_{\rm FUV,meta}$ is negligible in most cases. The cooling and heating rates we adopt give geometric-mean two-phase pressure equal to

$$P_{\rm two}/k_{\rm B} = 1.2 \times 10^3 \text{ cm}^{-3} \text{ K} f_{\rm rad} \left(\frac{\Sigma_{\rm SFR}}{10^{-3} \text{ M}_\odot \text{ kpc}^{-2} \text{ yr}^{-1}} \right). \tag{25}$$

Thus, comparing to equation (11), if we were to find $P_{\rm th} = P_{\rm two}$ for the mean midplane thermal pressure, it would imply $\eta_{\rm th} = 1.2 f_{\rm rad}$ for the dimensionless heating-feedback yield coefficient. As we shall show in Section 5.2, $P_{\rm th}$ at the midplane is in fact between +10% and −40% of $P_{\rm two}$, so that $\eta_{\rm th}$ remains very close to $1 \times f_{\rm rad}$.

In order to change the heating rate self-consistently, we need to calculate the recent SFR at each time step. We do this by counting the number of the recent SN events, so that the SFR surface density is calculated by

$$\Sigma_{\rm SFR} = \frac{N_{\rm SN} m_*}{L_x L_y t_{\rm bin}}, \tag{26}$$

where $t_{\rm bin}$ is the time bin over which the SFR is averaged, and $N_{\rm SN}$ denotes the total number of SN events that occurred during the time span $(t - t_{\rm bin}, t)$. We note that $\Sigma_{\rm SFR}$ corresponds to a space and time average of $\dot{M}_*$ divided by the surface area. Since only recent star formation contributes to gas heating via FUV radiation, if the simulations were in three dimensions and optical depth effects were included, the averages should be taken at least over $t_{\rm FUV} \times (\pi d^2)$ to cover the whole domain of influence, where $t_{\rm FUV} \sim 10$ Myr is the FUV luminosity-weighted lifetime of OB stars (Parravano et al. 2003) and $d \sim 200$ pc$/(\Sigma/10$ M$_\odot$ pc$^{-2})$ is the effective in-plane distance for radiation to travel.[5] However, our simulation domain represents a radial-vertical slab with effective thickness $L_y = 2r_{\rm sh} = 20$ pc in the y-direction, with $L_y \ll d$. Since the size of our domain in the x-direction is large enough ($L_x \gtrsim d$), it is desirable to take a temporal bin at least

---

[5]The effective in-plane distance for FUV radiation to travel is given by $d \sim 2H/(\Sigma\kappa_{\rm FUV})$ where H is the scale height of the gas disk and $\kappa_{\rm FUV} \sim 1-2 \times 10^{-21}$ cm^2(H atom)$^{-1} \sim 0.1$ pc^2 M$_\odot^{-1}$ is the dust opacity in the FUV band. By taking $H \sim 100$ pc, we have $d \sim 200$ pc$/(\Sigma/10$ M$_\odot$ pc$^{-2})$.

$t_{\rm bin} \sim t_{\rm FUV}(d/L_y) \sim 10 t_{\rm FUV}/(\Sigma/10\,{\rm M}_\odot\,{\rm pc}^{-2})$ in order to limit stochasticity in the heating rate. We thus set $t_{\rm bin}$ equal to a half of the orbital period (see below for definition). Since our set of model parameters is chosen to maintain $\Omega \propto \Sigma$, this implies $t_{\rm bin} \propto \Sigma^{-1}$. With this choice, $t_{\rm bin}(\Sigma/10\,{\rm M}_\odot\,{\rm pc}^{-2}) \sim 100\,{\rm Myr} \sim 10 t_{\rm FUV}$.

3.3. Model Parameters

Since the feedback parameters are all specified, we now turn to the disk parameters. Our initial conditions for the gaseous disk consist of warm-phase gas with uniform thermal speed $c_w = 7\,{\rm km\,s}^{-1}$. The gravitational susceptibility of the disk depends on three parameters: gas surface density Σ, the angular velocity of galactic rotation Ω, and the stellar plus dark matter density at the midplane $\rho_{\rm sd}$. Both Σ and Ω enter the Toomre stability parameter

$$Q_{\rm init} \equiv \frac{\kappa c_w}{\pi G \Sigma}, \tag{27}$$

while $\rho_{\rm sd}$ determines the degree of vertical disk compression induced by the stellar disk and dark matter halo. It is convenient to define

$$s_0 \equiv \frac{\pi G \Sigma^2}{2 c_w^2 \rho_{\rm sd}} = 0.28 \left(\frac{\Sigma}{10\,{\rm M}_\odot\,{\rm pc}^{-2}}\right)^2 \left(\frac{c_w}{7\,{\rm km\,s}^{-1}}\right)^{-2} \left(\frac{\rho_{\rm sd}}{0.05\,{\rm M}_\odot\,{\rm pc}^{-3}}\right)^{-1}, \tag{28}$$

which measures the relative strengths (in the vertical direction) of gas self-gravity and the external gravity from stars and dark matter (Kim et al. 2002). For Solar-neighborhood conditions, $s_0 \approx 0.3$. Assuming $s_0 \ll 1$, the equilibrium density distribution is a Gaussian profile

$$\rho(z) = \rho_0 \exp(-z^2/2H_w^2), \tag{29}$$

where $\rho_0 = \Sigma/[(2\pi)^{1/2} H_w]$ and

$$H_w = \frac{c_w}{(4\pi G \rho_{\rm sd})^{1/2}} = 134\,{\rm pc} \left(\frac{c_w}{7\,{\rm km\,s}^{-1}}\right) \left(\frac{\rho_{\rm sd}}{0.05\,{\rm M}_\odot\,{\rm pc}^{-3}}\right)^{-1/2}, \tag{30}$$

is the scale height.

To simulate disk evolution in a range of environments systematically, we vary Σ and $\rho_{\rm sd}$ while keeping $Q_{\rm init} = 2$ fixed, so that the angular velocity at the center of the domain varies as $\Omega = 28\,{\rm km\,s}^{-1}\,{\rm kpc}^{-1}(\Sigma/10\,{\rm M}_\odot\,{\rm pc}^{-2})$. We consider four main series of models: QA, QB, S, and G. The model parameters are summarized in Table 1. In Series QA and QB, $\rho_{\rm sd}$ varies as $\rho_{\rm sd} \propto \Sigma^2$ so that the stellar Toomre parameter $Q_s \propto \Omega/\sqrt{\rho_s} \propto Q\sqrt{s_0}$ implicitly has the same value for all members of each series. For the QA series, $s_0 = 0.28$ and for the QB series $s_0 = 0.07$. Thus, models in Series QB have four times larger $\rho_{\rm sd}$ (i.e. a more confining stellar vertical potential) than those with the same Σ in Series QA. The model Series QA and QB represent conditions typical in disk galaxies at different galactocentric radii, from mid-disks (i.e. slightly inside the Solar circle) to far outer disks (e.g., Koyama & Ostriker 2009a).[6] For Series S, we fix $\rho_{\rm sd}$ and vary Σ to

---

[6]Very far outer galaxies with negligible stellar disks and only dark matter contributing to $\rho_{\rm sd} \propto R^{-2}$ would have $s_0 = 2(\pi G \Sigma)^2 (c_w \Omega_{\rm dm})^{-2}$, which could reach unity, but these conditions are not studied in the current work.

explore the effect of the gas surface density independent of the strength of the external vertical gravity. In Series G, Σ and Ω are held constant, while ρ_{sd} varies; this allows us to isolate the effect of the external vertical gravity. Our fiducial model is Model QA10 with $\Sigma = 10$ M$_\odot$ pc^{-2}, $\Omega = 28$ km s^{-1} kpc^{-1}, and $\rho_{sd} = 0.05$ M$_\odot$ pc^{-3}; this model is similar to the Solar neighborhood. The corresponding orbital period is $t_{orb} = 2\pi/\Omega = 220$ Myr$(\Omega/28$ km s^{-1} kpc$^{-1})^{-1} = 220$ Myr$(\Sigma/10$ M$_\odot$ pc$^{-2})^{-1}$, which we use as the time unit in our presentation.

The model series above all have the same feedback parameters. In addition, we consider Series R, in which f_{rad} is varied to explore the effect of varying heating for a given Σ_{SFR}. All other parameters in Series R are the same as Model QA10 (which has $f_{rad} = 1$). We ran four models labeled R02, R05, R25, and R50 with $f_{rad} = 0.25$, 0.5, 2.5, and 5.0, respectively. Since the ratio of local heating rate to local SFR surface density $\Gamma/\Sigma_{SFR} \propto f_{rad}$ (see equation 24), larger f_{rad} implies a higher heating rate for a given Σ_{SFR}, corresponding to lower shielding (e.g. from lower dust abundance) than in the Solar neighborhood. Smaller f_{rad} corresponds to higher shielding. In reality, f_{rad} should depend on both dust abundance and the total column of gas, since both of these can affect shielding. For the present study, we simply treat f_{rad} as an autonomous variable in order to explore effects of varying shielding (or heating efficiency, which for present purposes is equivalent).

For the vertical extent of our simulation boxes, we take $L_z = 4H_w$ (this varies depending on the model; see Table 1). In the horizontal direction, we take $L_x = 512$ pc as the standard value. In order to check the effect of the box size, we have run Model QA10x2, which has the same parameters as Model QA10 except the horizontal box size is extended to $L_x = 1,024$ pc; this model confirmed that overall evolution and statistical properties are indeed similar. We vary the number of zones from model to model to make the grid spacing $\Delta x = \Delta z = 1$ pc for all the models. In order to seed TI, isobaric perturbations consisting of a Gaussian random field with flat power for $1 \leq kL_z/2\pi \leq 8$ and zero power for $kL_z/2\pi > 8$ are added to the initial density and temperature distributions. The amplitude of the initial perturbations is set to 10% of the midplane density. We evolve each model until $t/t_{orb} = 3$, well beyond the time required for the system to reach a quasi-steady state.

3.4. Classification of Gas Components

Before describing the simulation results, we establish terminology for the various gas components we shall discuss. In the neutral ISM, gas in GBCs and diffuse gas are distinguished based on whether the gravitational energy and total pressure significantly exceed that of the surrounding gas at similar z, or not. In general, the GBC component consists of the population of giant molecular clouds (GMCs), including both molecular gas inside GMCs and dense atomic shielding layers. Observations of the Milky Way (Solomon et al. 1987; Heyer et al. 2009; Roman-Duval et al. 2010) and Local Group galaxies (Bolatto et al. 2008) have reported that GMCs have similar surface densities $\Sigma_{GMC} \sim 100$ M$_\odot$ pc^{-2}, corresponding to $n_{GMC} \sim 40$ cm$^{-3}(M_{GMC}/10^6$ M$_\odot)^{-1/2}$. Since we do not take into account radiative transfer and formation of hydrogen and CO molecules explicitly, we cannot directly identify structures in our models that would be observed as GMCs. In this work, we simply define gas with $n \geq n_{GBC} = 50$ cm^{-3} as being within the

GBC component, since observed GMCs have comparable densities. We emphasize that this classification is essentially a nomenclature shorthand, allowing us to refer to the densest gas as the "GBC component". The designation of gas as "GBC" or "diffuse" component is not used in any way within the simulations themselves. We note that the density threshold for star formation (see section 3.2.1), which is much larger than $n_{\rm GBC}$, ensures that star formation in our numerical models takes place only within the GBCs.

The diffuse component, defined as gas with $n < n_{\rm GBC}$, consists of thermally-stable cold and warm phases as well as a thermally-unstable phase. We classify the phases of the diffuse component based on its density rather than temperature such that it is warm gas if $n < n_1$, cold gas if $n > n_2$, and unstable gas if $n_1 < n < n_2$ (see definitions of n_1 and n_2 following equation 19). Note that n_1 and n_2 depend on Γ (and hence $\Sigma_{\rm SFR}$) and thus vary with time. In what follows, $f_{\rm GBC}$ and $f_{\rm diff}$ denote the mass fractions of GBC and diffuse components in the whole gas, respectively. Similarly, the mass fractions of cold, unstable, and warm phases within the diffuse component are represented by f_c, f_u, and f_w, respectively. Note that $f_{\rm GBC} + f_{\rm diff} = 1$ and $f_c + f_u + f_w = 1$.

4. Simulation Results

In this section, we describe results of our numerical simulations. Our models evolve in a generally similar manner to those of Koyama & Ostriker (2009a), which also included self-gravity, radiative heating (at fixed Γ) and cooling, and feedback from star formation. In the models of Koyama & Ostriker (2009a), only feedback associated with H II regions was considered. H II regions were modeled by applying intense heating in dense enough regions that met criteria for star formation; expansion of the overpressured gas provided turbulent driving. Since SN explosions are more energetic than expanding H II regions, however, our present models achieve a higher (more realistic) level of turbulence at saturation than those in Koyama & Ostriker (2009a). Also, the variable radiative heating rate in the present simulations enables us to explore self-regulation of thermal pressures.

4.1. Overall Evolution

We begin by describing evolution of Model QA10x2, which has $\Sigma = 10\,{\rm M_\odot\,pc^{-2}}$ and $\rho_{\rm sd} = 0.05\,{\rm M_\odot\,pc^{-3}}$. Figure 1 displays snapshots for Model QA10x2 at $t/t_{\rm orb} = 0$, 0.1, and 0.2 to show early time evolution. The initial gas disk has a Gaussian density profile with scale height $H_w = 134$ pc and constant temperature, shown in Figure 1(a). Since the initial disk is out of thermal equilibrium, it rapidly evolves and separates into two phases, with a cold dense layer near the disk midplane sandwiched by diffuse warm gas at larger $|z|$. At the same time, TI develops locally, creating numerous cloudlets in the midplane dense layer. The cold midplane slab has a surface density of $\Sigma_c = 7\,{\rm M_\odot\,pc^{-2}}$ and a typical sound speed $c_c = 1\,{\rm km\,s^{-1}}$. The cold slab has Toomre stability parameter $Q_c \sim 0.3$ with Jeans length $\lambda_{\rm 2D,c} \equiv c_c^2/(G\Sigma_c) = 33$ pc, so that it is quite gravitationally unstable. The slab soon fragments gravitationally to form many dense clouds, which grow in size and mass by merger with their neighbors. Massive clouds undergo runaway collapse as self-gravity

dominates the internal pressure, eventually producing stars and SN explosions when the density exceeds ρ_{cr}. The first SN feedback event occurs at about $t/t_{orb} = 0.1$. Figure 1(*b*) shows formation of dense clouds and the first SN explosion from Model QA10x2. Subsequent SN events drive the gas disk into a turbulent state, as seen in Figure 1(*c*).

The kinetic energy associated with expanding shells disperses dense clouds in the midplane, and causes the disk to puff up in the vertical direction. Successive stages of gravitational contraction and feedback-induced expansion result in quasi-periodic oscillations of the disk thickness. Warm gas located ahead of the expanding shells is swept up by shocks and collected into the shells. Pre-existing dense gas becomes even denser from shock compression. Ensuing radiative cooling in the postshock regions increases the shell density (e.g., Mufson 1974; McCray et al. 1975). High-density expanding shells disintegrate due to a combination of dynamical processes, forming small dense cloudlets that subsequently merge together to grow into new dense clouds. These newly formed dense clouds collapse internally and create additional stars when their internal density exceeds the threshold value, leading to further SN feedback events that repeatedly stir up and restructure the surrounding medium.

Figure 2 plots temporal evolution of the mass fractions of the various gas components, the density-weighted vertical scale height

$$H \equiv \left(\frac{\int \rho z^2 dx dz}{\int \rho dx dz} \right)^{1/2} , \tag{31}$$

and the SFR surface density. The initial changes in the mass fractions and the disk scale height shown in Figure 2 reflect early-time thermal response of the gas to the net cooling function. The formation of new dense clouds is quickest at the compression phase of the disk oscillation, as evidenced by the negative correlation between f_{GBC} and H shown in Figure 2. Within a few tenths of an orbit, the system evolves into a quasi-steady state in the sense that Σ_{SFR}, gas fractions, and other statistical properties fluctuate but do not systematically change over time.

Notice that H in Figure 2 shows quasi-periodic oscillations over the entire evolution of Model QA10x2, which also produces temporal variations in other physical quantities. The dominant timescale is roughly half of the natural vertical oscillation period, $\sim 0.5(\pi/G\rho_{sd})^{1/2}$. The mean value and standard deviation of the disk scale height are $\langle H \rangle = 86$ pc and $\Delta H = 12$ pc, respectively, where the angle brackets $\langle \rangle$ denote a temporal average over $2 < t/t_{orb} < 3$. When the disk is compressed vertically, it produces more dense clouds and hence more active star formation. The enhanced radiative and mechanical feedback from star formation then increases the thermal pressure and the velocity dispersion of the gas, causing the disk to re-expand. Disk expansion temporarily suppresses star formation activity, which then reduces the total pressure and leads to a decrease in the disk scale height. At saturation, the mass fraction of the diffuse component in model QA10x2 has a mean value $\langle f_{diff} \rangle = 0.77$ and fluctuation amplitude of $\Delta f_{diff} \sim 0.06$. The cold, unstable, and warm phases amount to fractions $\langle f_c \rangle = 0.46$, $\langle f_u \rangle = 0.22$, and $\langle f_w \rangle = 0.32$, respectively, of the diffuse gas mass. The SFR surface density has a mean value $\langle \Sigma_{SFR} \rangle = 1.9 \times 10^{-3}$ $M_\odot$ kpc^{-2} yr^{-1} and standard deviation $\Delta \Sigma_{SFR} = 4.0 \times 10^{-4}$ $M_\odot$ kpc^{-2} yr^{-1}. Note that $\Delta \Sigma_{SFR}$ is small, since in evaluating Σ_{SFR} we have already time-averaged SN events over $t_{bin} = 0.5 t_{orb}$ (cf. Fig. 2).

Figure 3 displays the density structure (including newly formed dense clouds) and velocity field around an expanding shell at $t/t_{orb} = 2.22$, well after Model QA10x2 has reached a quasi-steady state. The expanding shell, near the center of the simulation box in Figure 3(a), was created by a SN event at $t/t_{orb} = 2.18$. Figure 3(b), showing a zoomed-in section of the shell, illustrates that dense (internal $n \sim 10^2 - 10^3$ cm^{-3}) clouds form in regions of converging velocity fields, indicated as white arrows. The mean velocities of the dense clouds, represented by black arrows, generally follow the background converging velocity fields (with an additional random component), suggesting that cloud collisions will ensue. The rectangular section marked in Figure 3(b) is enlarged in Figure 3(c) to show the internal velocity fields of three selected massive dense clouds. The internal one-dimensional velocity dispersion in each cloud is ~ 1 km s^{-1}, which is supersonic since the mean sound speed inside the dense clouds is ~ 0.5 km s^{-1}. The dense cloud near $(x, z) = (-175, -25)$ pc will have a star formation event at a time $\Delta t = 0.01 t_{orb}$ after this snapshot.

Figure 4(a) shows the distribution of the gas in the n–P plane from Model QA10x2, averaged over $t/t_{orb} = 2 - 3$. The colorbar labels the mass fraction in logarithmic scale. While a large fraction of the gas remains close to thermal equilibrium (given by the solid curve), a non-negligible portion is out of thermal equilibrium ($\sim 18\%$ by mass departs from equilibrium by $|\Delta \log P| > 0.15$), since the gas is continuously disturbed by turbulent motions.[7] The thermal equilibrium curve is for the time-averaged heating rate; fluctuations $\Delta \Gamma = 0.16 \Gamma_0$ relative to the mean value $\langle \Gamma \rangle = 0.76 \Gamma_0$ displace the equilibrium curve upward and downward. Variations in heating imply that gas can be out-of equilibrium with respect to the mean curve (even if instantaneous thermal equilibrium holds). Initially after a SN event, some cold gas is converted to the diffuse warm phase, while later shock compression and subsequent cooling during later stages of the shell expansion convert some warm gas to the cold phase.

Figures 4(b,c) plot the probability density functions (PDFs) of thermal pressure and number density distributions shown in Figure 4(a), respectively. Thick and thin lines denote the mass- and volume-weighted PDFs. The range of thermal pressure in our models spans more than three orders of magnitude, although most of the mass is near the mode of the PDF. The peak value of the pressure PDF corresponds to the mean thermal pressure at the midplane. The volume-weighted pressure PDF extends toward very small values mainly due to warm gas at high altitude, while self-gravitating dense clouds near the midplane occupy the high end of the mass-weighted pressure PDF. The mass-weighted density PDF shows the bimodal shape characteristic of the classical two-phase ISM (e.g., Field et al. 1969; Wolfire et al. 1995; Piontek & Ostriker 2004), although supersonic turbulent motions and frequent phase transitions increase the mass fraction in the unstable phase, making the peaks less prominent (e.g., Gazol et al. 2005; Gazol et al. 2009; Audit & Hennebelle 2005, 2010; Hennebelle & Audit 2007; de Avillez & Berry 2001; de Avillez & Breitschwerdt 2005; Piontek & Ostriker 2005, 2007; Joung & Mac Low 2006; Joung et al. 2009; Koyama & Ostriker 2009a).

Evolution of other models in Series QA is qualitatively similar to that of our standard model. One

---

[7]The thermal conductivity adopted is somewhat larger than the realistic value, and the numerical diffusion caused by large flow speeds also contributes, which may increase the unstable-mass fraction at the expense of the cold gas in our models (e.g., Kim et al. 2008).

notable trend is that physical quantities exhibit larger-amplitude fluctuations with decreasing Σ. In low-Σ models where SN events are rare and intermittent, even a single SN explosion stirs up the whole simulation domain because there is not enough mass to limit shell expansion. This gives rise to large variations in H, which in turn increases the dispersions of P_{th} and Σ_{SFR}, for lower-Σ models. In models with high Σ, on the other hand, SN events are frequent and spatially correlated. Shell expansion is frequently limited by surrounding dense gas and nearby SN shells. Consequently, the temporal changes of the disk scale height in these models are less dramatic than in low-density models.

Compared to Series QA, models in Series QB have smaller H, as a result of a more-confining vertical gravitational potential (four times larger ρ_{sd}). The resulting SFR is correspondingly larger in Series QB compared to Series QA. Series S and G also reach quasi-steady states, and their trends with increasing/decreasing Σ or ρ_{sd} follow the same patterns as in Series QA and QB. In particular, independent increases in either Σ or ρ_{sd} (with the other parameter controlled) produce an increase in Σ_{SFR}. The statistical properties of the models vary depending on the input "environmental" parameters (i.e. Σ and ρ_{sd}), as we shall describe and explore in the remainder of this paper.

4.2. Statistical Properties of the Gas

We have seen in Section 4.1 that after a brief transient, our models approach a quasi-steady state, which may be thought of as an approximate thermal and dynamical equilibrium (with fluctuations about the mean). In this subsection, we present the time-averaged values of the physical quantities that characterize the thermal and dynamical properties of the gas. These values will be used in Section 5 to compare our numerical results with the analytic predictions summarized in Section 2.

In our models, the total pressure at the midplane consists only of the thermal and turbulent components since we do not include a magnetic field. We measure these two pressures directly from simulation data as

$$P_{\text{th}} = \frac{\int_{z=-\Delta z/2}^{z=+\Delta z/2} \int P\Theta(n<n_{\text{GBC}})dxdz}{\int_{z=-\Delta z/2}^{z=+\Delta z/2} \int \Theta(n<n_{\text{GBC}})dxdz}, \tag{32}$$

$$P_{\text{turb}} = \frac{\int_{z=-\Delta z/2}^{z=+\Delta z/2} \int \rho v_z^2 \Theta(n<n_{\text{GBC}})dxdz}{\int_{z=-\Delta z/2}^{z=+\Delta z/2} \int \Theta(n<n_{\text{GBC}})dxdz}, \tag{33}$$

where $\Theta(X)$ is 1 if the logical argument 'X' is true and 0 otherwise. These definitions give volume-weighted averages of pressure for the diffuse component (all gas at $n < n_{\text{GBC}} = 50\,\text{cm}^{-3}$) at the midplane (the horizontal planes $z = \pm\Delta z/2$). Figure 5(a) plots as solid and dotted lines the midplane thermal and turbulent diffuse-gas pressures, respectively, in Model QA10x2 as functions of time. After a quasi-steady state is reached ($t/t_{\text{orb}} > 1$), the mean values are $\langle P_{\text{th}}/k_{\text{B}} \rangle = 1,680\,\text{cm}^{-3}\,\text{K}$ and $\langle P_{\text{turb}}/k_{\text{B}} \rangle = 5,440\,\text{cm}^{-3}\,\text{K}$, with fluctuation amplitudes $\Delta P_{\text{th}}/\langle P_{\text{th}} \rangle = 0.21$ and $\Delta P_{\text{turb}}/\langle P_{\text{turb}} \rangle = 0.52$. Since the midplane includes high-velocity injection regions associated with SN, there are large spikes in the midplane value of P_{turb}. The overall fluctuations of P_{th} and P_{turb} follow the pattern of variations in H due to vertical oscillations, as shown in Figure 2.

While we can measure midplane pressures in simulations, the most direct observables are mass-weighted velocity dispersions. We calculate the mass-weighted vertical turbulent and thermal velocity dispersions of the diffuse component using

$$v_{z,\mathrm{diff}} \equiv \left[\frac{\int \rho v_z^2 \Theta(n < n_{\mathrm{GBC}}) dx dz}{\int \rho \Theta(n < n_{\mathrm{GBC}}) dx dz} \right]^{1/2}, \quad v_{\mathrm{th,diff}} \equiv \left[\frac{\int P \Theta(n < n_{\mathrm{GBC}}) dx dz}{\int \rho \Theta(n < n_{\mathrm{GBC}}) dx dz} \right]^{1/2}. \tag{34}$$

The rms total velocity dispersion of the diffuse component in the vertical direction is given by $\sigma_{z,\mathrm{diff}} \equiv (v_{z,\mathrm{diff}}^2 + v_{\mathrm{th,diff}}^2)^{1/2}$. Figure 5(b) displays the time evolution of $v_{\mathrm{th,diff}}$ and $v_{z,\mathrm{diff}}$ in Model QA10x2 as solid and dotted lines, respectively. The vertical turbulent velocity dispersion saturates at $\langle v_{z,\mathrm{diff}} \rangle = 6.8$ km s^{-1} with relative fluctuation amplitude $\Delta v_{z,\mathrm{diff}} / \langle v_{z,\mathrm{diff}} \rangle = 0.30$, while the thermal component has a smaller mean value $\langle v_{\mathrm{th,diff}} \rangle = 3.7$ km s^{-1} and standard deviation $\Delta v_{\mathrm{th,diff}} = 0.2$ km s^{-1}. Many spikes in $v_{z,\mathrm{diff}}$ reflect energy injection events associated with SN explosions. Since the shock-heated gas occupies a very small volume only near the midplane, the thermal velocity dispersion $v_{\mathrm{th,diff}}$ averaged over the whole domain varies more smoothly than the volume-weighted mean P_{th} averaged only near the midplane.

Tables 2 and 3 list the mean values and standard deviations of several physical quantities characterizing the gas disk, for all models. Here and hereafter, we omit angle brackets for convenience; all the symbols represent time-averages over $t/t_{\mathrm{orb}} = 2-3$, unless stated otherwise. Column (1) labels each run as in Table 1. In Table 2, Column (2) gives the logarithm of Σ_{SFR} in units of M$_\odot$ kpc^{-2} yr^{-1}. Columns (3) and (4) give the logarithm of P_{th}/k_B and P_{turb}/k_B, respectively, in units of cm^{-3} K. Column (5) lists the midplane number density n_0 of hydrogen in units of cm^{-3} defined in analogy with equation (32) but for n rather than P in the integral. Column (6) gives the scale height of the diffuse gas $H_{\mathrm{diff}} \equiv [\int \rho z^2 \Theta(n < n_{\mathrm{GBC}}) dx dz / \int \rho \Theta(n < n_{\mathrm{GBC}}) dx dz]^{1/2}$ in units of pc.

In Table 3, Columns (2) and (3) give the turbulent and thermal velocity dispersions of the diffuse component in units of km s^{-1}, while Column (4) gives the mass-weighted vertical velocity dispersion for all the gas $\sigma_z \equiv [\int (\rho v_z^2 + P) dx dz / \int \rho dx dz]^{1/2}$ in units of km s^{-1}. Column (5) lists f_{diff}, the fraction of mass in the diffuse component (by definition, all gas at $n < n_{\mathrm{GBC}} = 50$ cm^{-3} is diffuse). In Columns (6) and (7), we list $\alpha \equiv (v_{\mathrm{th,diff}}^2 + v_{z,\mathrm{diff}}^2)/v_{\mathrm{th,diff}}^2$ and $\tilde{f}_w \equiv v_{\mathrm{th,diff}}^2/c_w^2$, respectively; these parameters are necessary to test the OML10 theory. Note that $\tilde{f}_w \approx f_w$ (the mass fraction of diffuse gas that is warm) since $v_{\mathrm{th,diff}}^2 = f_w c_w^2 + f_c c_c^2$ and the thermal speed c_w of the warm medium is an order of magnitude larger than that of the cold medium c_c. Also note that α in Table 3 (based on mass-weighted velocities or pressures averaged over the box) is close but not identical to the ratio $P_{\mathrm{tot}}/P_{\mathrm{th}}$ at the midplane. Finally, Column (8) gives the numerically-measured timescale to convert high-density gas into stars, $\tau_{\mathrm{SF,GBC}} \equiv (1 - f_{\mathrm{diff}})\Sigma/\Sigma_{\mathrm{SFR}}$ in Gyr units; here $1 - f_{\mathrm{diff}} = f_{\mathrm{GBC}}$ is simply defined as the mass fraction at $n > n_{\mathrm{GBC}} = 50$ cm^{-3}.

Figure 6 plots the mean values of turbulent and total velocity dispersions (a) $v_{z,\mathrm{diff}}$ (b) $\sigma_{z,\mathrm{diff}}$, and (c) σ_z as functions of Σ_{SFR} for all models except Series R. The mean values over the whole set of models shown in Figure 6 are $v_{z,\mathrm{diff}} = 6.8 \pm 0.6$ km s^{-1}, $\sigma_{z,\mathrm{diff}} = 7.7 \pm 0.6$ km s^{-1}, and $\sigma_z = 7.0 \pm 0.4$ km s^{-1}. It is clear that $\sigma_{z,\mathrm{diff}}$ increases slightly as Σ_{SFR} increases, while $v_{z,\mathrm{diff}} \sim \sigma_z \sim 7$ km s^{-1} is more-or-less constant in all models (excluding Series R). The slight increase of $\sigma_{z,\mathrm{diff}}$ with Σ_{SFR} is due to an increase of $v_{\mathrm{th,diff}}$ with a higher proportion of warm gas at higher Σ_{SFR}, although thermal speeds (averaged over both warm and cold

gas) are lower than turbulent speeds for all models except R50 (see Table 3).

The nearly constant value of $v_{z,\text{diff}}$, over two orders of magnitude in Σ_{SFR}, owes to a balance between driving and dissipation for the turbulent momentum (see Section 5.2 for a detailed discussion). The total vertical velocity dispersion for the whole gaseous medium is also nearly constant in all models, $\sigma_z \sim 7 \text{ km s}^{-1}$ (see Fig. 6c). This is because the higher proportion of warm gas in the diffuse medium (raising $\sigma_{z,\text{diff}}$ as Σ_{SFR} increases) is counterbalanced by a lower proportion of the gas being in the diffuse component (which has higher velocity dispersion than the dense, dynamically- and thermally-cold GBC component) at higher Σ_{SFR}. That is, with $\sigma_z \approx f_{\text{diff}}^{1/2} \sigma_{z,\text{diff}}$, the larger $\sigma_{z,\text{diff}}$ is offset by smaller f_{diff}, for models with higher Σ_{SFR}.

We note that the values of velocity dispersions given in Table 3 and plotted in Figure 6 are mass-weighted averages over the entire simulation volume rather than just averages at the midplane (which would be $v_{\text{th,mid}} = (P_{\text{th}}/\rho_0)^{1/2}$ and $v_{z,\text{mid}} = (P_{\text{turb}}/\rho_0)^{1/2}$, where $\rho_0 = 1.4 m_p n_0$). We report volume-averaged values because these are the closest to direct observables. However, the OML10 theory (and dynamical equilibrium considerations more generally) use midplane values of the pressure, which depend on midplane velocity dispersions. We have found $v_{\text{th,diff}}/v_{\text{th,mid}} \sim 1.3$ and $v_{z,\text{diff}}/v_{z,\text{mid}} \sim 1.3$ for all models. The reason for this difference is that the gas is somewhat differentially stratified, with cold phase preferentially concentrated near the midplane, which makes $v_{\text{th,mid}}$ slightly smaller value than $v_{\text{th,diff}}$. Also, since the gas density and the turbulent dissipation rate increase near the midplane, $v_{z,\text{mid}}$ is slightly smaller than $v_{z,\text{diff}}$ averaged over the whole volume.

Figure 7 plots the mean values of (a) α, (b) $\tilde{f}_w$, and (c) $f_w f_{\text{diff}}$ as functions of Σ_{SFR} for all models except Series R. There is a weak decreasing trend of α with Σ_{SFR}, but overall α has a small range, $\sim 3 - 6$. The small range of $\alpha = (v_{\text{th,diff}}^2 + v_{z,\text{diff}}^2)/v_{\text{th,diff}}^2$ implies that the ratio of turbulent to thermal pressure $P_{\text{turb}}/P_{\text{th}} = v_{z,\text{diff}}^2/v_{\text{th,diff}}^2$ in the diffuse gas is close to constant (for a given f_{rad}) over a very large range of Σ_{SFR}. The parameter $\tilde{f}_w$ increases as Σ_{SFR} increases since a higher heating rate increases the warm-gas mass fraction and $\tilde{f}_w = v_{\text{th,diff}}^2/c_w^2 = f_w + (1 - f_w)c_c^2/c_w^2 \approx f_w$. Note that $\alpha = 1 + (v_{z,\text{diff}}^2/c_w^2)/\tilde{f}_w$, so that with $c_w \sim v_{z,\text{diff}} \sim 7 \text{ km s}^{-1}$ (see Fig. 6), the decline in $\alpha \sim 1 + 1/\tilde{f}_w$ from ~ 6 to ~ 3 is just as expected when $\tilde{f}_w$ increases from ~ 0.2 to ~ 0.5. The mass fraction of warm gas in the whole medium $f_w f_{\text{diff}}$ is nearly constant, implying the warmer diffuse gas at higher Σ_{SFR} is offset by a higher fraction of the medium in a very dense component (here defined as $n > n_{\text{GBC}} = 50 \text{ cm}^{-3}$).

For Series R (see Tables 2 and 3), $v_{\text{th,diff}}$ and $\tilde{f}_w$ increase as f_{rad} increases (corresponding to increasing heating at given Σ_{SFR}). On the other hand, $v_{z,\text{diff}}$ decreases as f_{rad} increases, for the R series. Combining these effects, $\alpha = 1 + v_{z,\text{diff}}^2/v_{\text{th,diff}}^2$ decreases by nearly an order of magnitude for increasing f_{rad} in the R series. At large f_{rad}, $v_{\text{th,diff}}$ exceeds $v_{z,\text{diff}}$. On the other hand, $\sigma_{z,\text{diff}}$ and σ_z decrease only slightly as f_{rad} increases, while Σ_{SFR} decreases by a factor ~ 2. Thus, f_{rad} appears to affect primarily the energy distribution between thermal and turbulent components that results from star formation feedback, together with the proportions of cold and warm gas, for the parameter regime we have explored.

5. Test of the Thermal/Dynamical Equilibrium Model

5.1. Vertical Dynamical Equilibrium

Having obtained the statistical properties of the multiphase, turbulent gas from our time-dependent numerical simulations, we are now in a position to examine the validity of the assumptions made in OML10, and to compare our numerical results with the predictions of the OML10 analytic theory.

We first focus on the vertical force balance between (self plus external) gravity and total (thermal plus turbulent) pressure. If dynamical equilibrium holds, the total midplane pressure $P_{\rm tot}$ should match the vertical weight of diffuse gas, $P_{\rm tot,DE}$. Taking $\zeta_d = 1/\pi$, we rewrite equation (1) in terms of $f_{\rm diff} \equiv \Sigma_{\rm diff}/\Sigma$ and $\sigma_{\rm z,diff} = c_w(\tilde{f}_w\alpha)^{1/2}$ as

$$
\begin{aligned}
P_{\rm tot,DE} &= f_{\rm diff}\frac{\pi G\Sigma^2}{4}\left\{(2-f_{\rm diff})+\left[(2-f_{\rm diff})^2+\frac{32\sigma^2_{\rm z,diff}\rho_{\rm sd}}{\pi^2 G\Sigma^2}\right]^{1/2}\right\} \\[6pt]
&= 1.7\times10^3\,k_{\rm B}\,{\rm cm}^{-3}\,{\rm K}\,f_{\rm diff}\left(\frac{\Sigma}{10\,{\rm M}_\odot\,{\rm pc}^{-2}}\right)^2\times \\[6pt]
&\quad\left\{(2-f_{\rm diff})+\left[(2-f_{\rm diff})^2+37\left(\frac{\sigma_{\rm z,diff}}{7\,{\rm km\,s}^{-1}}\right)^2\left(\frac{\rho_{\rm sd}}{0.1\,{\rm M}_\odot\,{\rm pc}^{-3}}\right)\left(\frac{\Sigma}{10\,{\rm M}_\odot\,{\rm pc}^{-2}}\right)^{-2}\right]^{1/2}\right\},
\end{aligned}
\tag{35}
$$

Since the second term in the square brackets of equation (35) dominates for the range of parameters we have explored (suitable for outer disks), an approximate form for equation (35) is:

$$
\begin{aligned}
P_{\rm tot,DE} &\approx f_{\rm diff}\sigma_{\rm z,diff}\Sigma(2G\rho_{\rm sd})^{1/2}\approx f_{\rm diff}^{1/2}\sigma_{\rm z}\Sigma(2G\rho_{\rm sd})^{1/2} \\[6pt]
&\approx 1.0\times10^4 k_{\rm B}\,{\rm cm}^{-3}\,{\rm K}\,f_{\rm diff}^{1/2}\left(\frac{\sigma_{\rm z}}{7\,{\rm km\,s}^{-1}}\right)\left(\frac{\Sigma}{10\,{\rm M}_\odot\,{\rm pc}^{-2}}\right)\left(\frac{\rho_{\rm sd}}{0.1\,{\rm M}_\odot\,{\rm pc}^{-3}}\right)^{1/2},
\end{aligned}
\tag{36}
$$

where we take $\sigma_{\rm z,diff}\approx f_{\rm diff}^{-1/2}\sigma_{\rm z}$ based on the fact that the velocity dispersions of very dense gas are smaller than those of the diffuse component. This is similar to the formula adopted by Blitz & Rosolowsky (2004, 2006), except that our expression includes the correction factor $f_{\rm diff}$ and allows for the dark matter contribution to $\rho_{\rm sd}$ (see also OML10). Although the factor $f_{\rm diff}$ in equation (36) is close to unity in outer disks, this correction would be quite important in inner-disk regions where gas is dominated by gravitationally-bound GMCs. For the current models, we note that $f_{\rm diff}\sigma_{\rm z,diff}/c_w = \alpha f_{\rm diff}\tilde{f}_w c_w/\sigma_{\rm z,diff} \sim f_{\rm diff}^{1/2}\sigma_{\rm z}/c_w \sim 1.0$ insensitive to model parameters since $\sigma_{\rm z}\sim\sigma_{\rm z,diff}\sim c_w\sim7-8\,{\rm km\,s}^{-1}$, $\alpha\sim4-5$, and $f_{\rm diff}\tilde{f}_w\sim0.2-0.3$ if $f_{\rm rad}=1$. Thus, if dynamical equilibrium is satisfied, we expect the midplane pressure to correlate well with $\Sigma\sqrt{\rho_{\rm sd}}$.

Figure 8(a) plots the midplane total pressure of the diffuse component $P_{\rm tot}\equiv P_{\rm th}+P_{\rm turb}$ measured from the simulations (as listed in Table 2) as a function of $\Sigma\sqrt{\rho_{\rm sd}}$ for all models. The errorbars denote the standard deviations of the pressure fluctuations. The dynamical-equilibrium prediction of equation (35) (or the approximation in equation 36) for $P_{\rm tot,DE}$ can be evaluated directly from the model inputs Σ and $\rho_{\rm sd}$ in Table 1 and simulation results for $f_{\rm diff}$, $v_{\rm z,diff}$, and $v_{\rm th,diff}$ listed in Table 3. In the lower panel of Figure 8(a),

we plot the relative difference between the measured P_{tot} and $P_{tot,DE}$ computed from equation (35). These values agree with each other within 13%. This close agreement verifies that effective hydrostatic equilibrium is indeed satisfied. In addition, this suggests that the midplane total pressure in a star-forming disk is set by environmental parameters such as the gas surface density, external gravity, the level of the turbulence, etc. Since the parameters appearing in equation (35) can be inferred relatively directly from observables for spatially-resolved face-on galaxies (modulo uncertainties in the stellar-disk scale height), the total midplane pressure in diffuse gas is an empirically-accessible quantity.

Adopting the dependence on "environmental" parameters Σ and ρ_{sd} following equation (36), the numerical results are well fitted by

$$P_{tot} = 9.9 \times 10^3 k_B \text{ cm}^{-3} \text{ K} \left(\frac{\Sigma}{10 \text{ M}_\odot \text{ pc}^{-2}} \right) \left(\frac{\rho_{sd}}{0.1 \text{ M}_\odot \text{ pc}^{-3}} \right)^{1/2}. \tag{37}$$

This fit is overplotted as a dotted line in the upper panel of Figure 8(a). Comparison of the fit to the numerical results (equation 37) with the analytic prediction (equation 36) shows that averaging over our model suite, $f_{diff}\sigma_{z,diff} \approx f_{diff}^{1/2}\sigma_z = 7.0 \text{ km s}^{-1}$.

For accounting purposes, we have arbitrarily adopted the choice $n_{GBC} = 50 \text{ cm}^{-3}$ as the minimum for the dense-gas GBC component. One might be concerned that this may significantly affect the value obtained for $P_{tot,DE}$. As seen in equation (36), however, $P_{tot,DE}$ for the present models depends on n_{GBC} just through $P_{tot,DE} \propto f_{diff}^{1/2}$ because $\sigma_z \sim 7 \text{ km s}^{-1}$ is nearly constant for all models. We have checked that if we instead chose $n_{GBC} = 100 \text{ cm}^{-3}$, f_{diff} increases by about 10%, resulting in only about 3% change in $P_{tot,DE}$. Thus, for the diffuse-dominated regime studied in the present work, $P_{tot,DE}$ does not depend sensitively on the specific choice for n_{GBC} as long as it is large enough. In the regime where gravitationally-bound gas is more important, or where self-gravity is comparable to the external gravity, the more exact expression in equation (1) (or equation 35) should be used for $P_{tot,DE}$.

While an empirical measure of total midplane pressure can be obtained from spatially-resolved observations of Σ, ρ_{sd}, and $\sigma_{z,diff}$, pressure-sensitive lines can be used to obtain empirical estimates of P_{th} even from unresolved observations. It is thus useful to consider how P_{th} relates to environmental properties in our models. Figure 8(b) plots the midplane thermal pressure of the diffuse component P_{th} (as listed in Table 2) as a function of $\Sigma\sqrt{\rho_{sd}}$ for all models except Series R. The lower panel shows the relative difference between P_{th} and $P_{th,DE} = P_{tot,DE}/\alpha$ as defined in equation (2), or multiplying equation (35) by $1/\alpha$. (Note that this differs slightly from the lower panel of Figure 8(a) because our measured α is based on volume-averaged rather than midplane pressures.) The errorbars denote the standard deviations of the pressure fluctuations. The dynamical-equilibrium prediction $P_{th,DE}$ agrees with the measured P_{th} at the midplane within 17%, excluding Series R. The dotted line in the upper panel of Figure 8(b) gives our best fit

$$P_{th} = 2.2 \times 10^3 k_B \text{ cm}^{-3} \text{ K} \left(\frac{\Sigma}{10 \text{ M}_\odot \text{ pc}^{-2}} \right) \left(\frac{\rho_{sd}}{0.1 \text{ M}_\odot \text{ pc}^{-3}} \right)^{1/2}. \tag{38}$$

Multiplying equation (36) by $1/\alpha$, the thermal pressure in outer-disk regions is approximately given by $P_{th,DE} \approx (f_{diff}/\alpha)\sigma_{z,diff}\Sigma(2G\rho_{sd})^{1/2}$. Note that the connection between thermal pressure and the parameters

Σ and ρ_{sd} expressed by equation (38) results from vertical force balance and the fact that α and $f_{diff}\sigma_{z,diff} \approx f_{diff}^{1/2}\sigma_z$ are nearly constant.

As seen in Section 4.2, since the amount of energy injected into the thermal component depends on f_{rad}, P_{th} is proportional to f_{rad} for Series R, resulting in significant changes of P_{th} for the same Σ and ρ_{sd} (see Table 2). The relation $P_{th} \sim P_{th,DE}$ still approximately holds provided that the inverse variation of α with f_{rad} is included for varying f_{rad} (see equation 46). Although σ_z and f_{diff} are insensitive to f_{rad}, the large variation of α with f_{rad} implies that the results for Series R significantly depart from equation (38). This is why Series R is omitted from Figure 8(b).

It is also possible to estimate the midplane density and the scale height. If dynamical equilibrium holds, the mean midplane mass density is given by $\rho_{0,DE} = P_{tot,DE}/\sigma_{z,diff}^2 = P_{th,DE}/v_{th,diff}^2$, or hydrogen number density $n_{0,DE} = \rho_{0,DE}/(1.4m_p)$ by

$$
\begin{aligned}
n_{0,DE} = \ &0.20\,\mathrm{cm}^{-3} f_{diff} \left(\frac{\sigma_{z,diff}}{7\,\mathrm{km\,s^{-1}}}\right)^{-2} \left(\frac{\Sigma}{10\,M_\odot\,\mathrm{pc}^{-2}}\right)^2 \times \\
&\left\{ (2-f_{diff}) + \left[(2-f_{diff})^2 + 37\left(\frac{\sigma_{z,diff}}{7\,\mathrm{km\,s^{-1}}}\right)^2 \left(\frac{\rho_{sd}}{0.1\,M_\odot\,\mathrm{pc}^{-3}}\right)\left(\frac{\Sigma}{10\,M_\odot\,\mathrm{pc}^{-2}}\right)^{-2} \right]^{1/2} \right\}.
\end{aligned}
\tag{39}
$$

For a Gaussian distribution, the scale height in vertical dynamical equilibrium is

$$
\begin{aligned}
H_{diff,DE} = \ &\frac{f_{diff}\Sigma}{(2\pi)^{1/2}\rho_{0,DE}} \\
= \ &580\,\mathrm{pc}\left(\frac{\sigma_{z,diff}}{7\,\mathrm{km\,s^{-1}}}\right)^2 \left(\frac{\Sigma}{10\,M_\odot\,\mathrm{pc}^{-2}}\right)^{-1} \times \\
&\left\{ (2-f_{diff}) + \left[(2-f_{diff})^2 + 37\left(\frac{\sigma_{z,diff}}{7\,\mathrm{km\,s^{-1}}}\right)^2 \left(\frac{\rho_{sd}}{0.1\,M_\odot\,\mathrm{pc}^{-3}}\right)\left(\frac{\Sigma}{10\,M_\odot\,\mathrm{pc}^{-2}}\right)^{-2} \right]^{1/2} \right\}^{-1}.
\end{aligned}
\tag{40}
$$

Figure 9 plots the measured values of (a) the midplane number density n_0 and (b) the scale height of the diffuse gas H_{diff} versus the corresponding dynamical-equilibrium estimate given in equation (39) and (40), respectively. Our best fits for imposed unity slopes give $n_0/n_{0,DE} = 1.4$ and $H_{diff}/H_{diff,DE} = 0.87$. These differences owe to small differences between the mass-weighted thermal velocity dispersion $v_{th,diff}$ and the slightly-lower midplane value $v_{th,mid}$, as discussed in Section 4.2.

5.2. Thermal Equilibrium and Turbulent Balance

As described in Section 2, OML10 hypothesized that the gas disk evolves to a state in which both cold and warm phases can coexist at the midplane, at the same thermal pressure, with heating balanced by cooling. For given heating rate, a range of pressures between P_{min} and P_{max} permits both a cold and warm phase in thermal equilibrium. For definiteness, OML10 assumed that the midplane thermal pressure P_{th} in the diffuse medium is comparable to the geometric-mean pressure $P_{two} = (P_{min}P_{max})^{1/2}$.

In our numerical models, the heating rate evolves with the SFR according to equation (24). Assuming the $J_{\mathrm{FUV,meta}}$ contribution is negligible, the geometric-mean pressure is given by equation (25), corresponding to $P_{\mathrm{two}}/k_B = 3.1 \times 10^3$ cm^{-3} K$(f_{\mathrm{rad}}\Sigma_{\mathrm{SFR}}/\Sigma_{\mathrm{SFR},0})$, where the coefficient is slightly different from that in equation (3) since the adopted cooling function in our simulations is slightly different from that in Wolfire et al. (2003). For each model, the mean value of Σ_{SFR} measured from the simulation sets the mean of P_{two}; the mean midplane thermal pressure is also measured (see Section 5.1 and Table 2). Using these measurements, Figure 10 plots $P_{\mathrm{th}}/P_{\mathrm{two}}$ as a function of Σ_{SFR} for all models. The dotted line is our best fit

$$\frac{P_{\mathrm{th}}}{P_{\mathrm{two}}} = 0.79 \left(\frac{\Sigma_{\mathrm{SFR}}}{10^{-3} \text{ M}_\odot \text{ kpc}^{-2} \text{ yr}^{-1}} \right)^{-0.09}. \tag{41}$$

The measured thermal pressure of the diffuse gas is thus smaller than the geometric-mean pressure, but only slightly: P_{th} agrees with P_{two} within $\sim 40\%$ for all models, while P_{th} varies over more than two orders of magnitude for our whole suite of models (see Table 2). This proves that the assumption $P_{\mathrm{th}} \approx P_{\mathrm{two}}$ of the OML10 theory is a reasonable first approximation.

Using the numerical result given in equation (41), we are now in a position to evaluate the thermal yield from feedback η_{th} defined in equation (11). We find

$$\eta_{\mathrm{th}} = 0.99 f_{\mathrm{rad}} \left(\frac{\Sigma_{\mathrm{SFR}}}{10^{-3} \text{ M}_\odot \text{ kpc}^{-2} \text{ yr}^{-1}} \right)^{-0.09}. \tag{42}$$

Our numerical calibration of η_{th} gives a value $\sim 30\%$ lower for the Solar neighborhood than the value $1.2 f_{\mathrm{rad}}$ adopted in OML10, and includes a weak decrease of η_{th} with increasing Σ_{SFR}.

The tendency for η_{th} to decrease with increasing Σ_{SFR} can be understood as follows. Models with higher Σ and Σ_{SFR} have a larger diffuse-gas density, and hence shorter cooling times, compared to models with lower Σ and Σ_{SFR}. In the n–P plane, a shorter cooling time implies that P_{th} will more quickly drop towards P_{min}, such that $P_{\mathrm{th}}/P_{\mathrm{two}}$ will be slightly lower for higher-Σ, higher-Σ_{SFR} models. Models with lower Σ have longer cooling times, such that P_{th} does not drop as quickly after heating events, and remains closer to P_{two}.

Under the assumption that the dynamics of the gas disk has reached a statistical steady state (as Figure 5 indicates), the rates of turbulent driving and dissipation must balance each other. For mean momentum p_* and mass m_* per supernova, the rate of injection of vertical momentum per unit area per unit time to each side of the disk is $P_{\mathrm{driv}} \equiv 0.25(p_*/m_*)\Sigma_{\mathrm{SFR}}$, assuming spherical blasts at the midplane (OS11). If the injected vertical momentum is preserved until the gas falls back to the midplane, the vertical momentum flux across the disk P_{turb} would be equal to $2P_{\mathrm{driv}}$. If, however, the injected vertical momentum is dissipated within a vertical crossing time, then $P_{\mathrm{turb}} = P_{\mathrm{driv}}$. Finally, if the space-time distribution of star formation sites is such that expanding shells collide with each other in the vertical direction, then partial cancellation of injected momentum would yield $P_{\mathrm{turb}} < P_{\mathrm{driv}}$.

OS11 parameterized the uncertainties in dissipation and driving by introducing a factor $f_p \equiv P_{\mathrm{turb}}/P_{\mathrm{driv}}$. Here, we use results of our numerical simulations to directly compare the measured turbulent pressure with the vertical momentum injected by supernovae in our models. We characterize the return on mechanical

feedback from star formation using the turbulent yield parameter η_{turb} defined in equation (12). The parameter f_p is related to η_{turb} by $\eta_{\text{turb}} \equiv 3.6 f_p [(p_*/m_*)/3000 \text{ km s}^{-1}]$.

Figure 11 plots our measurement of the ratio $P_{\text{turb}}/P_{\text{driv}}$ for all models, as a function of Σ_{SFR}. The dotted line shows our best fit omitting the R series,

$$\frac{P_{\text{turb}}}{P_{\text{driv}}} = 0.97 \left(\frac{\Sigma_{\text{SFR}}}{10^{-3} \text{ M}_\odot \text{ kpc}^{-2} \text{ yr}^{-1}} \right)^{-0.17}. \tag{43}$$

Our numerical calibration of the mechanical feedback yield is therefore

$$\eta_{\text{turb}} = 3.5 \left(\frac{\Sigma_{\text{SFR}}}{10^{-3} \text{ M}_\odot \text{ kpc}^{-2} \text{ yr}^{-1}} \right)^{-0.17}, \tag{44}$$

where we use $p_*/m_* = 3000 \text{ km s}^{-1}$ for all models. The numerical result in equation (43) shows that $f_p \approx 1$ provides a good overall estimate; this is also consistent with the results of simulations presented in OS11 (for the molecule-dominated starburst regime). The numerical result that f_p (and η_{turb}) decrease weakly with increasing Σ_{SFR} suggests that vertical collisions of shells become more important at higher star formation rates, as would be expected. On the other hand, disks with lower Σ_{SFR} suffer somewhat less momentum dissipation because star formation sites are more isolated (in space and time), and shells expand into a more rarefied medium.

As discussed in OS11, the result $P_{\text{turb}} \sim P_{\text{driv}}$ is equivalent to having the dissipation time of turbulence comparable to the flow crossing time over the largest energy-containing scale (Stone et al. 1998; Mac Low et al. 1998), which here is the vertical disk thickness $H_{\text{diff}} \sim H_{\text{diff,DE}}$. Feedback provides an input momentum per unit time per unit area of $\sim P_{\text{driv}} \sim \Sigma_{\text{SFR}} p_*/m_*$. For a dissipation time $\sim H_{\text{diff}}/v_{\text{z,diff}}$, the dissipation rate of vertical momentum in the diffuse ISM, per unit time per unit area is $\sim \Sigma v_{\text{z,diff}}^2/H_{\text{diff}} \sim \rho v_{\text{z,diff}}^2 \sim P_{\text{turb}}$. Thus, driving is balanced by dissipation on a crossing time provided $P_{\text{turb}} \sim P_{\text{driv}}$, as in equation (43).

Combining equations (11) and (12), we have

$$\frac{P_{\text{tot}}/k_{\text{B}}}{10^3 \text{ cm}^{-3} \text{ K}} \equiv \eta \frac{\Sigma_{\text{SFR}}}{10^{-3} \text{ M}_\odot \text{ kpc}^{-2} \text{ yr}^{-1}}, \tag{45}$$

where $\eta \equiv \eta_{\text{th}} + \eta_{\text{turb}}$ is the combined yield of thermal and mechanical feedback, with the respective contributions given in equations (42) and (44) from our numerical results. Other sources of vertical support that are associated with star formation (e.g. radiation pressure, cosmic rays, and magnetic fields driven by turbulence) would contribute additional terms to η. Since η_{th} and η_{turb} decrease weakly with Σ_{SFR}, the increase of P_{tot} with Σ_{SFR} is slightly sublinear.

Using equations (42) and (44), we obtain an expression for the ratio between total and thermal pressure in the diffuse gas:

$$\begin{aligned} \alpha & = 1 + \frac{\eta_{\text{turb}}}{\eta_{\text{th}}} \\ & = 1 + 3.5 f_{\text{rad}}^{-1} \left(\frac{\Sigma_{\text{SFR}}}{10^{-3} \text{ M}_\odot \text{ kpc}^{-2} \text{ yr}^{-1}} \right)^{-0.08}. \end{aligned} \tag{46}$$

This explains the very weak decreasing trend of α with Σ_{SFR} for $f_{\mathrm{rad}} = 1$ (see Fig. 7a). In addition, this implies the value $\alpha \approx 5$ adopted by OML10 (based on empirical evidence) is in good agreement with the results of numerical simulations (for $f_{\mathrm{rad}} \sim 1$). Similarly, since $\tilde{f}_w = v_{\mathrm{th,diff}}^2/c_w^2 = \sigma_{\mathrm{z,diff}}^2/(c_w^2\alpha)$, $\tilde{f}_w \sim [1 + 3.5f_{\mathrm{rad}}^{-1}(\Sigma_{\mathrm{SFR}}/10^{-3}\,\mathrm{M}_\odot\,\mathrm{kpc}^{-2}\,\mathrm{yr}^{-1})^{-0.08}]^{-1}(\sigma_{\mathrm{z,diff}}/c_w)^2$, where $\sigma_{\mathrm{z,diff}}/c_w = 1.1(\Sigma_{\mathrm{SFR}}/10^{-3}\,\mathrm{M}_\odot\,\mathrm{kpc}^{-2}\,\mathrm{yr}^{-1})^{0.04}$ for all models (see Fig. 6b). This form is consistent with the trend for $\tilde{f}_w$ to increase slightly with increasing Σ_{SFR}, and to increase significantly with increasing f_{rad} (see Table 3).

Finally, we note that although turbulent energy dominates over thermal energy in equilibrium (unless f_{rad} is large), the radiative heating *rate* exceeds the rate of heating from dissipation of turbulent energy, except in far outer disks. The energy input rate ratio is $\eta_{\mathrm{th}}/\eta_{\mathrm{turb}}$ times the ratio of the turbulent dissipation time ($\sim H_{\mathrm{diff}}/v_{\mathrm{z,diff}}$; see Section 6) to the cooling time (assuming thermal equilibrium). In the Solar neighborhood, the cooling time is ~ 1 Myr, whereas the turbulent dissipation time is ~ 20 Myr, implying a rate ratio ~ 5. Moving outward in the disk, the radiative-to-turbulent heating rate ratio decreases $\propto nH_{\mathrm{diff}}/v_{\mathrm{z,diff}}$, which is $\propto \Sigma$ for $v_{\mathrm{z,diff}} \sim constant$.

6. Star Formation Laws

In this section, we compare the SFRs obtained in our numerical simulations to SFR formulae that are widely used in the literature, both as fitting functions for empirical studies, and as prescriptions for star formation in numerical models of galaxy formation/evolution. We also introduce a new formula that relates Σ_{SFR} to the total pressure in the diffuse ISM. This relation follows the general form expected when thermal and dynamical equilibrium are both satisfied, and when both thermal and turbulent pressure are controlled by feedback from star formation.

We begin with the orbital time prescription, expressed as $\Sigma_{\mathrm{SFR}} \propto \Sigma\Omega$ (Kennicutt 1998). A relationship of this kind is expected if the star formation timescale is proportional to the orbital time, which would be true if star formation is governed by large-scale gravitational instabilities and the Toomre Q parameter is near its critical value (e.g. Quirk 1972; Wyse & Silk 1989; Silk 1997; Elmegreen 1997; Kim & Ostriker 2001, 2007; McKee & Ostriker 2007). Figure 12 plots the mean values of Σ_{SFR} from our numerical models as a function of $\Sigma\Omega$. The dotted line is the our best fit $\Sigma_{\mathrm{SFR}} = 0.008\Sigma\Omega$ for an imposed unity slope, while the dashed line denotes the empirical relation obtained by Kennicutt (1998), $\Sigma_{\mathrm{SFR}} = 0.017\Sigma\Omega$. The RMS fractional deviation of the measurements compared to the fit is 43%. In our simulations, the sites of star formation are mainly small-scale dense clouds formed by local thermal and gravitational instabilities, rather than very massive clouds formed by large-scale instabilities. Thus, orbital and epicyclic motions do not directly control star formation in our models. Rather, the similarity between the behavior of Σ_{SFR} and $\Sigma\Omega$ in Figure 12 reflects the correlation of input parameters chosen for our simulations: we set $\Omega \propto \Sigma$ for all models, and since the specific star formation rate increases with Σ, it also increases with Ω.

We next consider Σ_{SFR} as a function of Σ, as shown in Figure 13(a). Also plotted as filled and empty contours are the recent pixel-by-pixel measurements of Bigiel et al. (2008, 2010) for Σ_{SFR} and Σ in the regions inside and outside the optical radius, respectively, of nearby spiral and dwarf galaxies.

Consistent with the observational results for $\Sigma \lesssim 10$ M$_\odot$ pc^{-2}, Figure 13(a) shows that there can be significant variation in Σ_{SFR} at a given value of Σ. A single power-law fit to the numerical results gives $\Sigma_{SFR} = 2.2 \times 10^{-3}$ M$_\odot$ kpc^{-2} yr^{-1}($\Sigma/10$ M$_\odot$ pc^{-2})$^{1.6}$ (not shown in Figure 13a), with 33% RMS fractional deviation. Although the power law we find is similar to empirical results, our simulations indicate that a single power-law Kennicutt-Schmidt relation $\Sigma \propto \Sigma^{1+p}$ is not a good fit in outer-galaxy regions where $\Sigma \lesssim 10$ M$_\odot$ pc^{-2} and diffuse atomic gas dominates. Close inspection of Figure 13(a) shows that individually, the QA and QB series each follows a relation close to $\Sigma_{SFR} \propto \Sigma^2$, but these relations are vertically offset from each other. The reason the QA series has lower SFR than the QB series is that the latter has four times larger ρ_{sd} at a given value of Σ, and the reason both series approximately follow $\Sigma_{SFR} \propto \Sigma^2$ is that we have set $\rho_{sd} \propto \Sigma^2$ in both series, as we shall discuss below.

We remark that the current suite of models is not intended to match the full parameter range of observed galaxies, but instead to explore the fundamental physical dependence of star formation on environmental conditions using carefully controlled numerical models. Nevertheless, Series QA, which includes Solar neighborhood conditions and extends to higher and lower Σ assuming constant Q and s_0, follows the observed distribution of Σ_{SFR} vs. Σ quite well. At very low gas surface density $\Sigma = 2.5$ M$_\odot$ pc^{-2}, the results from our models have higher Σ_{SFR} than much of the observed distribution for far outer disks. This is largely because we chose low input values of s_0 to show the effects of stellar gravity clearly in our controlled series of models (lower s_0 corresponds to higher ρ_{sd} for a given Σ – see equation 28). Realistic values of s_0 in far outer disks are likely to be higher (see Section 3.3). Higher s_0 would reduce the vertical gravity and hence reduce Σ_{SFR} (following the secular trend of decreasing Σ_{SFR} with increasing $s_0 = 0.02$ to 0.07 to 0.28 from Series S to QB to QA at $\Sigma = 2.5$ M$_\odot$ pc^{-2}). In addition, Series QA, QB, and S fix $f_{rad} = 1$, whereas f_{rad} is likely to increase in far outer disks because of lower shielding where the dust abundance and Σ are lower (see Section 3.2.2). The models of Series R show that Σ_{SFR} systematically decreases with increasing f_{rad} for fixed Σ and ρ_{sd}. Thus, the difference between the present model results and observations at low Σ is simply due to differences between model inputs and ambient conditions of gravity and shielding in outer galaxies. This emphasizes once again that Σ alone does not determine Σ_{SFR}.

For typical parameters in outer disks, the weight associated with the external (star+dark matter) gravity term $\propto \rho_{sd}^{1/2}$ exceeds the weight associated with gaseous self-gravity in equation (7) (or 8) for the dynamical-equilibrium diffuse-ISM pressure $P_{tot,DE}$, which is equal to the diffuse-ISM weight. Since the external-gravity dominates, we have $P_{tot,DE} \propto \Sigma \rho_{sd}^{1/2} \sigma_z$ as in equation (36) (see also Figure 8a), and $P_{tot,DE} \propto \eta \Sigma_{SFR}$ (equation 45) so that $\Sigma_{SFR} \propto \Sigma \rho_{sd}^{1/2} \sigma_z / \eta$ for $\eta = \eta_{th} + \eta_{turb}$. Since σ_z and the yield parameters η_{th}, η_{turb} are all close to constant (see Fig. 6 and equations 42 and 44), we expect $\Sigma_{SFR} \propto \Sigma \rho_{sd}^{1/2}$.

Figure 13(b) plots results from the simulations for Σ_{SFR} vs. $\Sigma \rho_{sd}^{1/2}$, showing a much tighter relationship than Σ_{SFR} vs. Σ in Figure 13(a). Comparing measured values to the fit in equation (47) below, the RMS fractional deviation is 24%. This is consistent with recent empirical findings that star formation is correlated with the stellar, not just the gaseous, content of galactic disks (see Section 1).

In both panels of Figure 13, we overplot the simultaneous solutions of equations (5), (11), and (35), adopting $\sigma_z = 7$ km s^{-1}, $\alpha = 5$, and $t_{SF,GBC} = 1.3$ Gyr, along with the numerical fit for η_{th} (equation 42 with

$f_{\rm rad} = 1$). If we instead adopt $\eta_{\rm th} = 1$, the results are quite similar since $\eta_{\rm th}$ is nearly constant. The black dot-dashed curve takes $s_0 = 0.28$ as in Series QA, the red dashed curve takes $s_0 = 0.07$ as in Series QB, and the blue dotted ($s_0 = 0.02$) and green long-dashed ($s_0 = 1.1$) curves bracket the overall range of s_0 for our model suite (see Table 1). The predicted curve for $s_0 = 0.28$ (as in Series QA) follows the observations quite well within the optical radius. As discussed above, larger values of s_0 and $f_{\rm rad}$ are likely present in far outer disks, which would produce a steeper $\Sigma_{\rm SFR}$ vs. Σ relation moving to very low Σ (outside typical optical radii). The agreement between numerical models and the simultaneous solution of equations (5), (11), and (35) confirms the analytic thermal/dynamical equilibrium theory for star formation developed in OML10. In that work, comparison to individual galaxies shows excellent agreement when both Σ and $\rho_{\rm sd}$ in the theory are set from the observations.

In panel Figure 13(b), the black solid line denotes the power-law solution obtained by combining equations (11), (38), and (42) (with $f_{\rm rad} = 1$) to obtain a prediction for $\Sigma_{\rm SFR}$:

$$\Sigma_{\rm SFR} = 2.4 \times 10^{-3} \; {\rm M_\odot \; kpc^{-2} \; yr^{-1}} \left(\frac{\Sigma}{10 \; {\rm M_\odot \; pc^{-2}}} \right)^{1.1} \left(\frac{\rho_{\rm sd}}{0.1 \; {\rm M_\odot \; pc^{-3}}} \right)^{0.55}. \tag{47}$$

We note that for outer disk regions, the focus of the present models, the approximation $f_{\rm diff} \approx 1$ is satisfied, such that the single equation (36) takes the place of the simultaneous solution of equations (5) and (35). That is, the prediction for outer-disk star formation is independent of $t_{\rm SF,GBC}$. If, rather than using the numerical fit (42) for $\eta_{\rm th}$, we had instead simply adopted a constant value of $\eta_{\rm th} \approx 1$, then we would obtain a very similar form to equation (47), except the exponent of $\rho_{\rm sd}$ would be 0.5, the exponent of Σ would be 1, and the coefficient in front would be $2.2 \times 10^{-3} \eta_{\rm th}^{-1} \; {\rm M_\odot \; kpc^{-2} \; yr^{-1}}$. Small differences between the numerical results and the analytic prediction for outer disk regions are due to the fact that some of the idealizations of equation (36) are not fully satisfied in the numerical models. For example, the S series models at $\Sigma = 15$ and $20 \; {\rm M_\odot \; pc^{-2}}$ have non-negligible gravity from the gas, which increases $P_{\rm th,DE}$ above the estimate in equation (36), and results in $\Sigma_{\rm SFR}$ exceeding the estimate of (47), which neglects the vertical gas gravity. Also, we note that the R series, because it has $f_{\rm rad} \neq 1$, is not expected to agree with equation (47). In fact, members of the R series lie both above and below the prediction, consistent with expectations.

A prescription for star formation commonly used in numerical simulations of galaxy formation and evolution within a cosmological context is to make the star formation timescale proportional to the self-gravitation or free-fall time of the gas, $\propto \rho^{-1/2}$. In the context of disks, it is natural to adopt the mean midplane density ρ_0 as a reference value, so that the SFR surface density would be given by

$$\Sigma_{\rm SFR} \equiv \epsilon_{\rm ff}(\rho_0) \frac{\Sigma}{t_{\rm ff,0}}, \tag{48}$$

where $t_{\rm ff,0} = [3\pi/(32G\rho_0)]^{1/2}$ is the free-fall time at the midplane and $\epsilon_{\rm ff}(\rho_0)$ is a star formation efficiency per free-fall time at the mean midplane density. Figure 14(a) plots $\Sigma_{\rm SFR}$ from the numerical simulations as a function of $\Sigma/t_{\rm ff,0}$. The dotted line shows our best fit $\Sigma_{\rm SFR} = 0.008(\Sigma/t_{\rm ff,0})$ for an imposed unity slope. Note that $\epsilon_{\rm ff}(\rho_0) = 0.008$ is similar to (but slightly smaller than) the value $\epsilon_{\rm ff}(\rho_{\rm cr}) = 0.01$ imposed at high density ($n_{\rm cr} \sim 500 \; {\rm cm^{-3}}$) for star formation to occur in the numerical models. The free-fall time prescription gives a tighter relation than $\Sigma_{\rm SFR}$ vs. $\Sigma\Omega$ or $\Sigma_{\rm SFR}$ vs. Σ, but there is still scatter.

Although the free-fall time is commonly adopted as the controlling dynamical timescale, in many circumstances self-gravity is less important in confining and condensing gas than the gravity of the stars and dark matter. For a given total velocity dispersion $\sigma_{z,\mathrm{diff}}$, the vertical dynamical time is related to the disk thickness by $t_{\mathrm{dyn}} \equiv H_{\mathrm{diff}}/\sigma_{z,\mathrm{diff}}$. Since $H_{\mathrm{diff}} \equiv \Sigma_{\mathrm{diff}}/(\sqrt{2\pi}\rho_0) = \sigma_{z,\mathrm{diff}}/(4\pi G\rho_{\mathrm{sd}})^{1/2}$ if external gravity dominates, or $H_{\mathrm{diff}} = \sigma_{z,\mathrm{diff}}/(\pi^2 G\rho_0)^{1/2}$ if gas self-gravity dominates, $t_{\mathrm{dyn}} \sim 0.3/(G\rho_{\mathrm{mid}})^{1/2}$ with $\rho_{\mathrm{mid}} = \rho_0 + \rho_{\mathrm{sd}}$ includes both limits. If self-gravity dominates, $t_{\mathrm{ff},0} = 1.7 t_{\mathrm{dyn}}$, but if $\rho_0 \ll \rho_{\mathrm{sd}}$, $t_{\mathrm{dyn}} \ll t_{\mathrm{ff},0}$, and the "external" gravity sets t_{dyn} and H_{diff}.

For a disk with significant turbulent contribution to the total velocity dispersion $\sigma_{z,\mathrm{diff}}$, t_{dyn} is comparable to the vertical crossing time $t_{\mathrm{ver}} \equiv H_{\mathrm{diff}}/v_{z,\mathrm{diff}}$. The vertical crossing time is the timescale for turbulence to be dissipated, reducing the disk thickness and raising ρ_0. For a low filling-factor cloudy medium, small, cold, dense clouds can also "fall" to the midplane due to the combined vertical gravitational force of stars, dark matter, and gas. When they reach the midplane, these small, dense clouds collide dissipatively, collecting into high-mass clouds that are internally gravitationally unstable and make stars. The vertical crossing time t_{ver} is thus expected to control how rapidly the diffuse cold component collects into self-gravitating clouds and initiates star formation.

Figure 14(b) plots Σ_{SFR} from the numerical simulations as a function of Σ/t_{ver}. The dotted line indicates our best fit $\Sigma_{\mathrm{SFR}} = 0.0025(\Sigma/t_{\mathrm{ver}})$ for an imposed unity slope. The coefficient of this fit denotes the star formation efficiency per vertical dynamical time $\epsilon_{\mathrm{ver}} = 0.0025$. The measured SFR surface density is well described by the vertical dynamical time prescription, although there is still scatter (but slightly less than in Figure 14a). The RMS fractional deviations of measured Σ_{SFR} compared to the estimated Σ_{SFR} are 26% and 21% for the free-fall time and the vertical dynamical time prescriptions, respectively.

The good correlations shown in Figure 14 for both the $t_{\mathrm{ff},0}$ and t_{ver} prescriptions are presumably because both implicitly have similar scaling to $\Sigma_{\mathrm{SFR}} \propto \Sigma\sqrt{\rho_{\mathrm{sd}}}$ (shown in Figure 13b). Since $\rho_0 \sim \rho_{0,\mathrm{DE}} \propto \Sigma/H_{\mathrm{diff}} \propto \Sigma\rho_{\mathrm{sd}}^{1/2}$ (when external gravity dominates), $\Sigma/t_{\mathrm{ff},0}$ is basically proportional to $\Sigma^{3/2}\rho_{\mathrm{sd}}^{1/4}$. For Series QA and QB, $\Sigma^{1/2}\rho_{\mathrm{sd}}^{1/4} \propto \rho_{\mathrm{sd}}^{1/2}$ because we take $\rho_{\mathrm{sd}} \propto \Sigma^2$ for these models. Thus, $\Sigma/t_{\mathrm{ff},0} \propto \Sigma\sqrt{\rho_{\mathrm{sd}}}$ for Series QA and QB. Although Series S and G have somewhat different input parameter dependence, the parameter coverage of these model series is not extensive enough to reveal a clear difference between $\Sigma_{\mathrm{SFR}} \propto \Sigma\sqrt{\rho_{\mathrm{sd}}}$ and $\Sigma_{\mathrm{SFR}} \propto \Sigma/t_{\mathrm{ff},0}$. For regions dominated by external gravity, we have $t_{\mathrm{ver}} \approx (4\pi G\rho_{\mathrm{sd}})^{-1/2}\sigma_{z,\mathrm{diff}}/v_{z,\mathrm{diff}}$, so that $\Sigma/t_{\mathrm{ver}} \propto \Sigma\rho_{\mathrm{sd}}^{1/2}$ since $\sigma_{z,\mathrm{diff}} \sim v_{z,\mathrm{diff}}$ for our models (and for the real ISM).

We note that the vertical dynamical time prescription for star formation is closely connected to the regulation of turbulent pressure by feedback from star formation, and to the relationship between input momentum and mean velocity dispersion in the disk (OS11). As shown in Section 5.2, a balance between turbulent momentum driving and dissipation is achieved in our models. If $\Sigma_{\mathrm{SFR}} = \epsilon_{\mathrm{ver}}\Sigma/t_{\mathrm{ver}}$, the momentum driving rate per unit mass becomes $2P_{\mathrm{driv}}/\Sigma = 0.5\epsilon_{\mathrm{ver}}p_*/(m_* t_{\mathrm{ver}})$. Equating this with the expected turbulence dissipation rate $\sim 0.5v_{z,\mathrm{diff}}^2/H_{\mathrm{diff}} = 0.5v_{z,\mathrm{diff}}/t_{\mathrm{ver}}$, we obtain $v_{z,\mathrm{diff}} \sim \epsilon_{\mathrm{ver}}p_*/m_*$. Using our adopted value $p_*/m_* = 3{,}000$ km s^{-1} and the efficiency $\epsilon_{\mathrm{ver}} = 0.0025$ measured from our numerical models, this yields $v_{z,\mathrm{diff}} = 7.5$ km s^{-1}, remarkably similar to the mean value $v_{z,\mathrm{diff}} = 6.8$ km s^{-1} obtained from our numerical simulations.

As argued in Section 2, energy and momentum feedback from star formation are often the dominant sources of heating and turbulence driving, in which case both P_{th} and P_{turb} (and therefore P_{tot}) in the diffuse ISM are predicted to vary approximately $\propto \Sigma_{SFR}$ (see equations 11 and 12). As we show in Section 5.2, our simulations indeed evidence near-linear relations. In Figure 15, we plot the measured Σ_{SFR} as a function of (a) the measured $(P_{th}/k_B)/f_{rad}$ and (c) the measured P_{tot}/k_B, for all of our numerical models. All quantities are time-averaged. Note that the thermal pressure is divided by f_{rad} to compensate for the effect of the varying assumed heating efficiency (Γ/Σ_{SFR}). The dotted lines in panels (a) and (c) are obtained from equations (11) and (45), respectively, with numerical calibrations (42) and (44) for the feedback yields η_{th} and η_{turb}. The dashed line in panel (c) plots our best fit omitting the R series:

$$\Sigma_{SFR} = 2.6 \times 10^{-3} \ M_\odot \ \mathrm{kpc}^{-2} \ \mathrm{yr}^{-1} \left(\frac{P_{tot}/k_B}{10^4 \ \mathrm{cm}^{-3} \ \mathrm{K}} \right)^{1.18}. \tag{49}$$

The power slightly steeper than unity reflects the weak decline of feedback yields η_{th} and η_{turb} with Σ_{SFR}, as discussed in Section 5.2 (cf. equation 45) . Comparing equation (49) with equation (13), we see that our numerical results yield $\eta = 3.9[P_{tot}/(10^4 k_B \ \mathrm{cm}^{-3} \ \mathrm{K})]^{-0.18}$ (for $f_{rad} = 1$), quite close to the estimate $\eta \sim 5$ obtained by combining the theory of OML10 and OS11 (see Section 2).

In addition to heating/cooling and turbulent driving/dissipation balance, vertical dynamical equilibrium is expected to apply, so that the total diffuse-gas pressure at the midplane is equal to the vertical weight $P_{tot} = P_{tot,DE}$. Thus, a hallmark of self-regulated star formation, when thermal, turbulent, and dynamical equilibrium are all satisfied, is that a relation close to $\Sigma_{SFR} \propto P_{tot,DE}$ is expected to apply (see equation 13). To the extent that $\alpha \sim const.$, we also expect $\Sigma_{SFR} \propto P_{th,DE}/f_{rad} = P_{tot,DE}/(\alpha f_{rad})$. In Figure 15 we plot the measured Σ_{SFR} from numerical simulations as a function of (b) $(P_{th,DE}/k_B)/f_{rad}$, and (d) $P_{tot,DE}/k_B$, for all models. The dynamical-equilibrium pressures are computed from input parameters Σ and ρ_{sd} using equation (35) and mean measured values of f_{diff}, $\sigma_{z,diff}$, and α for each model.[8] Dotted and dashed lines are as for Figures 15(a,c).

Figures 15(c,d) show that Σ_{SFR} is extremely well correlated with P_{tot} and $P_{tot,DE}$. The RMS fractional deviations of the numerical results from the relation given in equation (49) are only 14% and 16% for P_{tot} and $P_{tot,DE}$, respectively. The correlation is worse if the R series is included. This is because $\eta_{th} \propto f_{rad}$, so that higher f_{rad} reduces Σ_{SFR} compared to other models with the same midplane pressure.

Based on the results of our numerical simulations, we conclude that star formation rates should be most closely correlated with the total midplane pressure of the diffuse gas, as in equation (49).[9] The relation between diffuse-gas pressure and star formation rate has less scatter than the relation between Σ_{SFR} and the

---

[8]If we compute $P_{tot,DE}$ from equation (35) using constant values $f_{diff} = 0.78$ and $\sigma_{z,diff} = 7.7 \ \mathrm{km \ s}^{-1}$ (the mean values over the model suite), the best fit to Σ_{SFR} vs. $P_{tot,DE}$ analogous to equation (49) would have a coefficient 2.2×10^{-3} and a power 1.05.

[9]Although our current numerical models have only explored the diffuse-dominated case, we still expect thermal, turbulent, and vertical dynamical equilibrium to hold in the volume-filling diffuse gas even if it is not the dominant component of the ISM by mass (see OML10, OS11, and Section 2). In this case, equations (45) and (13) are still expected to hold with near-constant yield coefficients η, so that P_{tot} or $P_{tot,DE}$ would still vary nearly linearly with Σ_{SFR}. It is important to note, however, that in the GBC-dominated case, this is best interpreted as Σ_{SFR} setting f_{diff} (by equating [35] and [45] with $\Sigma_{SFR} \approx \Sigma/t_{SF,GBC}$) rather than the

gas surface density Σ alone, or the combination $\Sigma\Omega$. The relation between Σ_{SFR} and P_{tot} is also more general than $\Sigma_{\mathrm{SFR}} \propto \Sigma\sqrt{\rho_{\mathrm{sd}}}$ (which applies when external gravity exceeds gas self-gravity and $\sigma_{\mathrm{z,diff}} \sim const.$), or $\Sigma_{\mathrm{SFR}} \propto \Sigma/t_{\mathrm{ver}}$ (which applies for turbulence-dominated disks with $\epsilon_{\mathrm{ver}} \sim const.$). In regions dominated by diffuse gas, it is fundamentally the *weight of the ISM* that regulates star formation rates, since star formation rates must adjust until the pressure driven by feedback matches this weight. For outer disks that are diffuse-dominated ($f_{\mathrm{diff}} \sim 1$), the weight (or $P_{\mathrm{tot,DE}}$, given by equation 7 or by the approximation in equation 8) depends only on Σ, ρ_{sd}, and σ_{z}. As noted above, an increase in f_{rad} (which would be associated with low dust abundance) leads to a decrease in $\Sigma_{\mathrm{SFR}} \propto P_{\mathrm{tot,DE}}/\eta$, because $\eta_{\mathrm{th}} \propto f_{\mathrm{rad}}$.

7. Summary and Discussion

In this paper, we have used time-dependent numerical simulations to investigate the regulation of star formation, as well as the thermal and turbulent properties of the gas, in the regime where diffuse atomic gas dominates the multiphase ISM. For the Milky Way and similar galaxies, this corresponds to the outer disk – i.e. roughly the Solar circle and beyond. Physical effects included in our numerical models (see Section 3) include differential rotation, Coriolis forces, gaseous self-gravity, vertical gravity due to the stellar disk and dark matter halo, interstellar cooling and heating, thermal conduction, and feedback from recent star formation in the form of radiative and mechanical energy. Although this initial set of models involves a number of simplifications (e.g. we consider only a local box representing thin radial-vertical slices so that very large-scale gravitational instabilities are absent; we do not include galactic magnetic fields and spiral arms; we omit hot gas and treat feedback from SNe via localized momentum injection; we do not explicitly treat radiative transfer), it captures a very important aspect of real ISM disks that is missing in many numerical studies of galactic star formation. Namely, the vertical thickness of the disk, and therefore the mean gas density, is primarily controlled by (time-variable) turbulence. The turbulent vertical velocity dispersion depends on competition between driving by energy inputs from star formation, and dissipation through shocks and the mode-coupling turbulent cascade.

To explore the dependence of Σ_{SFR} on environmental parameters, we run models with varying total gas surface density Σ and midplane density ρ_{sd} of stars plus dark matter. The angular velocity Ω is set such the Toomre stability parameter $Q_{\mathrm{init}} = 2$ for a velocity dispersion of 7 km s^{-1}. Our models are highly dynamic, but each reaches a statistical steady state within a few tens of Myr. In this quasi-steady state, the star formation rate, disk scale height, mass fractions of various gas phases, turbulent velocity dispersion, and other physical properties fluctuate about well-defined mean values (Fig. 2). Low-amplitude quasi-periodic oscillations of the disk thickness are correlated with episodes of bound cloud formation (at maximum compression) and feedback-driven expansion. Small cold clouds repeatedly fall to the midplane and collect (due to self-gravity) into more massive clouds, which are then dispersed by feedback from star formation. We use the measured mean properties to test the theory of star formation and diffuse-ISM regulation developed

---

diffuse-ISM weight setting Σ_{SFR} (see OML10). If GBCs dominate the mass, Σ_{SFR} is controlled by the density (and pressure) within the bound clouds.

in OML10 and OS11, as outlined in Section 2.

The main results from our simulations are as follows:

1. We find that most of the gas is at pressures, densities, and temperatures close to thermal equilibrium (Fig. 4). The system evolves to a state in which both warm and cold stable phases are present, with mean midplane thermal pressure $P_{\rm th}$ within $\sim 40\%$ of the "two-phase" pressure $P_{\rm two} \equiv (P_{\rm min}P_{\rm max})^{1/2}$, decreasing weakly with increasing $\Sigma_{\rm SFR}$ (equation 41). This evolution involves continuous re-adjustment of the thermal equilibrium curve, as $P_{\rm two} \propto \Gamma \propto \Sigma_{\rm SFR}$. Since $\Sigma_{\rm SFR}$ varies by two orders of magnitude for our model suite, the thermal equilibrium curve shifts up and down by the same factor. The midplane thermal pressure increases from $P_{\rm th}/k_B \sim 100\,{\rm cm}^{-3}\,{\rm K}$ to $\sim 10^4\,{\rm cm}^{-3}\,{\rm K}$ going from low-Σ, low-$\rho_{\rm sd}$ to high-Σ, high-$\rho_{\rm sd}$ models (Fig. 8). This finding is consistent with the conclusion of Wolfire et al. (2003) that H I should be found in two phases out to large distances in the Milky Way (based on an assumed heating rate that declines outward), as well as observations indicating both phases are indeed present out to $\sim 20-25$ kpc (Dickey et al. 2009). Other nearby galaxies also show evidence for both warm and cold atomic gas (Braun 1997; Dickey et al. 2000; Young et al. 2003). The analytic model of OML10 adopted the assumption that the midplane thermal pressure is equal to $P_{\rm two}$; our numerical results show that this is indeed a good first estimate. The result $P_{\rm th} \sim P_{\rm two}$ implies that radiative heating approximately balances cooling. From the point of view of thermal energy replenishment, this means that star formation is highly efficient.

2. By comparing the prediction of dynamical-equilibrium pressure with the measured time-averaged midplane pressure in our numerical simulations, we find that vertical dynamical equilibrium is satisfied within 13% for the total pressure (lower panel of Fig. 8a). For the present models, the total weight of the diffuse ISM ($P_{\rm tot,DE}$, given in equation 1 or 35) is matched by a combination of thermal and turbulent pressure. In outer disks, where diffuse gas dominates the total surface density $\Sigma_{\rm diff} \approx \Sigma$, simplified expressions for the total midplane pressure in equilibrium are given by equations (7) and (8). In many outer-disk regions (including the Solar neighborhood), the vertical gravity from the stars exceeds that from the gas, such that in equilibrium $P_{\rm tot} \propto \Sigma\sqrt{\rho_{\rm sd}}$ if the vertical velocity dispersion is constant. The results from our simulations fit this form well (equation 37), with a similar result for midplane thermal pressure (equation 38). The numerical results that $P_{\rm th} \approx P_{\rm th,DE}$ and $P_{\rm tot} \approx P_{\rm tot,DE}$ demonstrate the validity of the vertical dynamical equilibrium assumption in the theory of OML10, and confirms prior findings from simulations by Koyama & Ostriker (2009b).

3. Based on our numerical measurements of the thermal and turbulent pressures, we find a ratio $P_{\rm tot}/P_{\rm th} = \alpha \approx 4-5$ for essentially all our models (Fig. 7a) when we fix $f_{\rm rad} \equiv (\Gamma/\Gamma_0)(\Sigma_{\rm SFR}/\Sigma_{\rm SFR,0})^{-1} = 1$ (see equation 24). This is consistent with the assumption of OML10 that α is relatively constant for galaxies with shielding properties (and hence $J_{\rm FUV}/\Sigma_{\rm SFR}$) similar to the local Milky Way. The near-constancy of α results from the fact that both thermal and turbulent pressure are driven by feedback (see below). When $f_{\rm rad}$ is varied (for Series R models), corresponding to varying dust shielding or FUV heating efficiency, α varies because $P_{\rm th} \propto f_{\rm rad}$ in thermal equilibrium. Higher $f_{\rm rad}$ (lower shielding) reduces α following equation (46); for large $f_{\rm rad}$, $P_{\rm th}$ can exceed $P_{\rm turb}$.

4. We find that the fraction of diffuse gas in the warm component $\tilde{f}_w \equiv v_{\rm th,diff}^2/c_w^2$ increases from

$\sim 20\%$ to $\sim 50\%$ from low- to high-$\Sigma_{\rm SFR}$, when we hold $f_{\rm rad} = 1$, corresponding to $\Gamma/\Sigma_{\rm SFR} = const$. The upper range, with half of the diffuse gas warm (for models similar to the Solar neighborhood), is comparable to findings of Heiles & Troland (2003) based on 21 cm emission and absorption observations. We find (for Series R) that the warm fraction steeply increases as $f_{\rm rad}$ increases (higher $\Gamma/\Sigma_{\rm SFR}$, corresponding to lower shielding by dust). This trend is consistent with the finding of Dickey et al. (2000) that the SMC, with a relative metallicity ~ 0.2, has a much higher warm-to-cold H I ratio than the Solar neighborhood. We note that in real galaxies, $f_{\rm rad}$ would be inversely correlated with Σ (see Section 3.2.2), which would increase the warm fraction at low Σ compared to the $f_{\rm rad} = 1$ models in Series QA, QB, and S presented here.

5. The time-averaged turbulent vertical velocity dispersions in all of our models are $v_{\rm z,diff} \approx 7$ km s^{-1}, with no systematic dependence on $\Sigma_{\rm SFR}$ (Fig. 6). Total vertical velocity dispersions $\sigma_{\rm z,diff}$ in the diffuse medium are larger by $\sim 1 - 2$ km s^{-1}. The turbulent amplitudes we find, and the lack of correlation of $\sigma_{\rm z,diff}$ with $\Sigma_{\rm SFR}$, are consistent with observations of H I velocity dispersions in the Milky Way and nearby face-on galaxies (Heiles & Troland 2003; Dickey et al. 1990; van Zee & Bryant 1999; Petric & Rupen 2007; Kalberla & Kerp 2009). As discussed in Section 6 (see also OS11), turbulent velocity dispersions $v_{\rm z,diff} \sim \epsilon_{\rm ver} p_*/m_*$ are expected if the star formation efficiency per vertical crossing time is $\epsilon_{\rm ver} \equiv t_{\rm ver}\Sigma_{\rm SFR}/\Sigma$ (for $t_{\rm ver} \equiv H_{\rm diff}/v_{\rm z,diff}$), and the momentum injection per stellar mass from feedback is p_*/m_*. Confirming this expectation, the turbulent amplitudes we find are consistent with the mean value $\epsilon_{\rm ver} = 0.0025$ measured from our numerical models, for the momentum feedback parameter $p_*/m_* = 3000$ km s^{-1} used in our simulations.

6. To assess the balance of turbulent driving and dissipation in our numerical models, we compare the measured turbulent pressure at the midplane $P_{\rm turb} \equiv \rho_0 v_{\rm z,diff}^2$ with the fiducial momentum injection rate per unit area $P_{\rm driv} \equiv 0.25(p_*/m_*)\Sigma_{\rm SFR}$ from star formation feedback. Fig. 11 shows that these are approximately equal, decreasing weakly with increasing $\Sigma_{\rm SFR}$ (equation 43). Since $P_{\rm turb}$ represents the characteristic vertical momentum per unit area in the diffuse ISM ($\Sigma_{\rm diff}v_{\rm z,diff}$) divided by $2H_{\rm diff}/v_{\rm z,diff}$, this implies the momentum dissipation timescale is comparable to the crossing time $t_{\rm ver} = H_{\rm diff}/v_{\rm z,diff}$, consistent with previous numerical results on turbulent driving and dissipation (e.g. Stone et al. 1998; Mac Low et al. 1998). Another way to think of this result is that the momentum injected in the diffuse ISM by star formation per unit time is comparable to the existing vertical momentum divided by the dynamical time. Thus, from the point of view of momentum replenishment, star formation is highly efficient.

7. We use our numerical models to calibrate the feedback yield parameters $\eta_{\rm th}$ and $\eta_{\rm turb}$, respectively equal to the ratio $P_{\rm th}/\Sigma_{\rm SFR}$ and $P_{\rm turb}/\Sigma_{\rm SFR}$ in suitable units (see equations 11 and 12). Both yield parameters decrease only very weakly with increasing $\Sigma_{\rm SFR}$ (see equations 42 and 44), with thermal yield also depending on the radiation penetration parameter as $\eta_{\rm th} \propto f_{\rm rad}$. This explains why $\alpha = P_{\rm tot}/P_{\rm th} = 1 + \eta_{\rm turb}/\eta_{\rm th}$ is nearly constant (for $f_{\rm rad} = 1$). The values $\eta_{\rm th} \sim 1 \times f_{\rm rad}$ and $\eta_{\rm turb} \sim 4$ obtained from our numerical models are consistent with the analytic predictions of OML10 and OS11, respectively.

8. We compare our numerical results for $\Sigma_{\rm SFR}$ to several commonly-used formulae, $\Sigma_{\rm SFR} \propto \Sigma\Omega$, $\Sigma_{\rm SFR} \propto \Sigma^{1+p}$, $\Sigma_{\rm SFR} = \epsilon_{\rm ff}(\rho_0)\Sigma/t_{\rm ff,0}$ (see Figs. 12, 13, 14). The first two relations are not well correlated with the numerical results. The third relation has improved correlation, but this is in part because $t_{\rm ff,0} \propto (G\rho_{\rm sd})^{-1/2}$ for most of our model suite, and $\Sigma_{\rm SFR}$ is well correlated with $\Sigma\rho_{\rm sd}^{1/2}$ (Fig. 13; see also equation 47). We also

compare to the relation $\Sigma_{\text{SFR}} = \epsilon_{\text{ver}} \Sigma / t_{\text{ver}}$ for $t_{\text{ver}} = H_{\text{diff}} / v_{z,\text{diff}}$ the vertical crossing time, which limits how rapidly cold clouds can collect at the midplane. The fitted efficiencies are $\epsilon_{\text{ff}}(\rho_0) = 0.008$ and $\epsilon_{\text{ver}} = 0.0025$, with a stronger correlation to the vertical crossing-time than free-fall-time prescription.

9. The best star formation correlation we find is with the total midplane pressure – either as measured in the simulations (P_{tot}), or as estimated from vertical dynamical equilibrium ($P_{\text{tot,DE}}$). Equation (49) fits Σ_{SFR} within 16% for all models (excluding Series R), as shown in Fig. 15. Series R shows that Σ_{SFR} drops if the shielding is reduced (higher f_{rad}). Our numerical result that Σ_{SFR} has a near-linear correlation with $P_{\text{tot,DE}}$ is consistent with the analytic models of OML10 and OS11 for star formation in diffuse-gas dominated regions – either outer disks or starbursts. The near-linear relation between Σ_{SFR} and $P_{\text{tot,DE}}$ is also consistent with a similar empirical result found by Leroy et al. (2008), and with the previous empirical findings that molecular gas (the immediate precursor of star formation) increases nearly linearly with the ISM pressure (Wong & Blitz 2002; Blitz & Rosolowsky 2004, 2006). A relationship of the form $\Sigma_{\text{SFR}} \sim P_{\text{tot,DE}}/\eta$ (see equation 45) implies that star formation responds to demand: the star formation rate increases until the midplane pressure (controlled by thermal and turbulent feedback) balances the vertical weight of the diffuse ISM.

That energy input from massive stars determines the midplane pressure and thus self-regulates the star formation rate suggests it is crucial to include stellar feedback, when simulating galactic star formation numerically. Indeed, work by Hopkins et al. (2011) contemporary with the present study used SPH simulations to show that Σ_{SFR} is consistent with the observed Kennicutt-Schmidt relations only when feedback is included (see also Dobbs et al. 2011). Without feedback, dense clouds collapse in a runaway fashion, increasing the star formation rate by $\sim 1-2$ orders of magnitude. Using grid-based simulations of Milky-Way-type galaxies, Tasker (2011) similarly found that star formation rates are at least an order of magnitude higher than observations if feedback is not included to drive turbulence and unbind dense clouds that form. Including feedback is known to strongly affect the star formation history in long-term simulations of galaxies (e.g. Governato et al. 2007).

Stellar feedback also appears essential for driving and maintaining turbulence in the direction perpendicular to the disk plane over many galactic orbits. Other proposed mechanisms for generating ISM turbulence include large-scale gravitational instabilities (e.g., Wada et al. 2002; Kim et al. 2003; Kim & Ostriker 2007; Agertz et al. 2009; Aumer et al. 2010; Bournaud et al. 2010), magnetorotational instabilities (e.g., Kim et al. 2003; Piontek & Ostriker 2004, 2005, 2007), and non-steady motions generated in spiral shocks (e.g. Kim & Ostriker 2006; Kim et al. 2006, 2010; Dobbs et al. 2006). Turbulence driven by these processes has lower vertical than horizontal velocity dispersions, because they all tap galactic rotation. Rotational-gravitational instabilities are able to produce turbulence levels comparable to observed values, although vertical dispersions drop to $\lesssim 4 \text{ km s}^{-1}$ after several galactic orbits (Agertz et al. 2009). In addition, gravitationally-driven turbulence is dominated by large scales (i.e., clump-to-clump motions) that do not prevent collapse within clumps. Without stellar feedback to unbind dense clouds that form, the resulting star formation rates are too high. Gravitationally-driven turbulence is likely to be most important during the transient, gas-rich early stages of galaxy formation at high redshift (e.g. Ceverino et al. 2010). Characterizing turbulence in galaxies requires subtraction of a "background state," and this becomes more difficult to define when there are large secular motions including prominent radial flows and collapsing clumps. Even

steady spiral shocks create a (steady) azimuthal velocity profile that can differ by tens of km s^{-1} from the background rotation curve. It will be interesting to analyze in detail how non-stellar processes combine with stellar feedback to power turbulence over both large and small scales in disk galaxies, providing a more complete understanding of galactic star formation over all redshifts.

As noted above, the present numerical models involve radical simplifications compared to the real star-forming ISM. Given the success of these simple models, it is clearly worthwhile to pursue further computational modeling along similar lines, improving on the numerical idealizations we have made. One of the advantages of local numerical models that resolve $\sim$ pc$-$ kpc is that the scales involved directly correspond to those accessible in high-resolution observations of nearby galaxies. Results from successive model refinements can be compared to observations to identify a "minimal physics" set, incorporating only the most important effects to minimize computational cost.

By employing high-resolution ISM simulations to identify the key processes controlling star formation, it will be possible to enhance subgrid models for computational galaxy formation studies in the cosmological context. While feedback to drive turbulent pressure plays a dominant role in the ISM of the Milky Way and similar galaxies, feedback to drive thermal pressure is likely to be increasingly important where there is minimal dust shielding, potentially leading to large $f_{\rm rad}$ and $\eta_{\rm th} \gg \eta_{\rm turb}$. Some current simulations of dust-poor galaxies at high redshift use subgrid shielding models to estimate the abundance of cold, star-forming gas (e.g. Gnedin et al. 2009; Gnedin & Kravtsov 2010; Kuhlen et al. 2011). A subgrid model that incorporates both shielding and turbulence could potentially bridge over a wide range of redshifts.

REFERENCES

Agertz, O., Lake, G., Moore, B., et al. 2009, MNRAS, 392, 294

Agertz, O., Teyssier, R., & Moore, B. 2011, MNRAS, 410, 1391

Audit, E., & Hennebelle, P. 2005, A&A, 433, 1

Audit, E., & Hennebelle, P. 2010, A&A, 511, 76

Aumer, M., Burkert, A., Johansson, P. H., & Genzel, R. 2010, ApJ, 719, 1230

de Avillez, M. A., & Berry, D. L. 2001, MNRAS, 328, 708

de Avillez, M. A., & Breitschwerdt, D. 2005, A&A, 436, 585

Bakes, E. L. O., & Tielens, A. G. G. M. 1994, ApJ, 427, 822

Basu, S., Mouschovias, T. C., & Paleologou, E. V. 1997, ApJ, 480, L55

Begelman, M. C., & McKee, C. F. 1990, ApJ, 358, 375

Bigiel, F., Leroy, A. K., Walter, F., et al. 2008, AJ, 136, 2846

Bigiel, F., Leroy, A. K., Walter, F., et al. 2010, AJ, 140, 1194

Bigiel, F., Leroy, A. K., Walter, F., et al. 2011, ApJ, 730, L13

Blitz, L., & Rosolowsky, E. 2004, ApJ, 612, L29

Blitz, L., & Rosolowsky, E. 2006, ApJ, 650, 933

Boissier, S., Prantzos, N., Boselli, A., & Gavazzi, G. 2003, MNRAS, 346, 1215

Bolatto, A. D., Leroy, A. K., Rosolowsky, E., et al. 2008, ApJ, 686, 948

Bolatto, A. D., Leroy, A. K., Jameson, K., et al. 2011, ApJ, in press (arXiv:1107.1717)

Bournaud, F., & Elmegreen, B. G. 2009, ApJ, 694, L158

Bournaud, F., Elmegreen, B. G., & Elmegreen, D. M. 2007, ApJ, 670, 237

Bournaud, F., Elmegreen, B. G., Teyssier, R., et al. 2010, MNRAS, 409, 1088

Braun, R. 1997, ApJ, 484, 637

Ceverino, D., Dekel, A., & Bournaud, F. 2010, MNRAS, 404, 2151

Cioffi, D. F., McKee, C. F., & Bertschinger, E. 1988, ApJ, 334, 252

Daddi, E., Elbaz, D., Walter, F., et al. 2010, ApJ, 714, L118

Dickey, J. M., Hanson, M. M., & Helou, G. 1990, ApJ, 352, 522

Dickey, J. M. & Lockman, F. J. 1990, ARA&A, 28, 215

Dickey, J. M., Mebold, U., Stanimirovic, S., & Staveley-Smith, L. 2000, ApJ, 536, 756

Dickey, J. M., Strasser, S., Gaensler, B. M., et al. 2009, ApJ, 693, 1250

Dobbs, C. L., & Bonnell, I. A. 2006, MNRAS, 367, 873

Dobbs, C. L., & Bonnell, I. A. 2008, MNRAS, 385, 1893

Dobbs, C. L., Bonnell, I. A., Pringle, J. E. 2006, MNRAS, 367, 873

Dobbs, C. L., Glover, S. C. O., Clark, P. C., & Klessen, R. S. 2008, MNRAS, 389, 1097

Dobbs, C. L., Burkert, A., & Pringle, J. E. 2011, MNRAS, in press (arXiv:1107.0154)

Elmegreen, B. G. 1997, RMxAC, 6, 165

Fuchs, B., Jahreiß, H., & Flynn, C. 2009, AJ, 137, 266

Field, G. B. 1965, ApJ, 142, 531

Field, G. B., Goldsmith, D. W., & Habing, H. J. 1969, ApJ, 155, L149

Gazol, A., Luis, L., & Kim, J. 2009, ApJ, 693, 656

Gazol, A., Vázquez-Semadeni, E., & Kim, J. 2005, ApJ, 630, 911

Genzel, R., Tacconi, L. J., Garcia-Carpio, J., et al. 2010, MNRAS, 407, 2091

Gnedin, N. Y., & Kravtsov, A. V. 2010, ApJ, 714, 287

Gnedin, N. Y., Tassis, K., & Kravtsov, A. V. 2009, ApJ, 697, 55

Governato, F., Willman, B., Mayer, L., et al. 2007, MNRAS, 374, 1479

Hawley, J. F., Gammie, C. F., & Balbus, S. A. 1995, ApJ, 440, 742

Heiles, C., & Troland, T. H. 2003, ApJ, 586, 1067

Hennebelle, P. & Audit, E. 2007, A&A, 465, 431

Heyer, M., Krawczyk, C., Duval, J., & Jackson, J. M. 2009, ApJ, 699, 1092

Hopkins, P. F., Quataert, E., & Murray, N. 2011, MNRAS, submitted (arXiv:1107.0154)

Joung, M. K. R., & Mac Low, M.-M. 2006, ApJ, 653, 1266

Joung, M. K. R., Mac Low, M.-M., & Bryan, G. L. 2009, ApJ, 704, 137

Kalberla, P. M. W. & Kerp, J. 2009, ARA&A, 47, 27

Katz, N. 1992, ApJ, 391, 502

Kennicutt, R. C., Jr. 1998, ApJ, 498, 541

Kim, C.-G., Kim, W.-T., & Ostriker, E. C. 2006, ApJ, 649, L13

Kim, C.-G., Kim, W.-T., & Ostriker, E. C. 2008, ApJ, 681, 1148

Kim, C.-G., Kim, W.-T., & Ostriker, E. C. 2010, ApJ, 720, 1454

Kim, J., Hong, S. S., Ryu, D., & Jones, T. W. 1998, ApJ, 506, L139

Kim, J., Ryu, D., & Jones, T. W. 2001, ApJ, 557, 464

Kim, W.-T., & Ostriker, E. C. 2001, ApJ, 559, 70

Kim, W.-T., & Ostriker, E. C. 2002, ApJ, 570, 132

Kim, W.-T., & Ostriker, E. C. 2006, ApJ, 646, 213

Kim, W.-T., & Ostriker, E. C. 2007, ApJ, 660, 1232

Kim, W.-T., Ostriker, E. C., & Stone, J. M. 2002, ApJ, 581, 1080

Kim, W.-T., Ostriker, E. C., & Stone, J. M. 2003, ApJ, 599, 1157

Koo, B.-C., & Kang, J.-H. 2004, MNRAS, 349, 983

Koyama, H., & Inutsuka, S. 2002, ApJ, 564, L97

Koyama, H., & Inutsuka, S. 2004, ApJ, 602, L25

Koyama, H., & Ostriker, E. C. 2009a, ApJ, 693, 1316

Koyama, H., & Ostriker, E. C. 2009b, ApJ, 693, 1346

Kroupa, P. 2001, MNRAS, 322, 231

Krumholz, M. R., McKee, C. F. 2005, ApJ, 630, 250

Krumholz, M. R., & Tan, J. C. 2007, ApJ, 654, 304

Kuhlen, M., Krumholz, M., Madau, P., et al. 2011, ApJ, submitted (arXiv:1105.2376)

Lemaster, M. N., & Stone, J. M. 2009, ApJ, 691, 1091

Leroy, A. K., Walter, F., Brinks, E., et al. 2008, AJ, 136, 2782

Li, Y., Mac Low, M.-M., & Klessen, R. S. 2005, ApJ, 626, 823

Mac Low, M.-M., & Klessen, R. S. 2004, RvMP, 76, 125

Mac Low, M.-M., Klessen, R. S., Burkert, A., & Smith, M. D. 1998, PhRvL, 80, 2754

McCray, R., Kafatos, M., & Stein, R. F. 1975, ApJ, 196, 565

McKee, C. F., & Ostriker, E. C. 2007, ARA&A, 45, 565

Mufson, S. L. 1974, ApJ, 193, 561

Mouschovias, T. C., Kunz, M. W., & Christie, D. A. 2009, MNRAS, 397, 14

Ostriker, E. C., McKee, C. F., & Leroy, A. K. 2010, ApJ, 721, 975 (OML10)

Ostriker, E. C., & Shetty, R. 2011, ApJ, 731, 41 (OS11)

Parravano, A., Hollenbach, D. J., & McKee, C. F. 2003, ApJ, 584, 797

Parker, E. N. 1953, ApJ, 117, 431

Petric, A. O., & Rupen, M. P. 2007, AJ, 134, 1952

Piontek, R. A., & Ostriker, E. C. 2004, ApJ, 601, 905

Piontek, R. A., & Ostriker, E. C. 2005, ApJ, 629, 849

Piontek, R. A., & Ostriker, E. C. 2007, ApJ, 663, 183

Quirk, W. J. 1972, ApJ, 176, L9

Roman-Duval, J., Jackson, J. M., Heyer, M., et al. 2010, ApJ, 723, 492

Ryder, S. D., & Dopita, M. A. 1994, ApJ, 430, 142

Salim, S., Rich, R. M., Charlot, S., et al. 2007, ApJS, 173, 267

Shetty, R., & Ostriker, E. C. 2006, ApJ, 647, 997

Shetty, R., & Ostriker, E. C. 2008, ApJ, 684, 978

Shi, Y., Helou, G., Yan, L., et al. 2011, ApJ, 733, 87

Silk, J. 1997, ApJ, 481, 703

Solomon, P. M., Rivolo, A. R., Barrett, J., & Yahil, A. 1987, ApJ, 319, 730

Sternberg, A., McKee, C. F., & Wolfire, M. G. 2002, ApJS, 143, 419

Stone, J. M., & Gardiner, T. A. 2009, NewA, 14, 139

Stone, J. M., Gardiner, T. A., Teuben, P. et al. 2008, ApJS, 178, 137

Stone, J. M., Ostriker, E. C., & Gammie, C. F. 1998, ApJ, 508, L99

Tasker, E. J. 2011, ApJ, 730, 11

Tasker, E. J., & Bryan, G. L. 2006, ApJ, 641, 878

Tasker, E. J., & Tan, J. C. 2009, ApJ, 700, 358

Thacker, R. J., & Couchman, H. M. P. 2001, ApJ, 555, L17

Truelove, J. K., Klein, R. I., McKee, C. F., et al. 1997, ApJ, 489, 179

Truelove, J. K., Klein, R. I., McKee, C. F., et al. 1998, ApJ, 495, 821

van Zee, L., & Bryant, J. 1999, AJ, 118, 2172

Wada, K. 2008, ApJ, 675, 188

Wada, K., & Koda, J. 2004, MNRAS, 349, 270

Wada, K., Meurer, G., & Norman, C. A. 2002, ApJ, 577, 197

Wada, K., Baba, J., & Saitoh, T. R. 2011, ApJ, 735, 1

Wada, K., & Norman, C. A. 1999, ApJ, 516, L13

Wada, K., & Norman, C. A. 2007, ApJ, 660, 276

Wolfire, M. G., McKee, C. F., Hollenbach, D., et al. 1995, ApJ, 443, 152

Wolfire, M. G., McKee, C. F., Hollenbach, D., & Tielens, A. G. G. M. 2003, ApJ, 587, 278

Wong, T., & Blitz, L. 2002, ApJ, 569, 157

Wyse, R. F. G., & Silk, J. 1989, ApJ, 339, 700

Young, L. M., van Zee, L., Lo, K. Y., et al. 2003, ApJ, 592, 111

Table 1.   Model Parameters

Model	Σ [$M_\odot$ pc^{-2}]	$\rho_{\rm sd}$ [$M_\odot$ pc^{-3}]	Ω [km s^{-1} kpc^{-1}]	H_w [pc]	L_z [pc]	s_0
QA02	2.5	0.0031	7	528	2048	0.28
QA05	5.0	0.0125	14	269	1024	0.28
QA07	7.5	0.0281	21	179	768	0.28
QA10	10.0	0.0500	28	134	512	0.28
QA15	15.0	0.1125	42	89	384	0.28
QA20	20.0	0.2000	56	67	256	0.28
QB02	2.5	0.0125	7	269	1024	0.07
QB05	5.0	0.0500	14	134	768	0.07
QB07	7.5	0.1125	21	89	512	0.07
QB10	10.0	0.2000	28	67	384	0.07
QB15	15.0	0.4500	42	44	256	0.07
S02	2.5	0.0500	7	134	768	0.02
S05	5.0	0.0500	14	134	768	0.07
S07	7.5	0.0500	21	134	512	0.16
S10	10.0	0.0500	28	134	512	0.28
S15	15.0	0.0500	42	134	512	0.62
S20	20.0	0.0500	56	134	512	1.10
G02	10.0	0.0250	28	190	768	0.55
G05	10.0	0.0500	28	134	512	0.28
G10	10.0	0.1000	28	95	512	0.14
G20	10.0	0.2000	28	67	384	0.07

Note. — Models S05, S10, G05, and G20 are identical to QB05, QA10, QA10, and QB10 models, respectively. All models in Series QA, QB, S, and G have $f_{\rm rad}$ = 1. Models in the R series (not listed) have the same parameters as model QA10, except $f_{\rm rad}$ = 0.25, 0.5, 2.5, and 5.0 for R02, R05, R25, and R50, respectively. All models have L_x = 512 pc except model QA10x2, which is the same as QA10 but with L_x = 1024 pc.

Table 2.   Disk Properties 1

Model (1)	$\log\langle\Sigma_{\rm SFR}\rangle$ (2)	$\log\langle P_{\rm th}/k_{\rm B}\rangle$ (3)	$\log\langle P_{\rm turb}/k_{\rm B}\rangle$ (4)	$\langle n_0\rangle$ (5)	$\langle H_{\rm diff}\rangle$ (6)
QA02	-4.20 ± 0.23	1.94 ± 0.35	2.61 ± 1.51	0.05 ± 0.08	342 ± 111
QA05	-3.52 ± 0.12	2.53 ± 0.22	3.03 ± 0.72	0.39 ± 0.30	174 ± 37
QA07	-3.03 ± 0.11	2.95 ± 0.16	3.57 ± 0.73	0.82 ± 0.46	132 ± 29
QA10	-2.74 ± 0.11	3.24 ± 0.15	3.85 ± 0.60	1.12 ± 0.58	92 ± 18
QA10x2	-2.72 ± 0.09	3.23 ± 0.08	3.74 ± 0.52	1.32 ± 0.40	94 ± 10
QA15	-2.38 ± 0.10	3.50 ± 0.11	4.08 ± 0.51	1.70 ± 0.69	70 ± 9
QA20	-2.06 ± 0.10	3.86 ± 0.07	4.19 ± 0.63	2.76 ± 0.70	51 ± 5
QB02	-3.85 ± 0.15	2.29 ± 0.23	2.71 ± 0.63	0.30 ± 0.26	157 ± 53
QB05	-3.15 ± 0.08	2.81 ± 0.21	3.45 ± 0.61	0.56 ± 0.40	118 ± 38
QB07	-2.79 ± 0.12	3.19 ± 0.13	3.75 ± 0.71	1.07 ± 0.55	77 ± 20
QB10	-2.58 ± 0.09	3.43 ± 0.13	3.90 ± 0.62	1.88 ± 0.86	56 ± 12
QB15	-2.24 ± 0.05	3.72 ± 0.09	4.27 ± 0.55	2.97 ± 0.98	44 ± 6
S02	-3.45 ± 0.07	2.60 ± 0.23	3.25 ± 0.56	0.40 ± 0.30	110 ± 33
S07	-2.93 ± 0.07	3.08 ± 0.12	3.62 ± 0.68	1.09 ± 0.47	90 ± 13
S15	-2.43 ± 0.11	3.44 ± 0.12	3.96 ± 0.70	1.50 ± 0.94	95 ± 22
S20	-2.31 ± 0.10	3.64 ± 0.07	4.08 ± 0.53	1.79 ± 0.58	87 ± 7
G02	-2.82 ± 0.08	3.13 ± 0.20	3.66 ± 0.77	0.88 ± 0.52	136 ± 34
G10	-2.66 ± 0.06	3.31 ± 0.14	3.86 ± 0.60	1.57 ± 0.68	82 ± 13
R02	-2.61 ± 0.06	2.73 ± 0.25	3.97 ± 0.66	0.98 ± 0.54	99 ± 15
R05	-2.72 ± 0.08	2.94 ± 0.15	3.85 ± 0.77	1.42 ± 0.48	96 ± 17
R25	-2.87 ± 0.12	3.48 ± 0.12	3.53 ± 0.60	1.11 ± 0.45	92 ± 12
R50	-2.96 ± 0.22	3.69 ± 0.16	3.31 ± 0.37	1.29 ± 0.58	97 ± 20

Note. — The mean values and standard deviations of physical quantities are averaged over $t/t_{\rm orb}=2-3$. Col. (2): Logarithmic value of the SFR surface density ($M_\odot$ kpc^{-2} yr^{-1}). Cols. (3)-(4): Logarithmic values of the midplane thermal and turbulent pressures over $k_{\rm B}$ (cm^{-3} K). Col. (5): Midplane number density of hydrogen (cm^{-3}). Col. (6): Scale height of the diffuse component (pc). See Section 4.2 for definitions.

Table 3.   Disk Properties 2

Model (1)	$\langle v_{z,diff}\rangle$ (2)	$\langle v_{th,diff}\rangle$ (3)	$\langle \sigma_z\rangle$ (4)	$\langle f_{diff}\rangle$ (5)	α (6)	$\tilde{f}_w$ (7)	$\tau_{SF,GBC}$ (8)
QA02	6.20 ± 4.57	3.27 ± 0.78	6.86 ± 4.67	0.92 ± 0.07	4.59 ± 5.56	0.23 ± 0.12	3.31 ± 3.35
QA05	6.28 ± 2.95	3.25 ± 0.43	6.78 ± 2.85	0.90 ± 0.06	4.74 ± 3.65	0.25 ± 0.07	1.73 ± 1.17
QA07	6.90 ± 2.78	3.49 ± 0.46	7.36 ± 2.51	0.89 ± 0.06	4.90 ± 3.31	0.29 ± 0.08	0.92 ± 0.56
QA10	7.23 ± 2.28	3.73 ± 0.42	7.39 ± 2.02	0.77 ± 0.09	4.75 ± 2.51	0.32 ± 0.07	1.26 ± 0.60
QA10x2	6.80 ± 2.07	3.74 ± 0.18	7.01 ± 1.73	0.77 ± 0.06	4.31 ± 2.04	0.32 ± 0.03	1.19 ± 0.40
QA15	6.95 ± 1.94	4.05 ± 0.30	7.02 ± 1.71	0.67 ± 0.06	3.95 ± 1.70	0.36 ± 0.05	1.20 ± 0.36
QA20	6.94 ± 1.67	4.59 ± 0.22	6.80 ± 1.30	0.54 ± 0.06	3.29 ± 1.12	0.46 ± 0.05	1.06 ± 0.27
QB02	5.35 ± 3.26	2.93 ± 0.39	5.87 ± 3.18	0.91 ± 0.08	4.32 ± 4.15	0.19 ± 0.05	1.64 ± 1.47
QB05	7.07 ± 3.34	3.36 ± 0.45	7.37 ± 3.02	0.87 ± 0.08	5.44 ± 4.36	0.27 ± 0.07	0.89 ± 0.59
QB07	7.15 ± 2.81	3.62 ± 0.31	7.16 ± 2.43	0.76 ± 0.09	4.89 ± 3.13	0.30 ± 0.05	1.12 ± 0.53
QB10	6.68 ± 2.17	3.70 ± 0.32	6.55 ± 1.79	0.67 ± 0.08	4.25 ± 2.19	0.31 ± 0.06	1.26 ± 0.41
QB15	7.88 ± 2.05	4.02 ± 0.26	7.29 ± 1.58	0.59 ± 0.05	4.83 ± 2.06	0.35 ± 0.04	1.07 ± 0.18
S02	7.14 ± 3.58	3.04 ± 0.41	7.25 ± 3.30	0.84 ± 0.08	6.53 ± 5.75	0.22 ± 0.06	1.12 ± 0.62
S07	6.41 ± 2.68	3.50 ± 0.29	6.80 ± 2.44	0.82 ± 0.05	4.35 ± 2.85	0.29 ± 0.05	1.12 ± 0.38
S15	6.76 ± 1.92	4.25 ± 0.31	7.01 ± 1.76	0.70 ± 0.10	3.54 ± 1.49	0.40 ± 0.06	1.20 ± 0.51
S20	6.08 ± 1.43	4.42 ± 0.22	6.62 ± 1.25	0.67 ± 0.05	2.89 ± 0.91	0.43 ± 0.05	1.34 ± 0.37
G02	7.13 ± 2.26	4.00 ± 0.34	7.68 ± 2.11	0.85 ± 0.05	4.18 ± 2.09	0.37 ± 0.06	1.01 ± 0.39
G10	6.82 ± 1.99	3.83 ± 0.30	6.99 ± 1.77	0.74 ± 0.07	4.17 ± 1.91	0.34 ± 0.05	1.18 ± 0.37
R02	8.36 ± 2.35	2.28 ± 0.19	7.85 ± 1.92	0.78 ± 0.07	14.51 ± 7.93	0.11 ± 0.02	0.91 ± 0.32
R05	6.80 ± 2.01	2.87 ± 0.28	6.84 ± 1.92	0.80 ± 0.06	6.62 ± 3.50	0.19 ± 0.04	1.05 ± 0.37
R25	5.25 ± 1.77	4.87 ± 0.40	6.72 ± 1.91	0.77 ± 0.06	2.16 ± 0.80	0.54 ± 0.09	1.69 ± 0.65
R50	4.49 ± 1.85	5.70 ± 0.49	6.78 ± 1.84	0.85 ± 0.07	1.62 ± 0.52	0.73 ± 0.12	1.39 ± 0.92

Note. — The mean values and standard deviations of physical quantities are averaged over $t/t_{orb}=2-3$. Cols. (2)-(3): Vertical turbulent and thermal velocity dispersions of the diffuse gas (km s^{-1}). Col. (4): Total vertical velocity dispersion for all gas (km s^{-1}). Cols. (5)-(7): Mass fraction of the diffuse gas (f_{diff}), the ratio of total pressure to turbulent pressure (α), and the square of mass-weighted thermal to warm-medium thermal speed ($v_{th,diff}^2/c_w^2 = \tilde{f}_w$) in the diffuse gas. Col. (8): Timescale to convert dense gas into stars (Gyr). See Section 4.2 for definitions.
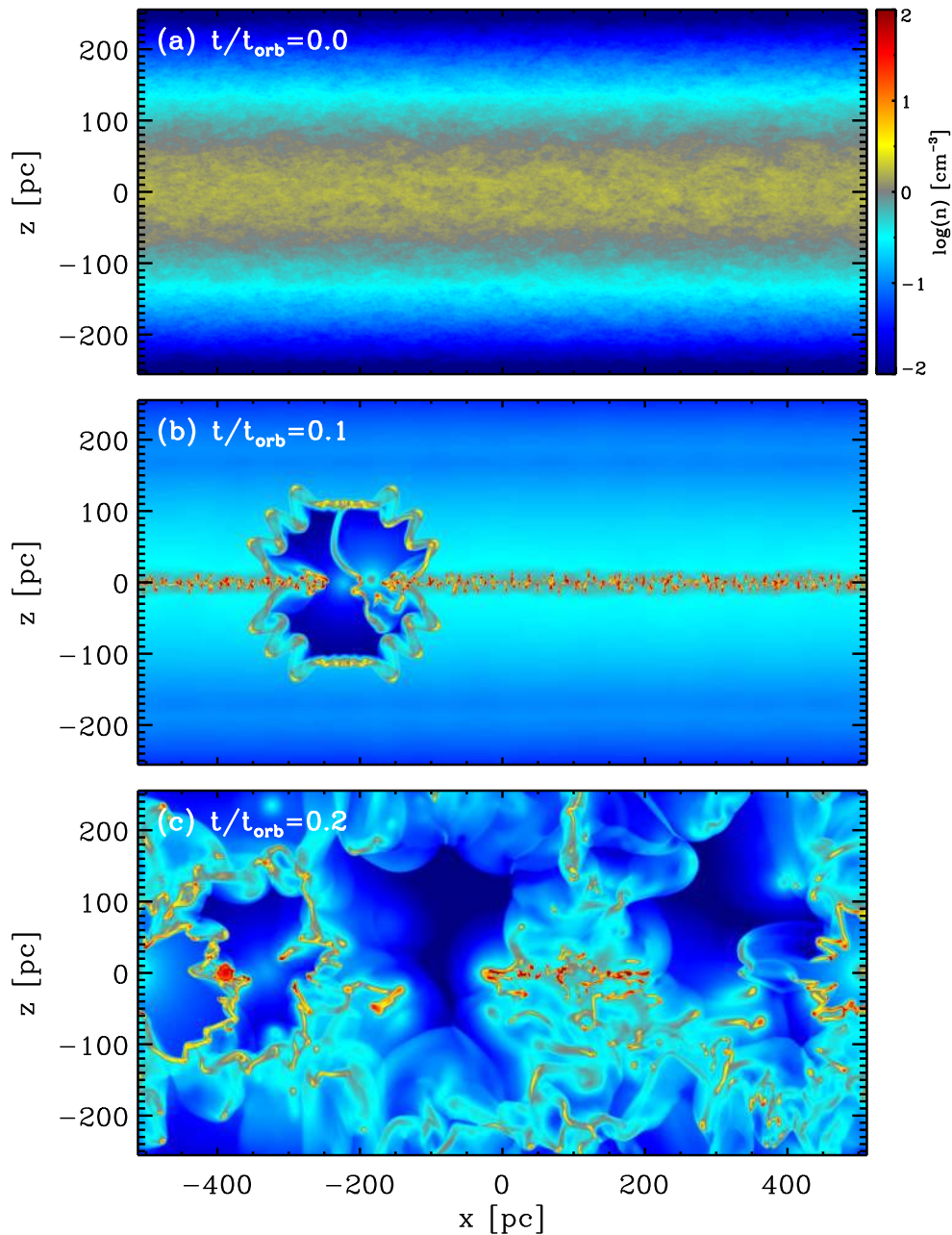
Fig. 1.— Density snapshots for Model QA10x2 (logarithmic color scale) at $t/t_{\rm orb} = 0$, 0.1, and 0.2. The initial single-temperature gas disk (*a*) evolves rapidly via thermal instability into a configuration with mid-plane cold cloudlets sandwiched by outer layers of warm gas. In (*b*), the first SN explosions occur in dense clouds near $x = -200$ pc produced by mergers and self-gravitating contraction of smaller clouds. Subsequent SN explosions disperse the dense clouds and drive the disk into a turbulent state (*c*), in which filamentary structures of cold gas are found at all heights.
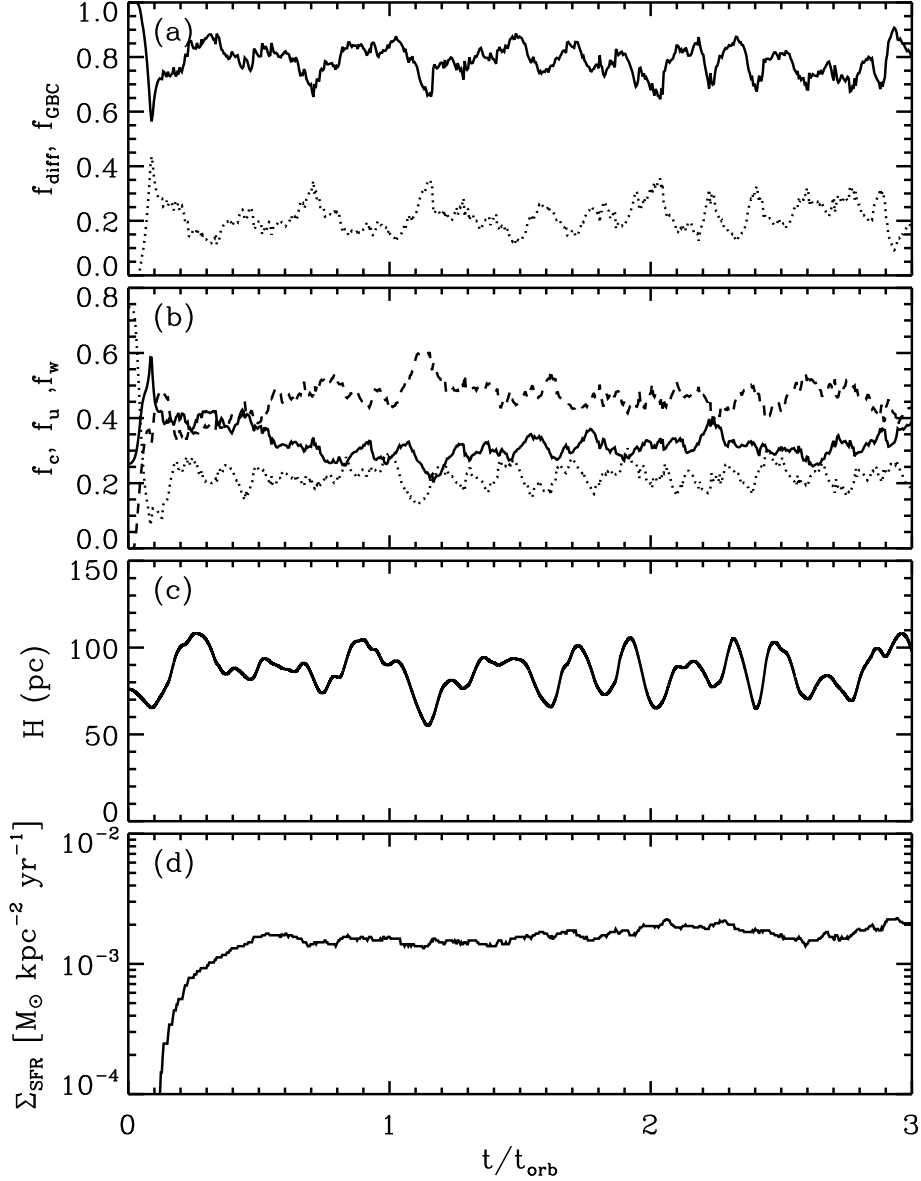
Fig. 2.— Time evolution in Model QA10x2 of (*a*) the mass fractions of the diffuse ($f_{\rm diff}$, solid) and GBC ($f_{\rm GBC}$, dotted) components, (*b*) the mass fractions of the cold (f_c, dashed), unstable (f_u, dotted), and warm (f_w, solid) phases within the diffuse component, (*c*) the density-weighted vertical scale height H, and (*d*) the SFR surface density $\Sigma_{\rm SFR}$. The initial increase of $f_{\rm GBC}$ and f_c stops at $t = 0.1 t_{\rm orb} = 22$ Myr when the first SN event occurs inside a massive dense cloud. The model reaches a quasi-steady state after a few tenths of an orbital time, in the sense that the physical quantities fluctuate but do not evolve secularly. Note that $f_{\rm diff}$ is positively correlated with H.
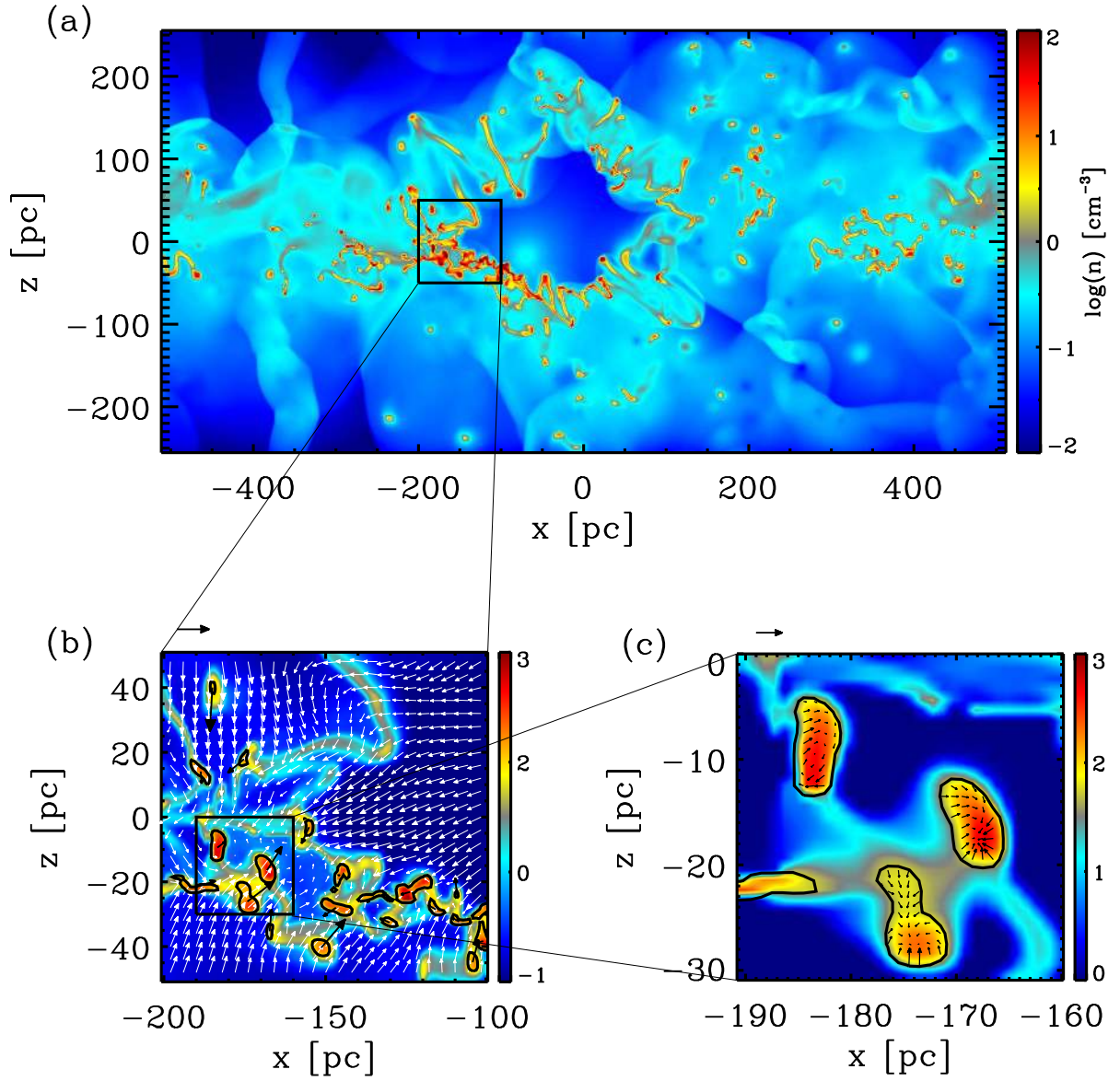
Fig. 3.— (a) Density structure in the whole simulation domain of Model QA10x2 at $t/t_{\rm orb} = 2.22$, including a large, fragmented, expanding shell produced by a recent SN event. (b) The rectangular section in (a) is enlarged to identify dense clouds ($n > 50$ cm^{-3}), outlined by black contours, that formed in a region of converging flow where the shell collides with surrounding gas. The white arrows represent the background velocity field, while the black arrows show the mean velocity of each dense cloud. (c) The section marked in (b) is further enlarged to show internal velocity structure of three selected dense clouds. The colorbars (whose range differs from panel to panel) indicate number density in logarithmic scale. The sizes of the arrows outside the boxes in (b) and (c) correspond to 10 km s^{-1} and 5 km s^{-1}, respectively.
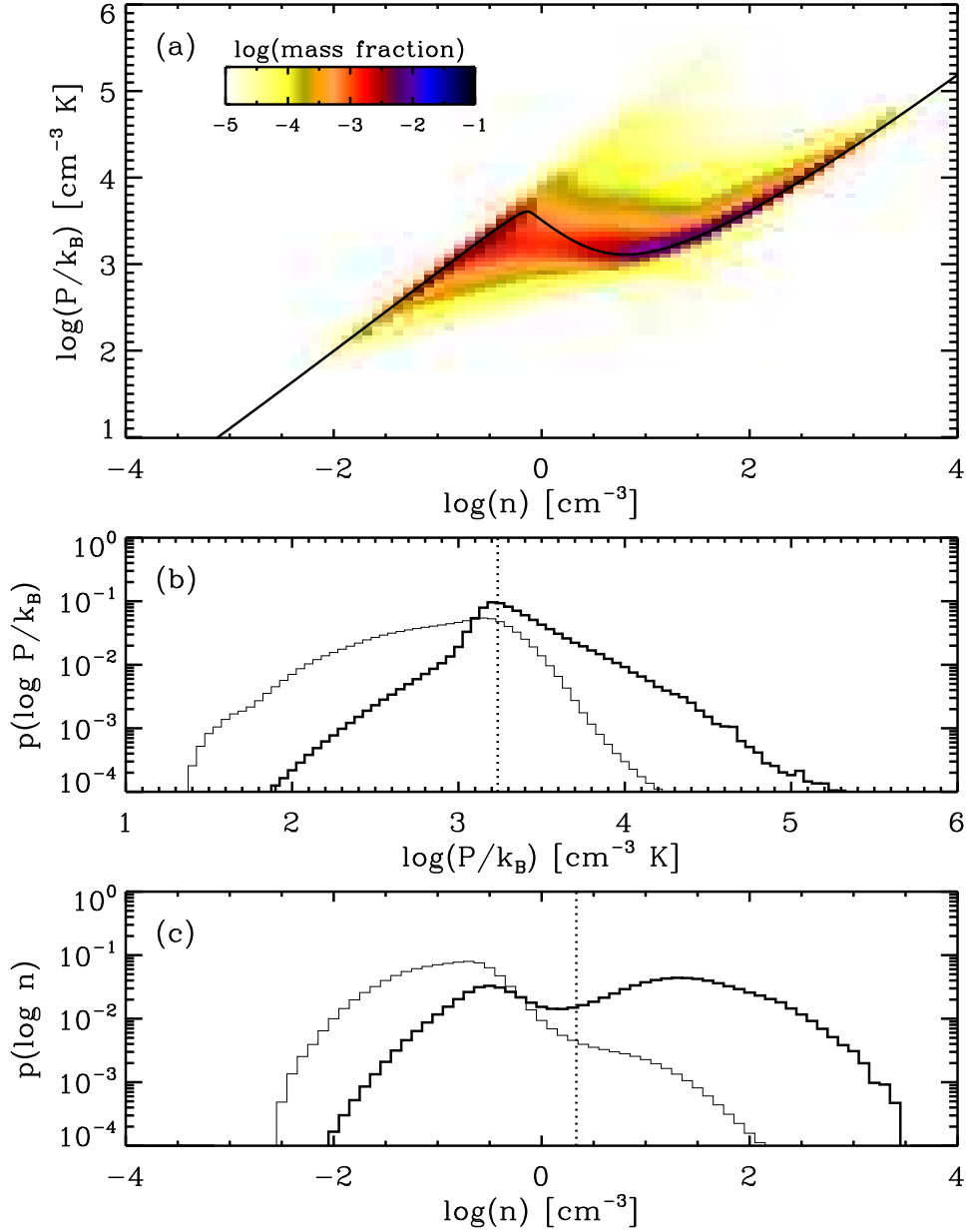
Fig. 4.— (*a*) Distribution of gas in the *n*-*P*/k_B plane for Model QA10x2, averaged over $t/t_{orb} = 2 - 3$. The colorbar gives the mass fraction in logarithmic scale. The solid curve marks the locus of thermal equilibrium at the mean heating rate of $\langle \Gamma \rangle = 0.76\Gamma_0$. Mass-weighted (*thick*) and volume-weighted (*thin*) probability distribution functions are shown for (*b*) thermal pressure and (*c*) number density. The vertical dotted lines in (*b*) and (*c*) mark the mean midplane thermal pressure and number density, respectively, of the diffuse gas. These results show that the system evolves to a state in which approximate two-phase thermal equilibrium at a common pressure holds for the atomic gas.
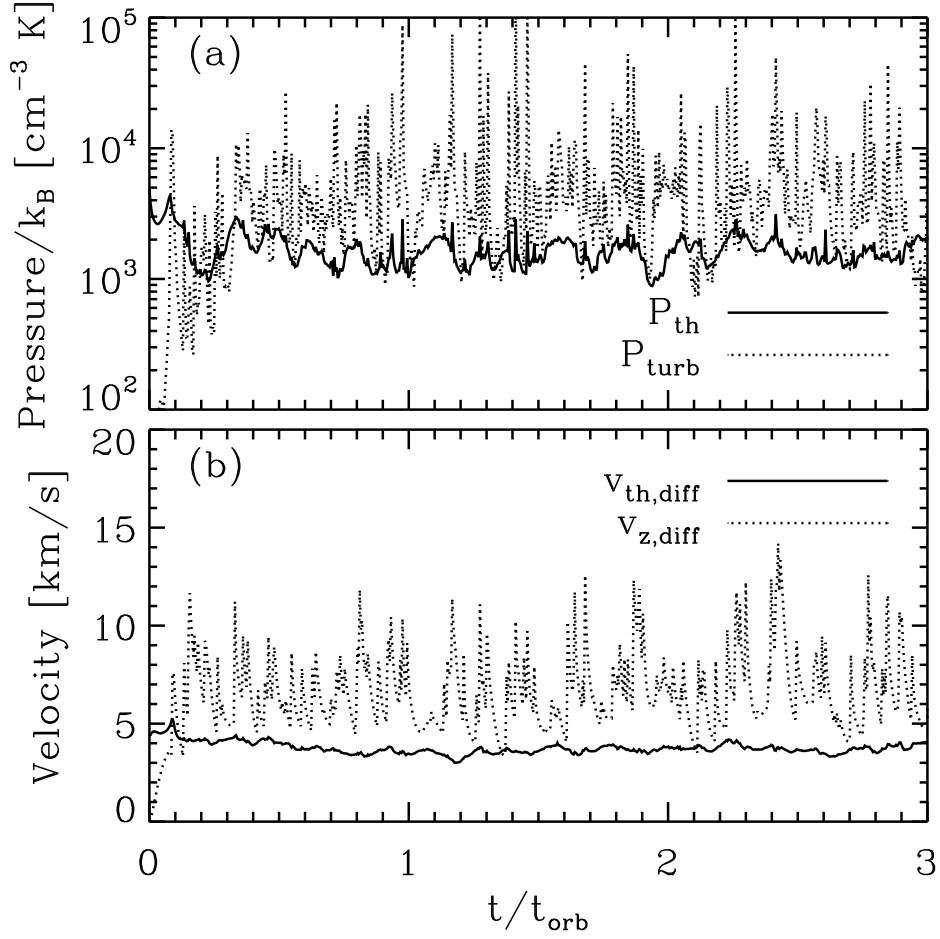
Fig. 5.— Time evolution of the midplane thermal and turbulent pressures (*a*) and the thermal and turbulent velocity dispersions (*b*) of the diffuse component for model QA10x2. In (*a*), P_{th} initially decreases as the gas cools, while P_{turb} increases rapidly after the gas falls toward midplane and is stirred up by SN explosions. After a few cloud formation and feedback cycles (a few 10s of Myr), P_{th} and P_{turb} reach saturation values of $\langle P_{th}/k_B \rangle \sim 1,680\,\mathrm{cm}^{-3}\,\mathrm{K}$ and $\langle P_{turb}/k_B \rangle \sim 5,440\,\mathrm{cm}^{-3}\,\mathrm{K}$, respectively, with a relative fluctuation amplitudes of 0.21 and 0.52. In (*b*), the velocity dispersions saturate at $\langle v_{th,diff} \rangle = 3.7\,\mathrm{km\,s}^{-1}$ and $\langle v_{z,diff} \rangle = 6.8\,\mathrm{km\,s}^{-1}$, respectively, with relative fluctuation amplitudes of 5% and 30%.
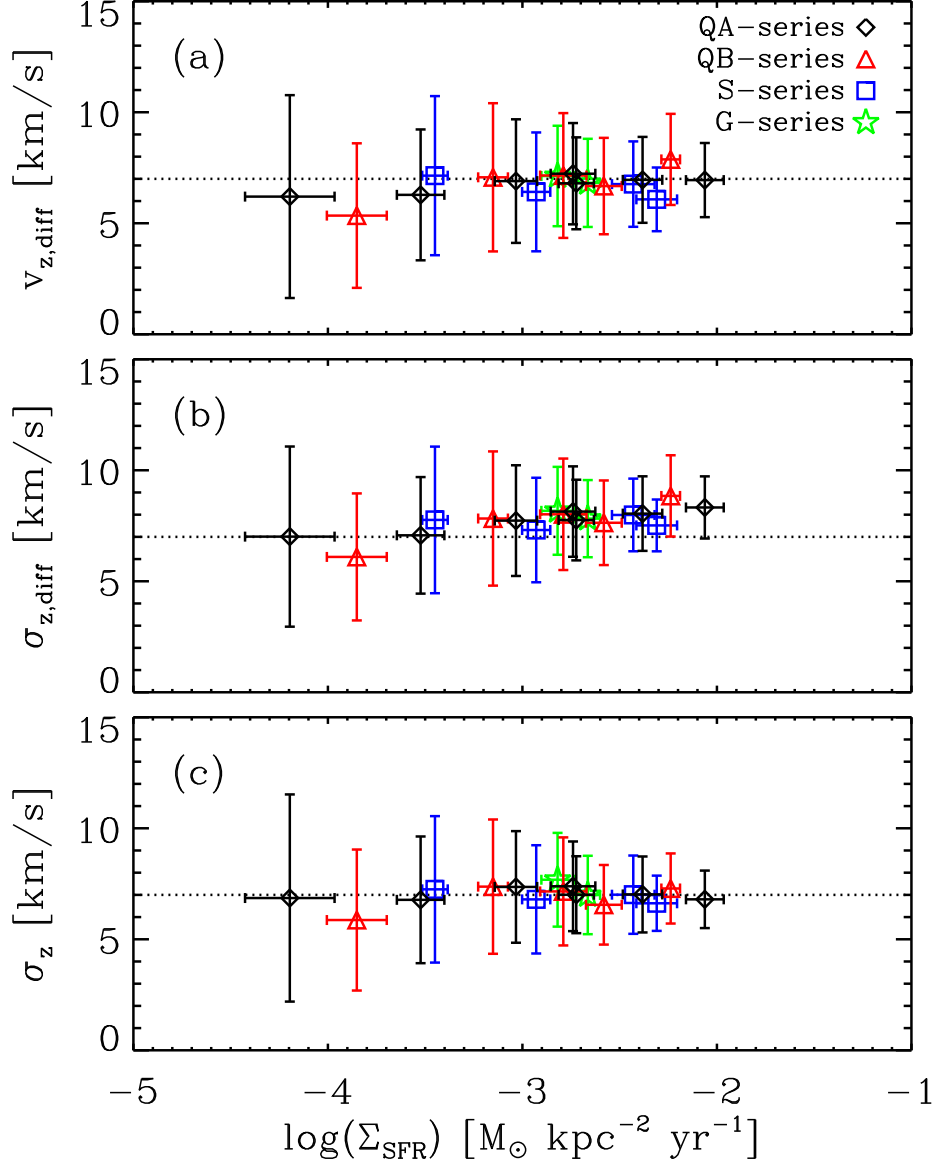
Fig. 6.— (*a*) The vertical turbulent velocity dispersion of the diffuse gas $v_{z,diff}$, (*b*) the total (turbulent+thermal) velocity dispersion of the diffuse gas $\sigma_{z,diff}$, and (*c*) the total velocity dispersion of all gas σ_z, as functions of the SFR surface density Σ_{SFR} for all models except Series R. The points and errorbars give the mean and standard deviations over $t/t_{orb} = 2-3$. For the whole set of models shown in this figure, $v_{z,diff} = 6.8 \pm 0.6$ km s^{-1}, $\sigma_{z,diff} = 7.7 \pm 0.6$ km s^{-1}, and $\sigma_z = 7.0 \pm 0.4$ km s^{-1}. The dotted lines in all panels show 7 km s^{-1} for reference.
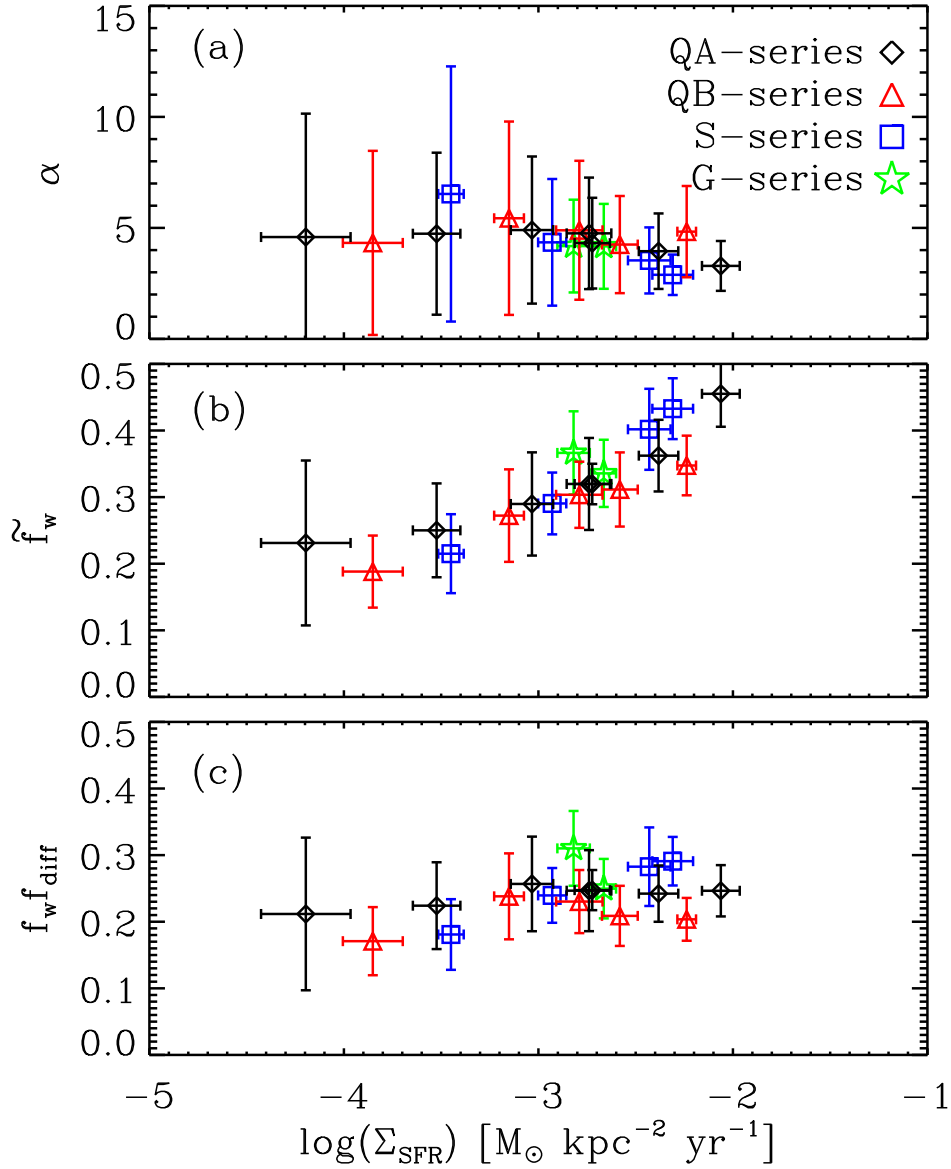
Fig. 7.— Computed values of (a) the ratio of total-to-thermal velocity dispersion for the diffuse gas $\alpha \equiv 1 + v_{z,\mathrm{diff}}^2/v_{\mathrm{th,diff}}^2$, (b) the square of mass-weighted thermal to warm-medium thermal speed $v_{\mathrm{th,diff}}^2/c_w^2 = \tilde{f}_w$, and (c) the product $f_w f_{\mathrm{diff}}$ (for $f_w \approx \tilde{f}_w$ the warm gas mass fraction in the diffuse gas and f_{diff} the diffuse mass fraction), as functions of Σ_{SFR} for all models except Series R. The points and errorbars give the mean and standard deviations over $t/t_{\mathrm{orb}} = 2-3$. Over more than two orders of magnitude in Σ_{SFR}, the balance between energy input (heating, turbulent driving) and energy output (cooling, turbulent dissipation) maintains nearly constant $\alpha = P_{\mathrm{tot}}/P_{\mathrm{th}}$ and both warm and cold gas phases.
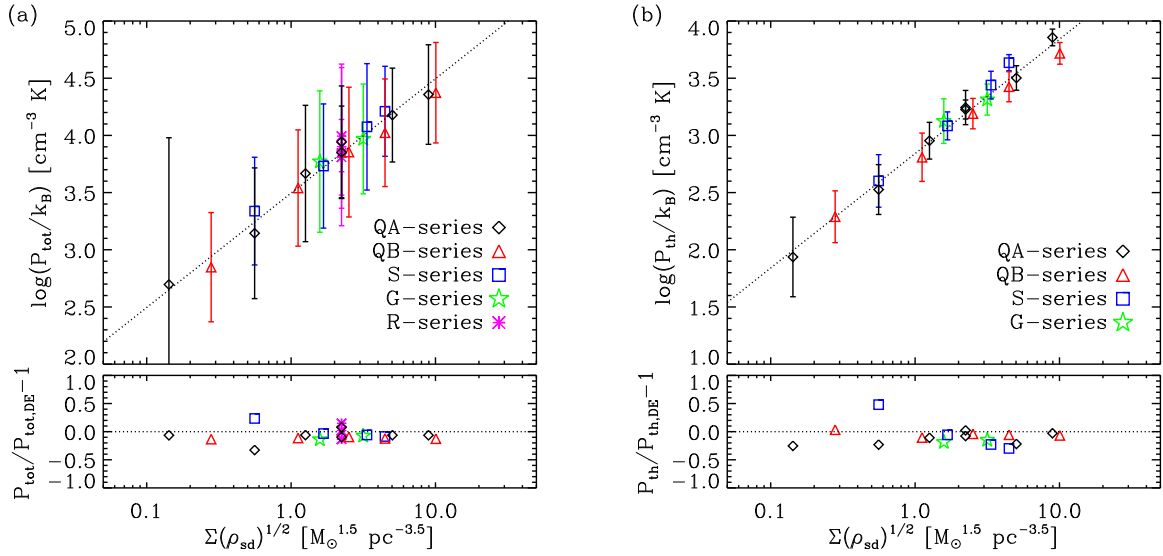
Fig. 8.— Top: Midplane (*a*) total and (*b*) thermal pressures of the diffuse gas as functions of $\Sigma\sqrt{\rho_{sd}}$. The points and errorbars give the mean and standard deviations over $t/t_{orb} = 2 - 3$. The dotted lines in upper panels show fits $P_{tot}/k_B = 9.9 \times 10^3$ cm^{-3} K$(\Sigma/10\ M_\odot\ pc^{-2})(\rho_{sd}/0.1\ M_\odot\ pc^{-3})^{1/2}$ and $P_{th}/k_B = 2.2 \times 10^3$ cm^{-3} K$(\Sigma/10\ M_\odot\ pc^{-2})(\rho_{sd}/0.1\ M_\odot\ pc^{-3})^{1/2}$, respectively. Bottom: Relative differences between measured midplane pressures and the dynamical equilibrium estimates using equation (35). The mean midplane pressure P_{tot} varies only 13% relative to $P_{tot,DE}$, showing that vertical dynamical equilibrium is an excellent approximation.
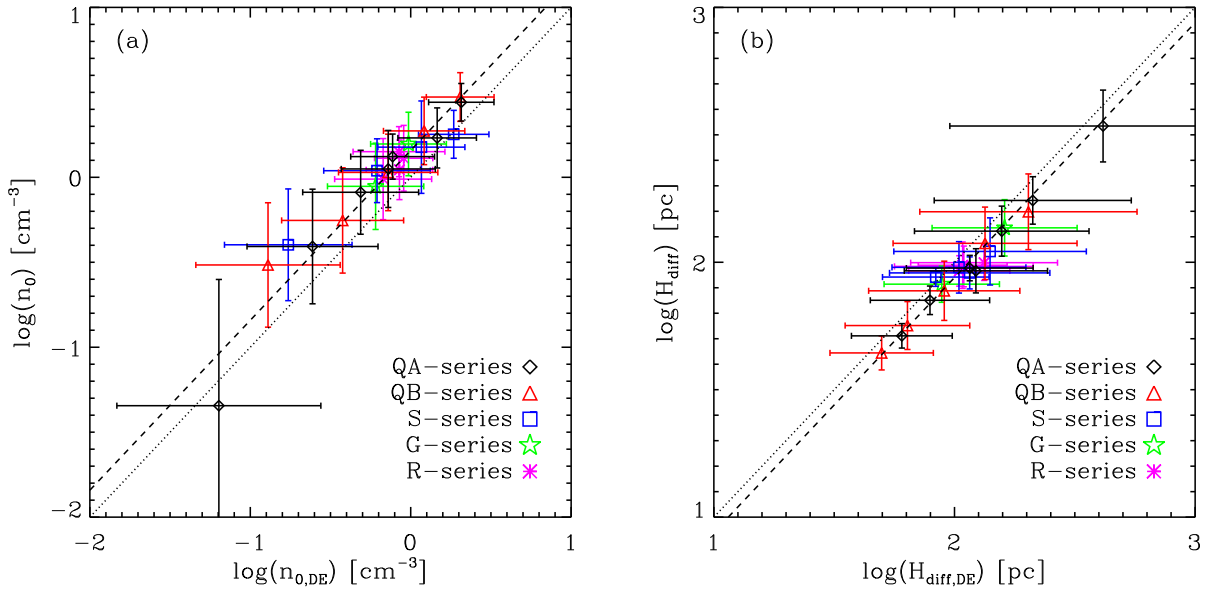
Fig. 9.— Measured *versus* estimated values of (*a*) midplane number densities and (*b*) disk scale heights of the diffuse gas. The points and errorbars give the mean and standard deviations over $t/t_{\rm orb} = 2-3$. The estimated midplane number density $n_{0,\rm DE} \equiv \rho_{0,\rm DE}/(1.4m_p)$ and scale height $H_{\rm diff,DE}$ are obtained from dynamical equilibrium as equations (39) and (40), respectively. The dashed lines show our best fits $n_0 = 1.4n_{0,\rm DE}$ and $H_{\rm diff} = 0.87H_{\rm diff,DE}$ for imposed unity slopes, while the dotted lines indicate one-to-one correspondence.
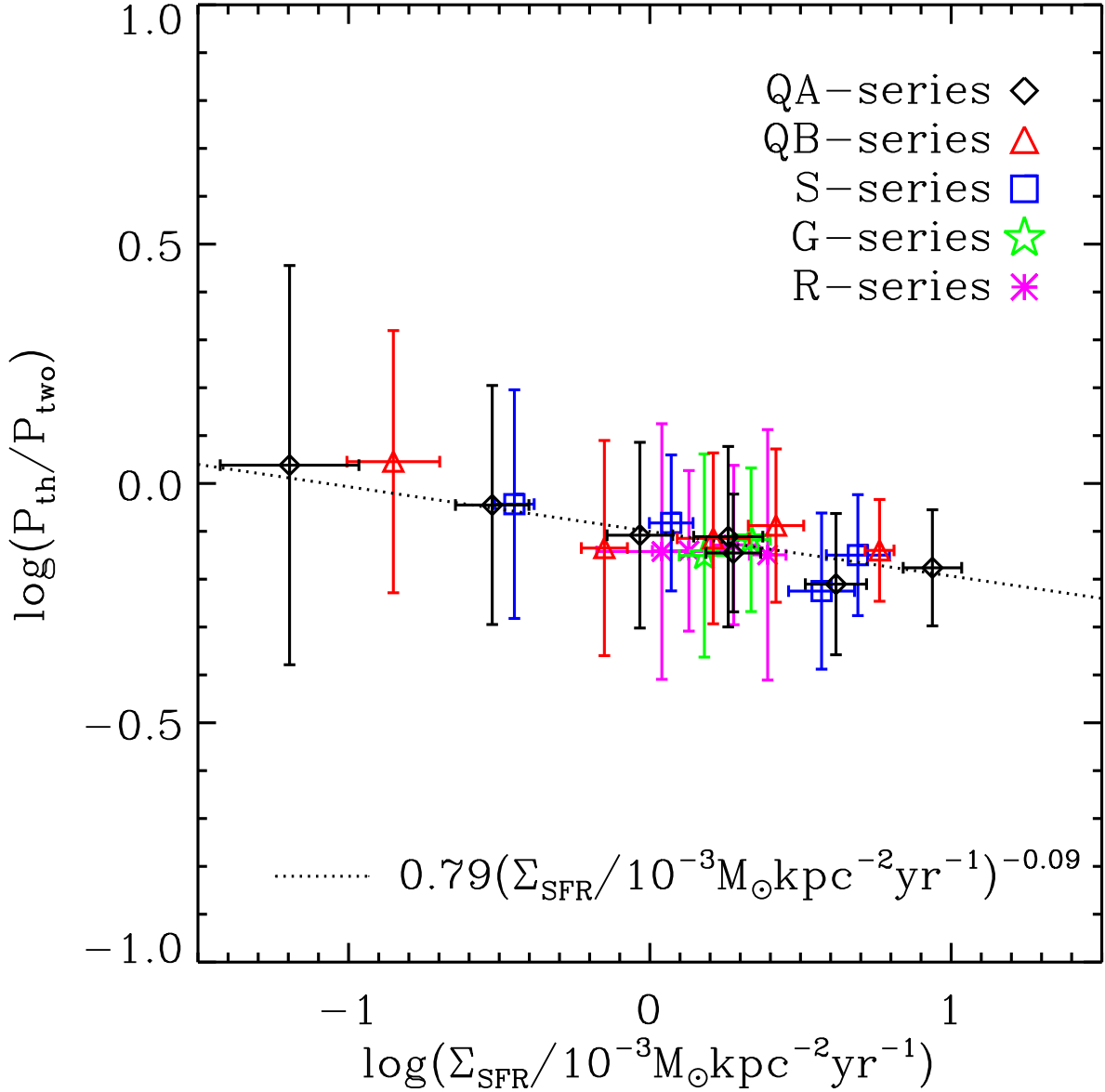
Fig. 10.— Measured midplane thermal pressure P_{th} of the diffuse gas relative to the two-phase thermal equilibrium pressure P_{two}, as a function of Σ_{SFR}. The points and errorbars give the mean and standard deviations over $t/t_{orb} = 2-3$ for each model. The dotted line, with a slope of -0.09, gives the best fit. Heating/cooling and mass exchange between warm and cold atomic phases enables the mean pressure to track the (radiation) energy input from star formation $P_{th} \propto P_{two} \propto \Sigma_{SFR}$ over more than two orders of magnitude in Σ_{SFR}.
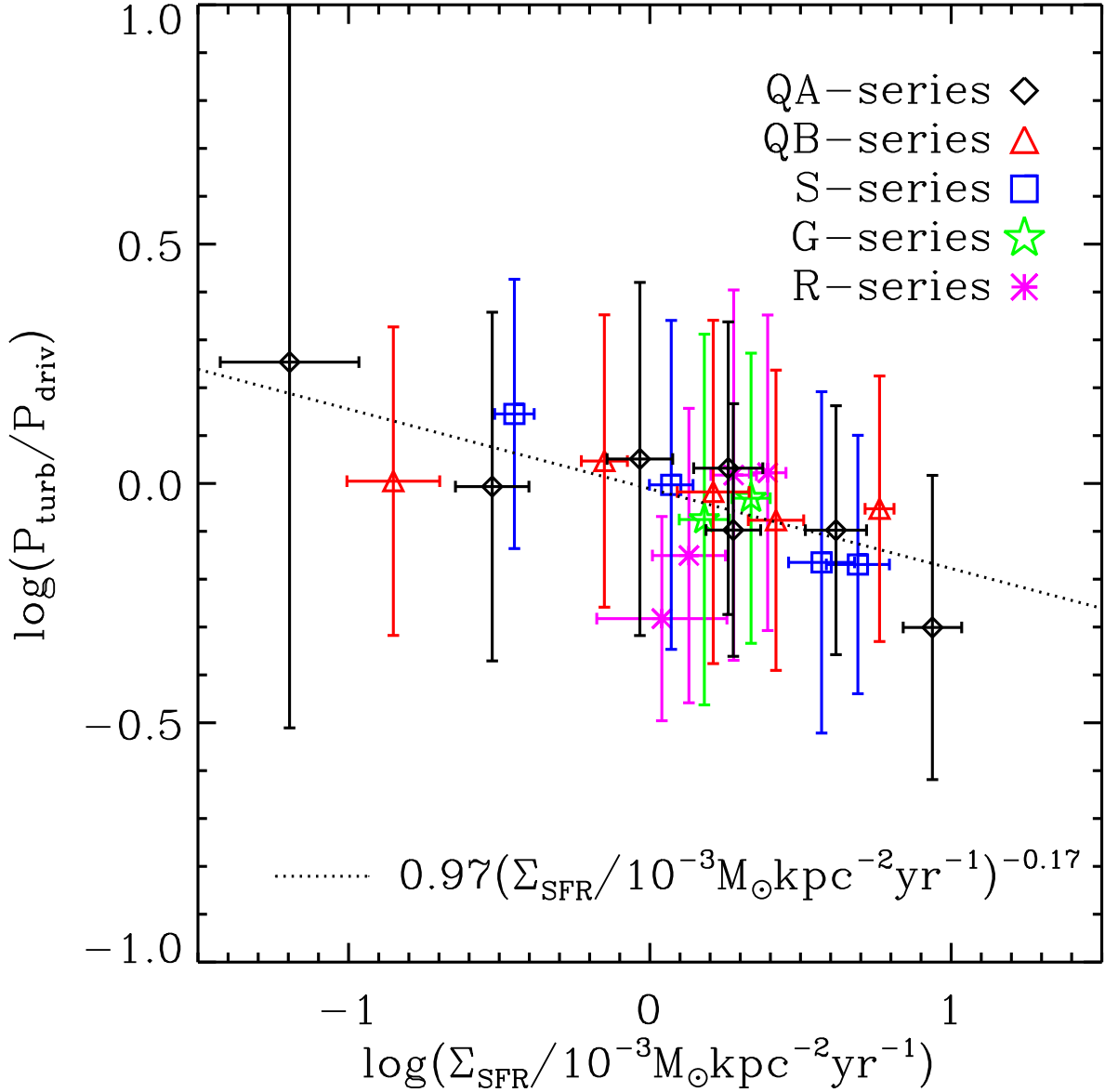
Fig. 11.— Measured midplane turbulent pressure $P_{\rm turb}$ of the diffuse gas relative to the vertical momentum flux injected by star formation $P_{\rm driv}$, as a function of $\Sigma_{\rm SFR}$. The points and errorbars give the mean and standard deviations over $t/t_{\rm orb} = 2 - 3$ for each model. The dotted line with a slope of -0.17 gives the best fit. The result $P_{\rm turb} \sim P_{\rm driv}$ indicates that turbulent driving is consistently balanced by dissipation on approximately a vertical crossing time, even though both terms vary by more than two orders of magnitude as $\Sigma_{\rm SFR}$ changes.
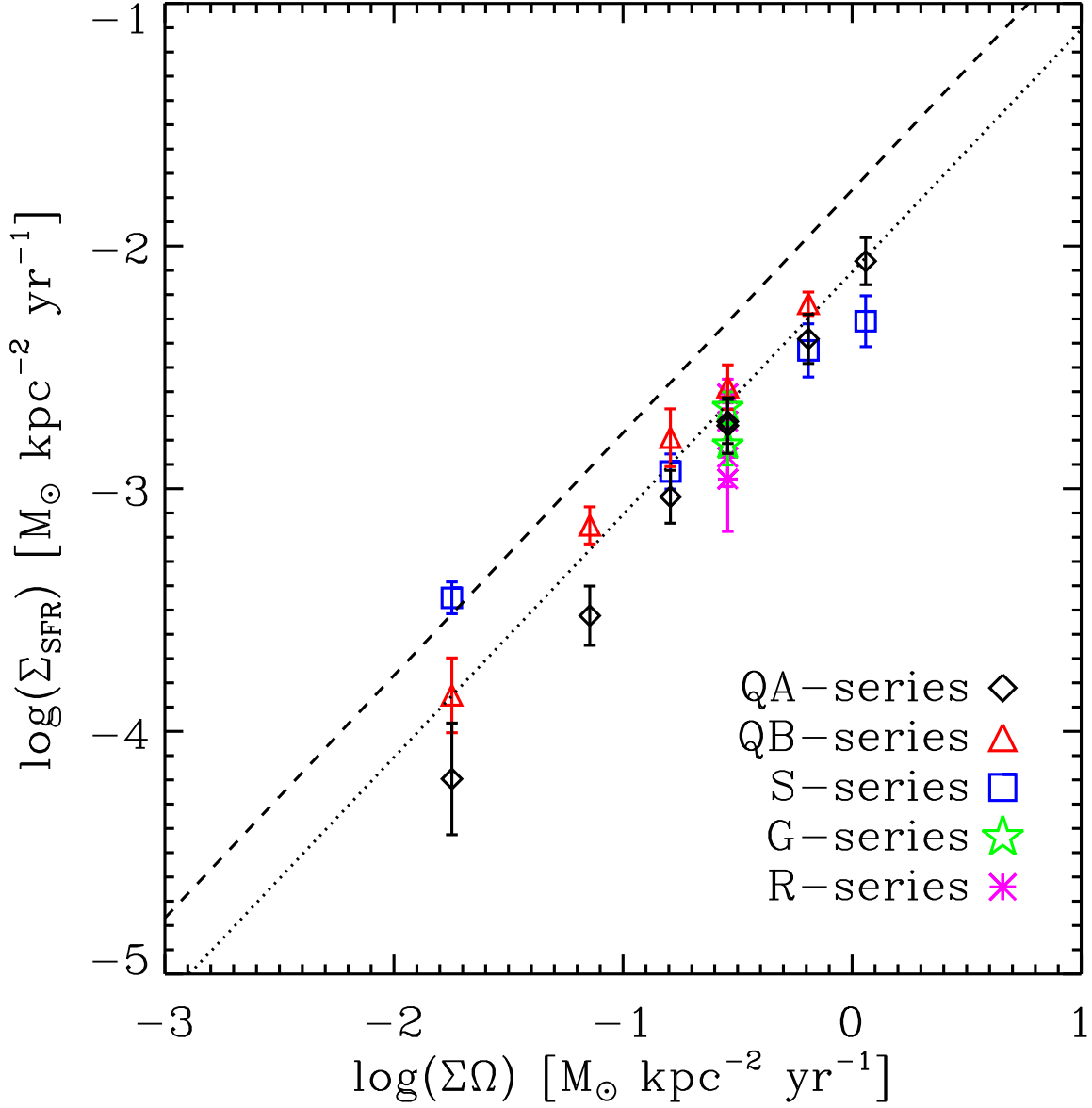
Fig. 12.— Measured Σ_{SFR} as a function of $\Sigma\Omega$ for all models. The points and errorbars give mean values and standard deviations over $t/t_{orb} = 2-3$. The dotted line shows our best fit $\Sigma_{SFR} = 0.008\Sigma\Omega$ for an imposed unity slope, and the dashed line shows the empirical result $\Sigma_{SFR} = 0.017\Sigma\Omega$ of Kennicutt (1998).

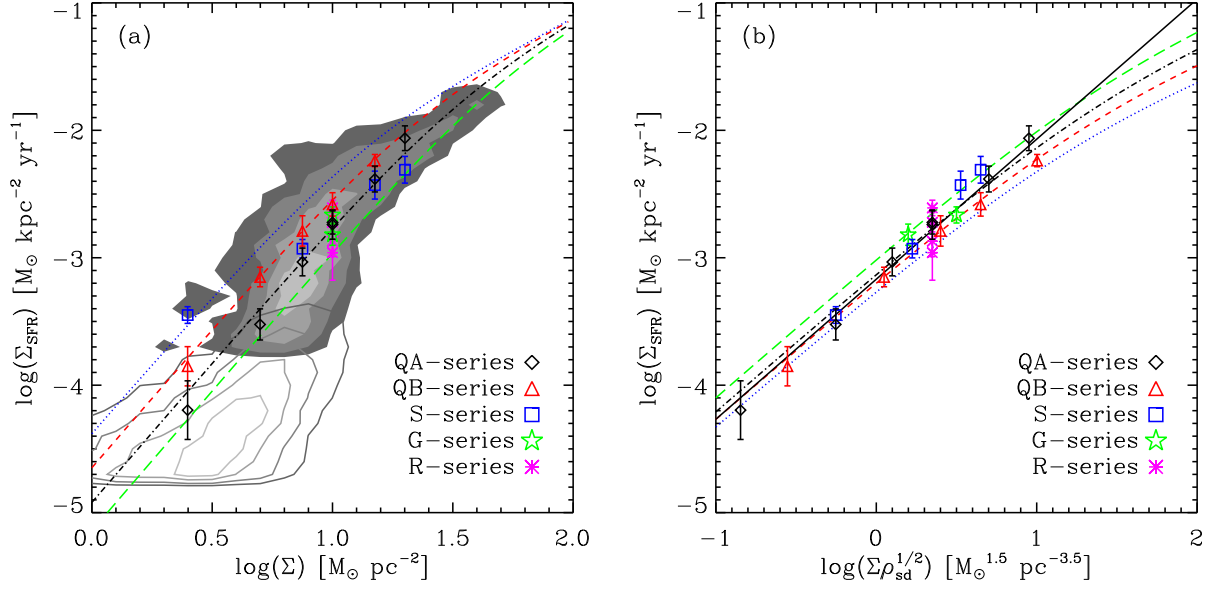Fig. 13.— SFR surface density Σ_{SFR} as a function of (a) Σ and (b) $\Sigma\rho_{sd}^{1/2}$ for all models. The points and errorbars give the mean and standard deviations over $t/t_{orb} = 2-3$, respectively. In both panels, blue dotted, red dashed, black dot-dashed, and green long-dashed lines give the theoretical predictions obtained by solving equations (5), (11), and (35) simultaneously for $s_0 = 0.02, 0.07, 0.28$, and 1.10, respectively. The parameters $\sigma_z = 7$ km s^{-1}, $\alpha = 5$, and $t_{SF,GBC} = 1.3$ Gyr are held fixed for these analytic comparisons, while η_{th} varies following the numerical fit in equation (42) with $f_{rad} = 1$. Filled and empty contours in (a) show the observational measurements in the regions inside (Bigiel et al. 2008) and outside (Bigiel et al. 2010) of the optical radius, respectively, for nearby spirals and dwarf galaxies: the contour levels from dark to light correspond to 10%, 25%, 50%, and 75% of the data. With higher s_0 and/or f_{rad} at low Σ (not shown), the models can match the observations beyond the optical radius. The black solid line in (b) denotes the power-law solution for Σ_{SFR} in equation (47). Note that Σ_{SFR} is much better correlated with the combination $\Sigma\rho_{sd}^{1/2}$ than with Σ alone.
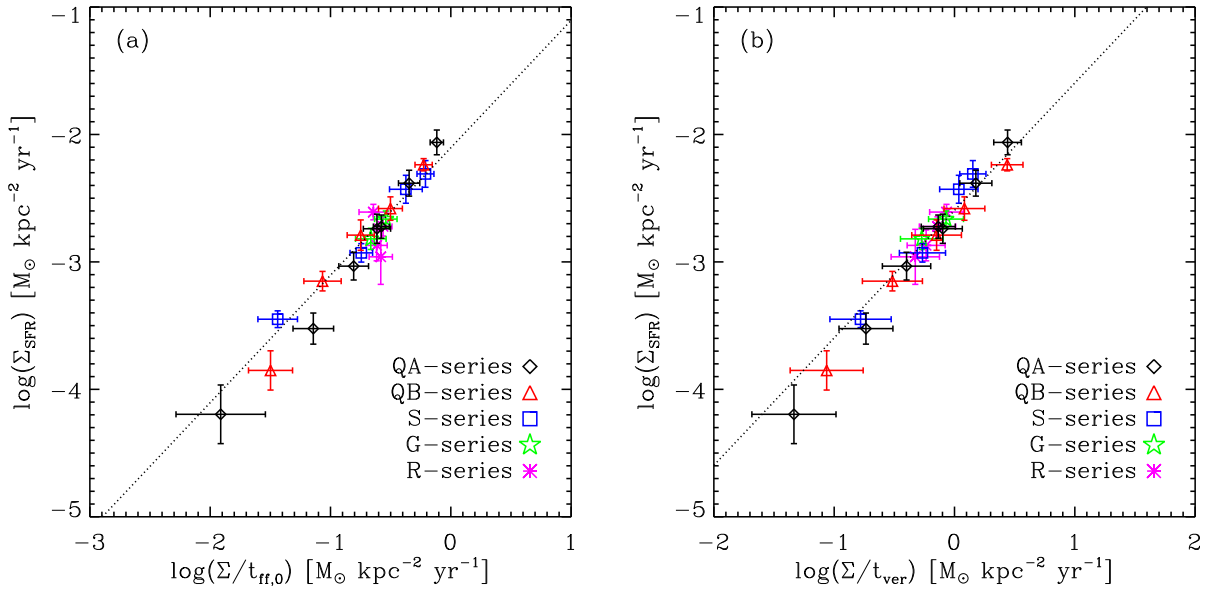
Fig. 14.— Measured SFR surface density Σ_{SFR} as a function of (a) $\Sigma/t_{ff,0}$ and (b) Σ/t_{ver} for all numerical models, where $t_{ff,0} = (3\pi/(32G\rho_0))^{1/2}$ and $t_{ver} = H_{diff}/v_{z,diff}$ are computed using time-averaged values of the variables. The points and errorbars give the mean and standard deviations over $t/t_{orb} = 2-3$. The dotted lines in (a) and (b) show our best fits for imposed unity slopes, $\Sigma_{SFR} = 0.008(\Sigma/t_{ff,0})$ and $\Sigma_{SFR} = 0.0025(\Sigma/t_{ver})$, respectively.

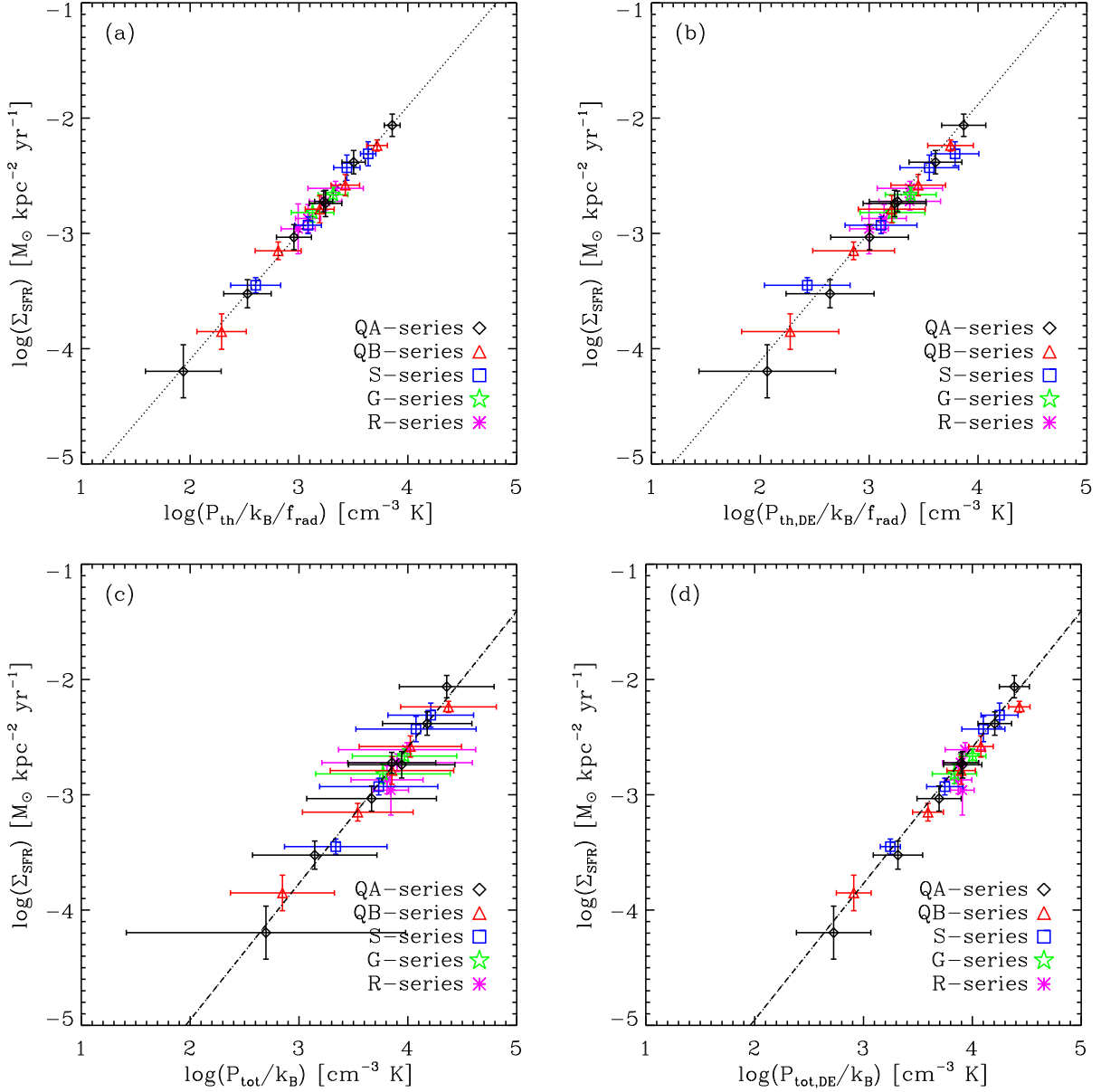Fig. 15.— Surface density of star formation Σ_{SFR} measured from the simulations as functions of (*a*) the measured midplane thermal pressure of the diffuse gas P_{th}, (*b*) the predicted midplane thermal pressure $P_{\mathrm{th,DE}}$, (*c*) the measured midplane total pressure of the diffuse gas P_{tot}, and (*d*) the predicted midplane total pressure $P_{\mathrm{tot,DE}}$. The points and errorbars give the mean and standard deviations over $t/t_{\mathrm{orb}} = 2 - 3$. Predicted pressures use the dynamical equilibrium equation (35) and measured values of f_{diff}, α, and $\sigma_{z,\mathrm{diff}}$ for each model. In (*a*) and (*b*) P_{th} and $P_{\mathrm{th,DE}}$ are divided by f_{rad} to compensate for varying heating efficiency so that Series R may be compared with other series. In top and bottom panels, dotted lines are obtained from equations (11) and (45), respectively, using the numerical calibrations (42) and (44). The dashed lines in bottom panels show the best fit given by equation (49). The pressures and Σ_{SFR} are extremely well correlated, consistent with the idea that Σ_{SFR} adjusts until the pressures (driven by feedback) match equilibrium requirements.